Analysis, Segmentation and Prediction of Knee Cartilage using Statistical Shape Models

A Dissertation Presented for the
Doctor of Philosophy
Degree
The University of Tennessee, Knoxville

Joseph Michael Johnson
December 2013

Copyright © 2013 by Michael Johnson
All rights reserved.

Dedication

To my wife Sarah. All day.

Acknowledgements

I would like to thank those that helped with this particular work – namely: Dr. Emam Abdel Fatah, Wes Underwood, and many undergraduates at the Center for Musculoskeletal Research (CMR) who performed the thankless task of image segmentation that is the foundation of this work. To my colleagues at CMR, for their friendship and daily contributions to this work and my overall experience during my time at UTK. To my committee, for their time and opinions, for which I am always thankful: Dr. Richard Komistek, Dr. William Hamel, Dr. Aly Fathy, and especially Dr. Mohamed Mahfouz – without whom none of this would have been possible.

To Rebecca and Lyndsay: for never killing the messenger.

To all my friends and family who have kept me motivated and never stopped asking "So, when do you think you'll be finished?" in all of its various forms.

To my parents, for supporting me through too many years of school.

Abstract

Osteoarthritis (OA) of the knee is one of the leading causes of chronic disability (along with the hip). Due to rising healthcare costs associated with OA, it is important to fully understand the disease and how it progresses in the knee. One symptom of knee OA is the degeneration of cartilage in the articulating knee. The cartilage pad plays a major role in painting the biomechanical picture of the knee. This work attempts to quantify the cartilage thickness of healthy male and female knees using statistical shape models (SSMs) for a deep knee bend activity. Additionally, novel cartilage segmentation from magnetic resonance imaging (MRI) and estimation algorithms from computer tomography (CT) or x-rays are proposed to facilitate the efficient development and accurate analysis of future treatments related to the knee. Cartilage morphology results suggest distinct patterns of wear in varus, valgus, and neutral degenerative knees, and examination of contact regions during the deep knee bend activity further emphasizes these patterns. Segmentation results were achieved that were comparable if not of higher quality than existing state-of-the-art techniques for both femoral and tibial cartilage. Likewise, using the point correspondence properties of SSMs, estimation of articulating cartilage was effective in healthy and degenerative knees. In conclusion, this work provides novel, clinically relevant morphological data to compute segmentation and estimate new data in such a way to potentially contribute to improving results and efficiency in evaluation of the femorotibial cartilage layer.

Table of Contents

Chapter 1 Introduction 1
1.1 Osteoarthritis of the Knee 1
1.2 Clinical Significance 5
1.3 Segmentation State of the Art 10
1.4 Segmentation Challenges 16
1.5 Estimation of Cartilage Thickness 22
1.6 Contributions 24
1.7 Organization of Dissertation 24
Chapter 2 Imaging of the Knee Joint 27
2.1 Imaging of Bony Anatomy 27
2.1.1. CT and X-Ray 29
2.1.2 MRI 31
2.2 Imaging Knee Joint Cartilage 34
2.2.1 MRI 34
2.2.3 CT and X-Ray 37
Chapter 3 Segmentation of Bony Anatomy 40
3.1 Segmentation using SSM 40
3.1.1 Building the SSM 41
3.1.2 Segmentation with SSM 43
3.2 Anchor Point Refinement 52
3.3 Atlas Parameters 53
3.4 Use of Segmented Bones 55
Chapter 4 Morphological Changes in Osteoarthritic Knees 56
4.1 Cartilage Thickness Distribution 56
4.2 Methods 58
4.2.1 Subject Selection 58
4.2.2 Cartilage Thickness Calculation 60
4.2.3 Cartilage Thickness Analysis 64
4.3 Results 64
4.3.1 Healthy Cartilage 64
4.3.2 Osteoarthritic Cartilage Maps 69
4.4 Kinematic Evaluation of Pathological Wear 85
4.4 Conclusions 90
Chapter 5 Local Supervised Learning for Cartilage Segmentation 92
5.1 Classifiers and Point Correspondence 92
5.2 Extracting Feature Vectors and Targets 94
5.2.1 Defining the Bone-Cartilage-Interface and Cartilage Labels 95
5.2.2 Extracting Features 95
5.2.3 Choice of Classifier 97
5.2.4 Classification of Points Along a Profile 98
5.2.5 Regularization by SSM 98
5.3 Segmentation Results 99

5.3.1 Datasets of Healthy Knees 99
5.3.2 Datasets of Osteoarthritic Knees 99
5.3.3 Error analysis 99
5.3.5 Osteoarthritic Results 108
5.4 Conclusions 113
Chapter 6 Cartilage Estimation 115
6.1 Building the *a priori* Information 117
6.1.1 Calculating the Cartilage Thickness and Location Model 117
6.2 Estimation Methods 117
6.2.1 Constructing the Initial Estimate 117
6.3 Results 119
6.4 Conclusions 124
Chapter 7 Conclusion and Recommendations 125
List of References 128
Vita 136

List of Tables

Table 1. Kellgren and Lawrence grading criteria for osteoarthritis. 8
Table 2. Mass attenuation coefficient for various tissues at 10 KeV (from http://physics.nist.gov/PhysRefData/XrayMassCoef). 28
Table 3. Subject demographics for healthy cartilage dataset. 58
Table 4. Subject demographics for cartilage datasets with degeneration. 59
Table 5. Makeup of male subject dataset by KL score and compartment of degeneration. 59
Table 6. Makeup of female subject dataset by KL score and compartment of degeneration. 59
Table 7. Global quantitative results for cartilage tissue in healthy male and female. 68
Table 8. Quantitative statistics for all divisions of degenerative cartilage tissues. Of note is the inability to tell differences by examining only the mean thickness, but that the standard deviation gives some indication of degeneration. 84
Table 9. Segmentation results for femoral cartilage of healthy male and female subjects. 102
Table 10. Segmentation results for tibial cartilage of healthy male and female subjects. 103
Table 11. Segmentation results for the femoral cartilage as divided by KL score. 109
Table 12. Cartilage segmentation results for the degenerative tibia dataset as divided by KL score. 110
Table 13. Segmentation Results for femoral cartilage using degenerative dataset divided by compartment of wear. 111
Table 14. Cartilage segmentation results for degenerative tibia divided by compartment of wear. 112
Table 15. Segmentation results from the proposed method compared with state-of-the-art. Best healthy result and best degenerative result are highlighted in bold. 113
Table 16.Results from cartilage estimation for the femur and tibia. 120

List of Figures

Figure 1. Close up view of frontal radiograph. Note only bone information is visible, and little direct information regarding cartilage is present in the image. 7
Figure 2. Axial slice of knee MRI. Notice poor contrast between anterior bone and soft tissues. This makes accurate segmentation difficult in this region. 15
Figure 3. Cartilage as it appears in MRI. Notice the poor contrast in contact areas, as well as the thin-sheet appearance of the tissue – sometimes only a few pixels in width. 18
Figure 4. Poor contrast at cartilage-soft tissue interface in posterior femoral condyle increases segmentation difficulty. 19
Figure 5. Laminar properties of images cartilage tissue in the patellar groove. Notice the appearance of a double layer. 20
Figure 6. Poor contrast on anterior of tibia where patellar tendon is near the bone. 21
Figure 7. Cartilage as visible in CT images. Notice little to no contrast for the majority of the cartilage tissue boundaries. It is not possible to accurately segment cartilage from CT images without the aid of some injectable contrast agent. 23
Figure 8. General flow from input of image data to segmentation and/or estimation of bone and cartilage data. 24
Figure 9. Long-film XR allows imaging of total leg in a weight-bearing position, allowing estimate of hip-knee-ankle lines. Left image is AP view, right is lateral. . 30
Figure 10. A subchondral lesion on MRI images of patient with osteoarthritis. This knee was given a grade of KL 3. 32
Figure 11. MRI image showing example of scanning protocol with image properties of light trabecular bone and dark cortical bone. The cortical bone appears as a thin black outline around the trabecular tissue. Accurate bone segmentation would require outlining both the trabecular and cortical bone tissue. 33
Figure 12. Alignment landmarks on mean surface models (top) and selected on the MRI images for registration (middle and bottom images are femur and tibia, respectively). Transformation between best fit from atlas models and selected points is used for registration of atlas to patient volume. 45
Figure 13. Examples of low-pass filtering properties of projection onto the atlas for femur (top) and tibia (bottom). Noisy models are on the left and model after projection onto the atlas is on the right. Notice significant reduction of noise. 47
Figure 14. Surface normals at each vertex. Sampling along these profiles is performed to determine the appropriate edge at each vertex. 48
Figure 15. Example intensity signal, smoothing and detected edge for bone segmentation. 50
Figure 16. Cumulative variance of PCs for the femur SSM. 54
Figure 17. Cumulative variance of prinicipal components for tibia SSM. 54
Figure 18. Semi-automatic segmentation of bone and cartilage from MRI images from the OAI dataset. The first step is to utilize the segmentation algorithm in Chapter 3 to segment the bone and cartilage data. Any remaining errors are then manually segmented using available tools. The resulting labels after the manual step represent the bone and the bone + cartilage. Subtraction of the two labels allows accurate

cartilage reconstruction while guaranteeing accurate BCI for thickness and location calculations. 61
Figure 19. Mean cartilage thickness for Caucasian male femur. 65
Figure 20. Standard deviation of cartilage thickness for Caucasian male femur. 65
Figure 21. Probability map for femoral cartilage presence on Caucasian male femur. 66
Figure 22. Mean thickness (left), standard deviation (middle) and probability (right) of Caucasian male tibia cartilage. 66
Figure 23. Mean cartilage thickness for Caucasian female femur. 67
Figure 24. Standard deviation of cartilage thickness for Caucasian female femur. 67
Figure 25. Probability of cartilage presence for Caucasian female femur. 68
Figure 26. Mean thickness (left), standard deviation (middle) and probability (right) of Caucasian female tibia cartilage. 68
Figure 27. Mean cartilage thickness of KL-1 grade femur. 69
Figure 28. Standard deviation of cartilage thickness for KL-1 grade femur. 70
Figure 29. Normalized fraction of mean healthy (KL-0) thickness for KL-1 grade femur. 70
Figure 30. Cartilage for KL-1 grade tibia. 71
Figure 31. Mean cartilage thickness for KL-2 grade femur. 71
Figure 32. Standard deviation of cartilage thickness for KL-2 grade femur. Note that despite thickness map appearing to be nearly normal, the deviation in the patellofemoral region is high. 72
Figure 33. Probability of cartilage presence for KL-2 grade femur. Note some patches of missing cartilage in the medial compartment. 72
Figure 34. Normalized fraction of mean healthy (KL-0) thickness for KL-2 grade femur. 73
Figure 35. Cartilage for KL-2 grade tibia. 73
Figure 36. Mean cartilage thickness for KL-3 grade femur. 74
Figure 37. Standard deviation of cartilage thickness for KL-3 grade femur. 74
Figure 38. Probability of cartilage presence in KL-3 grade femur. Notice the higher probability of missing cartilage than in KL-2 femurs, as expected. 75
Figure 39. Normalized fraction of mean healthy (KL-0) cartilage thickness for KL-3 femur. 75
Figure 40. Cartilage for KL-3 grade femur. 76
Figure 41. Mean femoral cartilage thickness for cases with varus defects. Note thin cartilage in medial tibiofemoral compartment. 76
Figure 42. Standard deviation of femoral cartilage thickness for cases with varus defects. 77
Figure 43. Probability of femoral cartilage for varus knees. 77
Figure 44. Normalized fraction of healthy thickness for femoral cartilage in varus knees. Note significant cartilage wear in the medial tibiofemoral compartment, which is expected in knee joints with varus malalignment. 78
Figure 45. Cartilage for tibia in varus knees. Note majority of tibia wear is in the medial compartment. 78

Figure 46. Mean femoral cartilage thickness in knees with valgus defects. Note that the femoral cartilage looks nearly healthy. 79
Figure 47. Standard deviation of femoral cartilage thickness in knees with valgus defects. 79
Figure 48. Probability of femoral cartilage in valgus knees. 80
Figure 49. Normalized fraction of healthy thickness for valgus knees. Note the lateral wear is mainly in the posterior compartment of the femur. 80
Figure 50. Cartilage for tibia in valgus knees. Note that most of the tibiofemoral wear is in the lateral tibia compartment. 81
Figure 51. Mean femoral cartilage thickness in knees with defects in both compartments. 81
Figure 52. Standard deviation of femoral cartilage thickness in knees with defects in both medial and lateral compartments. 82
Figure 53. Probability of femoral cartilage in knees with defects in both medial and lateral compartments. 82
Figure 54. Normalized fraction healthy thickness in knees with defects in both compartments. 83
Figure 55. Cartilage for tibia with defects in both medial and lateral compartments..... 83
Figure 56. Division of the medial and lateral condylar vertices on the mean femoral atlas model. The division plane was taken as the mean model point with normal direction along the principal axis pointing in the most ML direction. 86
Figure 57. All contact regions starting at 0° flexion on the top left and continuing in 20° increments in a serpentine fashion to the right. Each new color represents current contact region overlaid on previous regions. 87
Figure 58. Fraction of healthy thickness for contact regions at each flexion angle in the lateral tibia compartment. Each subplot represents a different category of knee alignment. Notice that in the varus and neutral knees, degeneration is present in the lateral compartment, but to a lesser extent than for valgus knees. 88
Figure 59. Fraction of healthy thickness for contact regions at each flexion angle in the medial tibia compartment. Each subplot represents a different category of knee alignment. Notice that in the valgus knee, there is little to no wear in the medial compartment, possibly suggesting that the lateral compartment is experiencing the vast majority of the loading. 89
Figure 60.Various neighborhoods of a vertex. The central vertex of the green neighborhood is the origin vertex, $\mathbf{v_i}$**.** Green vertices correspond to $Ni0$,yellow to $Ni1$, and so on. Larger neighborhoods reduce local tissue modeling. 94
Figure 61. Edge labeled region values (red) as detected from the intensity profile along the normal direction (green). Cartilage label is shown in blue for reference. In this example, edge region 0 corresponds to the cartilage tissue. 97
Figure 62. Sample segmentation for a healthy femoral case. 100
Figure 63. Example segmentation of tibia cartilage. 101
Figure 64. Comparison of true mean cartilage thickness (above) and segmented mean thickness (below) as segmented using SSM projection method for healthy male

femur. The overall patterns agree closely, with some apparent oversegmentation seen as a thicker cartilage pad. 105
Figure 65. Mean cartilage thickness of male tibia (left) compared with the mean thickness of segmented cartilage (right) using SSM projection method. 106
Figure 66. Mean cartilage thickness of healthy female femur (top row) compared to segmented female femur (bottom row) as segmented using the SSM method. 107
Figure 67. Mean cartilage thickness of healthy tibia (left) compared to mean segmented thickness (right) as by SSM projection method. The medial compartment appears nearly identical, but there is some oversegmentation in the lateral compartment. . 108
Figure 68. Caucasian male mean femur thickness. Note stark difference in cartilage thickness across the surface. Clearly, approximating the thickness as uniform will not suffice for most applications. 116
Figure 69. Segmentation of MRI image results in the SSM bone models in the appropriate pose. 118
Figure 70. Mean thickness of the femoral cartilage for healthy males (top) compared with the mean estimated thickness for healthy males (bottom). 121
Figure 71. Mean thickness of the tibia cartilage for healthy male (left) compared to estimated mean thickness for healthy males (right). 122
Figure 72. Mean thickness for healthy female femur (top) compared to estimated mean thickness of healthy female femur (bottom). 123
Figure 73. Mean thickness of healthy female tibia (left) compared with estimated mean thickness of healthy female tibia (right). 124

List of Abbreviations and Symbols

OA	Osteoarthritis
PACS	Picture Archiving and Communications System
RIS	Radiology Information System
TKR	Total Knee Replacement
OAI	Osteoarthritis Initiative
XR	X-ray
CT	Computed Tomography
MRI	Magnetic Resonance Imaging
KL	Kellgren and Lawrence score
WOMAC	Western Ontario and McMaster Universities
BCI	Bone-cartilage interface
LOGISMOS	Layered Optimal Graph Image Segmentation of Multiple Objects and Surfaces
DSC	Dice Similarity Coefficient
kNN	*k*-nearest neighbors
SSM	Statistical shape model
ASM	Active shape model
PCA	PC analysis
PC	Principal component
RMSE	Root mean squared error
SNR	Signal-to-noise ratio
FSE	Fast spin echo
SPGR	Spoiled gradient echo
FLASH	Fast low-angle shot
DESS	Dual echo steady state
JSW	Joint space width
SVD	Singular value decomposition
MCW	Mutual correspondence warping
$\boldsymbol{v_i}$	Vertex i
$\boldsymbol{N_i^k}$	k-ring neighborhood of v_i
$\left\|\boldsymbol{N_i^k}\right\|$	Number of neighbors in $\boldsymbol{N_i^k}$
$\boldsymbol{P_i}$	Profile at vertex v_i
$\boldsymbol{C_i^k}$	Classifier at v_i using k-ring neighbors

Chapter 1

Introduction

1.1 Osteoarthritis of the Knee

Osteoarthritis (OA) of the knee is one of the leading causes of chronic disability (along with the hip). Clinically, OA is defined as [1]:

> "OA diseases are a result of both mechanical and biological events that destabilize the normal coupling of degradation and synthesis of articular cartilage chondrocytes and extracellular matrix, and subchondral bone. Although they may be initiated by multiple factors, including genetic, developmental, metabolic and traumatic, OA diseases involve all of the tissues of the diarthrodial joint. Ultimately, OA diseases are manifested by morphologic, biochemical, molecular and biomechanical changes of both cells and matrix which lead to a softening, fibrillation, ulceration, loss of articular cartilage, sclerosis and eburnation of subchondral bone, osteophytes, and subchondral cysts. When clinically evident, OA diseases are characterized by joint pain, tenderness, limitation of movement, crepitus, occasional effusion, and variable degrees of inflammation without systemic effects."

Per the definition, there are many potential causes of primary OA, but in general, the presentation is often idiopathic - due to natural wear. While it is difficult to identify a

single underlying cause for most OA cases, with the exception of those caused by direct trauma or pre-existing joint malalignment, the existence of several risk factors have been well documented.

Age and body weight are two of the most strongly correlated risk factors for OA of the knee. The importance of muscle strength and ligament quality on knee joint stability is obvious. Sharma, et al. showed that various factors affect knee joint stability, including varus-valgus laxity's degradation with age [2]. As expected, muscle strength in the quadriceps also decreases with age [3].The degradation of stabilizing components with increased age partially explains the results of one longitudinal study suggesting that patients in the highest age bracket are approximately 2.4 times more likely to develop knee OA [4].With an aging population, it is no surprise that costs for OA related healthcare are on the rise.

Body weight is also strongly associated with the risk of OA, especially in the knee as it experiences forces that are three to seven times more than body weight. The medial compartment of the knee joint is almost nine times more likely than the lateral tibiofemoral compartment to develop OA due to the medial compartment's bearing approximately 50% more load than the lateral side of the knee. In addition to compartmental differences, the lateral meniscus bears nearly 70% of the lateral load while the medial meniscus carries only 50% of the medial load [5]. The medial tibiofemoral cartilage not only experiences more load in general, but a larger ratio of the load lies on the cartilage tissue. In a great example of form following function, Li, et al. [6] suggest that tibiofemoral cartilage is thicker in regions of cartilage-to-cartilage

contact by up to 40%. Joint instability and increased forces caused by excessive force loading from increases in body weight or patient age can cause failure of the stressed cartilage by exceeding load limits or unbalanced loading. Western populations are becoming increasingly obese, further increasing the demand for OA treatment and driving up healthcare costs.

One clue as to what causes the cartilage degradation associated with OA of the knee is the method of cartilage repair. Articulating cartilage tissue is a porous matrix supported by fibrous tissue. The level of hydration fluctuates with the amount of pressure on the tissue – hydrostatic pressure assists in supporting load, while energy is dissipated with displacement of interstitial fluid. Through normal activity, molecules in the interstitial fluid are critical for proper repair and sustenance of damaged cells in the cartilage matrix. The loading patterns consistent with daily activity under normal conditions provide a regular loading and unloading of the joint. The natural movement of interstitial fluid across and into/out of the cartilage matrix caused by the natural load pattern consistent with walking or light exercise provides an optimal pattern of degeneration and repair in a normally balanced knee joint. When static load is excessive (obesity) or energy is improperly dissipated or distributed (joint malalignment, surface incongruities), the cartilage surface may degrade without the proper balance of tissue regeneration [7],[8],[9]. If left alone, this degeneration can cause fibrillation of the articulating surfaces, lesions, and eventually full “bone-on-bone” joint failure.

In addition to cartilage degradation, the bony tissue also undergoes significant changes in cases of knee OA. Calcified growths near the cartilage boundaries, known as

osteophytes, are indicative of OA progression. These bony growths are irregular in shape and not well understood, but are believed to be caused by the presence of various growth factors introduced by processes initialized by cartilage loss [10],[11],[12],[13] – though additional work suggests they can appear as part of the natural aging process [14], [15]. Current standard of care dictates at least a single view radiograph (XR) to determine disease progression. As soft tissues are difficult or impossible to distinguish using XR, the osteophyte size and multiplicity – along with joint space characteristics – are used in most OA scoring systems. There are some references which show clear patterns to osteophyte growth – suggesting non-random growth, and thus, some predictable underlying factors may help determine location. Nagaosa, et al. showed that osteophyte location on XRs relative to the bones of the knee follows distinct patterns [16]. Any osteophyte growth negatively affects the congruity of the articulating surfaces, causing increased friction and additional abnormal wear, accelerating joint space deformation.

Treatment of OA is currently confined to alleviation of symptoms. In most cases, the most prominent symptom is pain. In the early stages of the disease, stabilization of the afflicted joint through physical training can provide some relief, but in most cases, the patient must rely on administration of analgesic medicine of varying strength to maintain a reasonable standard of living. Eventually, joint mobility is reduced to the point wherein some level of surgical intervention is required.

1.2 Clinical Significance

With swift technological advancements, the field of medical imaging is making the transition from manual analytical tools to automated analysis processes. This transition is a critical step towards reducing healthcare costs associated with imaging procedures. Manual bottlenecks in the imaging workflow are becoming increasingly apparent as the flow of information becomes more efficient with the widespread deployment of picture archiving and communication systems (PACS) and radiology information systems (RIS). One 2006 study of European hospitals found a wide variation of the implementation rates of PACS systems from 10% in France to 70% in Finland with a mean of approximately 33% [17]. The Healthcare Information and Management Systems Society (HIMSS) 2009 annual report indicates that roughly 75% of US hospitals had at least one radiology PACS system in use in 2008, which is an increase of 50% in 2006 [18]. This rapid rise in PACS implementation was driven by advances in medical technology, as well as an aging population, such that improvements in image resolution, coupled with the prospect of increasing numbers of imaging procedures require advanced methods of image storage and retrieval. Multi-detector row computed tomography (CT) scanners are capable of producing upwards of 1,000 images in only a few seconds, while analysis is limited by the efficiency of the physician in traversing the images. One area in special need of automated analysis tools is the orthopedic field, especially given the available forecasts of needed care.

The number of total knee replacements (TKRs) is expected to rise 673% by 2030 from 2005 numbers, and the number of revisions is expected to double by 2015 [19]. Due

to these increasing demands on orthopedic surgeons, efficiency in workflow must be achieved in all applicable areas. Surgeons use medical images for pre-operative planning, surgical navigation and in the design of customized surgical tools. Researchers and those involved in the development of novel treatments and management planning require accurate assessments of patient anatomy to determine efficacy of the proposed method of intervention. Effective surgical planning, including implant sizing, placement strategies, and, if desired, patient-specific cutting guide design, requires accurate reproductions of the patient anatomy. The patient anatomy, in the case of the knee, is often represented by three-dimensional (3D) models, consisting of a series of connected vertices defining the bone surface and/or the articulating cartilage surface. In surgical cases, these models are most often constructed by technicians manually tracing the outlines of the anatomical surfaces on the CT or MRI images. This manual segmentation process is time consuming, expensive, and can delay a much-needed surgical procedure. For researchers evaluating a proposed treatment, the time and labor required for the manual segmentation of many cases is often cumbersome and can become prohibitive. In addition to economic considerations, one study by Desmeules, et al. suggests that significant wait times can result not only in increased pain in the affected knee, but can also increase stress and pain in the contralateral knee [20]. This study makes apparent the need for removing any existing bottlenecks in the surgical workflow, of which manual segmentation and landmarking are a major contributing factor.

There are many treatments in development for OA. These include, but are not limited to, cartilage restoration, chondrocyte implantation and stem cells [21]. One major

challenge lies in assessing the efficacy of these treatments in a large population. While several biomarkers have been identified which may serve as indicators for OA, such as in [22-24], the ultimate standard for a promising treatment is stopping deformation of bone and cartilage in the affected joint. In other words, stopping osteophyte growth and cartilage degeneration or even reversing this process. A front view XR, as seen in Figure 1, allows for a quick assessment of joint spacing and alignment, but gives no indication of cartilage health, which requires a more detailed 3D imaging scan, such as MRI, contrast-enhanced CT, or XR via arthrography.



Figure 1. Close up view of frontal radiograph. Note only bone information is visible, and little direct information regarding cartilage is present in the image.

Unfortunately, this added information increases time required for analysis, and if volumetric measurements of cartilage or bone are required, it may take many hours per case to perform. Several methods of semi- and fully-automated segmentation for bone

and cartilage from MRI have been proposed with this problem in mind, but none have sufficiently resolved the problem of segmentation in OA knees.

In addition to tracking disease progression, regardless of application, automated, reproducible segmentation of the articulating knee surface can aid in disease classification. There are several existing classification systems, the most popular being the Kellgren and Lawrence (KL) score [25] and Western Ontario and McMaster Universities index (WOMAC) [26]. The WOMAC index is more difficult to define, as it is derived from the patient answers to many questions designed to assess overall pain and mobility. The WOMAC score is independent of joint appearance and can serve as an indicator of disease progression, but it is not a reliable indicator of actual joint damage.

The KL scoring system seeks to assign a score from 0-4, 0 being healthy and 4 being most severe, derived from features extracted from 2D XR images. Table 1 defines the criteria for each score.

Table 1. Kellgren and Lawrence grading criteria for osteoarthritis.

KL Score	Criteria
0	Healthy appearance
1	Doubtful joint space narrowing, possible osteophytic lipping
2	Definite presence of osteophytes, some joint space narrowing
3	Multiple osteophytes, definite joint space narrowing, mile sclerosis and bone deformation
4	Large osteophytes, significant narrowing, severe sclerosis and bone deformation

A major shortcoming of these classification systems is that they are subjective in nature and, in the case of the KL score, rely on measurements made from 2D imaging technology, which may obscure manifestations of OA, depending on the view and pose. The subjective nature essentially makes this scoring system inadequate for multi-user studies in research or a "go/no-go" system for determining surgical candidacy clinically. Accurate 3D reconstruction of patient anatomy can serve as a foundation for the development of a quantitative method of OA disease classification.

A major motivation for developing automated segmentation tools for the bones and soft tissue is to aid in the assessment of joint disease, especially OA. With this in mind, the National Institutes of Health have funded a major multi-center prospective, observational study of knee OA, the Osteoarthritis Initiative (OAI). The OAI dataset consists of 4,796 participants at baseline and follow up at 12, 24, 36 and 48 months. Each follow up includes a sagittal MRI for quantifying cartilage volume and thickness. A non-exposed control group consisting of 122 patients exhibited no signs of OA at baseline. This abundance of data has led to numerous publications regarding OA of the knee, but the manual or semi-automatic methods of knee segmentation and cartilage tracking makes analysis across the entire cohort nearly impossible. Much work has been published utilizing a subset of the cohort.

With the goal of standardizing nomenclature regarding OA of the knee and cartilage, Eckstein, et al. divided the knee anatomy into various compartments after consultation with experts [27]. This proposed nomenclature has been used to successfully quantify changes in cartilage thickness and bone structure in the presence of OA for a

variety of purposes using OAI data [28], [29], [30], [31], [32], [33]. Wirth, et al. used this nomenclature to assess cartilage loss in 396 OA patients [34] and to define a novel method of reporting cartilage loss using supposed ordered values [35]. While these studies provide valuable information on localizing and quantifying cartilage changes due to OA, the compartments described provide little local resolution and may be difficult to localize on a per patient basis, requiring manual identification of landmarks. Thus, a solution which can automate landmark selection to aid in articulating surface region identification, while improving resolution of cartilage analysis on the bone surface, can provide a consistent framework for joint analysis, independent of imaged pose or user.

1.3 Segmentation State-of-the-Art

Segmentation of bone and cartilage from 3D images is a major topic of research. Current medical segmentation methods can be classified as intensity-based, edge-based, region-based or deformable [36]. It is important to mention that a globally optimal segmentation solution for an *in vivo* joint has not been presented thus far, and that most solutions in literature rely on multiple methods to determine patient-specific anatomy. Often the bone is treated separately from the cartilage, as the appearance and modeling of the patient bone in MRI is much different than the cartilage, requiring different considerations for accurate segmentation. Fripp, et al. published two articles; the first of which utilized deformable shape models to constrain the shape and pose of the bones in the knee joint (femur, tibia and patella) [37]. From the bone segmentation, intensity and first derivative values near the segmented area, 3D surface models were used to identify

the bone-cartilage interface, or the area where the cartilage contacts the surface of the bone. The second paper used the bone-cartilage interface (BCI) as a foundation from which the cartilage was segmented using edge (first-order gradient) and intensity information, coupled with a global tissue classifier and cartilage thickness model [38].

One of the more interesting methods recently developed is the graph search and graph cut method. This involves defining a network of nodes connected with edges that define the "cost" of cutting each edge. The problem of optimally cutting edges to achieve good segmentation results was presented by Yin, et al. [39] with a method called Layered Optimal Graph Image Segmentation of Multiple Objects and Surfaces (LOGISMOS). This method treats the surfaces to be segmented as thin-sheets, which have some interaction constraints as defined by user-tailored cost functions. It was shown to work well with healthy and OA knees, but was sensitive to the initial bone segmentation and local changes in cartilage intensity. One difficulty of this method is extracting the complex cost functions needed as input to the algorithm – extraction and storage of multiple volumetric cost functions requires time and extensive memory. These could be probability maps for cartilage location and thickness, statistical models for intensity or edge maps derived from gradient information.

The two previously described methods can be thought of as 3D methods, meaning the operations are performed on the volumetric data, resulting in surfaces which outline the patient anatomy. In addition to extracting surface information, the labeling of the image data may be performed on the voxels themselves. An examples of a3D method includes the work of Pakin, et al. [40] who used a region-growing segmentation method,

followed by 2-class intensity-based local clustering, then 3D deformable models for cartilage separation. Their accuracy was 98.87%, and they reported sensitivity 66.22%, and specificity 99.56%. Grau, et al. [41] is another example where researchers used 3D method, proposing a general purpose, watershed-based algorithm that incorporated region-growing and edge existence probability mapping to limit expected over-segmentation. They tested their algorithm on datasets, producing average sensitivity, specificity, and Dice Similarity Coefficient (DSC) of 91.4%, 99.84%, and 0.84. In [42], a combination of binary *k*-nearest neighbor (kNN) classifiers are used to classify voxel elements of the medial femoral and tibial cartilage and the background, according to a set of selected image multi-scale features, including intensity, position, image derivatives, and eigen values and vectors of the Hessian. They achieved average sensitivity, specificity, and DSC of 83.9%, 99.9%, and 0.80, respectively. More recently, Wang, et al. utilized a global tissue classification using iterative semantic forests with a unique anatomical correspondence distance measure. They reported achieving 0.850 femoral DSC and 0.837 patellar DSC [43].

Examples of 2D methods include the work of Tang, et al. [44], who used Directional Gradient flow vector snakes to extract the cartilage surface of individual slices, Soloway, et al. [45], who used Active Shape Models (ASMs) and achieved a mean segmentation error of 0.58 pixels, and Dodin, et al. [46], who performed 2D textural analysis that involved filtering cartilage tissue using intensity and texture homogeneity analysis. Their results are further refined using a Bayesian test to discard synovial fluid outliers. They achieved a DSC of 0.84. The output of 2D methods is usually a series of

contours, which require further processing, such as 3D triangulation to create the required 3D model. Utilizing 3D methods, on the other hand, does not require additional processing, possibly leading to increased surface model accuracy.

In general, it is preferable to operate in 3D to maintain surface smoothness and global shape. Some challenges of operating in 3D include increased computational complexity, often by an order of magnitude or more, and constraining a global shape. The most promising technique for shape constraint is the use of SSMs or ASMs. These utilize *a priori* information to define parameters which control location of supposed landmarks. These landmarks lie in the same location of the shape in each instance of the shape model, making them ideal for localizing and storing information about the anatomical position of some feature or landmark relative to the shape model surface (e.g., cartilage location and thickness). This point correspondence property makes SSMs a good candidate for use as a base for building a cartilage segmentation method. This has been applied to several applications, including the papers by Fripp, et al. for the knee [37],[38]. While there are many different approaches to using SSMs or appearance models, (both include shape and appearance information), regardless of if they are surface or volume oriented, the general approach is the same. The vast majority of methods first seek to identify the easier anatomy – in the case of the knee, the bony anatomy – and then seek to define some computational methods around this initial segmentation for extracting the cartilage. Interestingly, there is little work combining the point correspondence of a surface atlas with the feature classification used with volumetric atlases, as in [42].

Segmentation of the bone from CT is somewhat well solved, at least when the bone is healthy. Merkl, et al. used deformable models to guide an edge-based segmentation approach with good results for the long bone in CT [47]. Segmentation from CT of bony anatomy is often much easier than a comparable MRI case, as the nature of the imaging modality makes the bone contours readily apparent and relatively easily discernible - both visually and via algorithmic methods. In fact, many times a reasonable result can be obtained through heuristic methods using intelligent application of basic image processing techniques, such as thresholding and region growing. Calder, et al. have recently proposed an iterative probabilistic method for discerning bony structures from CT using appearance similarity of bone and surrounding tissues [48]. Vasilache, et al. segmented injured pelvis bony tissue from CT scans using a combination of several more basic processing techniques [49].

In the more difficult scenario of segmentation from MRI, there has been much progress. Schmid, et al. describe a method of MRI segmentation using ASMs constrained by principal component (PC) forces and Markov Random Fields forces derived from image data to achieve a segmentation, reporting a root mean squared error (RMSE) of 1.44 mm [50]. The algorithm described is computationally complex and requires multiple parameter initializations and has not been realized on OA bones. As mentioned before, Fripp, et al. proposed a method using ASMs similar to that of Merkl and Mahfouz, although tissue characterization was used to guide detection of nearby edges [37]. They segment bone and tissue using global models initialized with global threshold to guide the first level of ASM segmentation. After initial segmentation, the tissue model is

updated to include tissue properties obtained from the first segmentation. This global method works well when the bone is healthy and local deformities are minimal, but in cases of OA or other diseases, this can cause errors in the segmentation, as the tissue models become inaccurate in areas of pathological change. The authors also reported failures due to poor contrast between bone and soft tissue, similar to those seen in Figure 2.

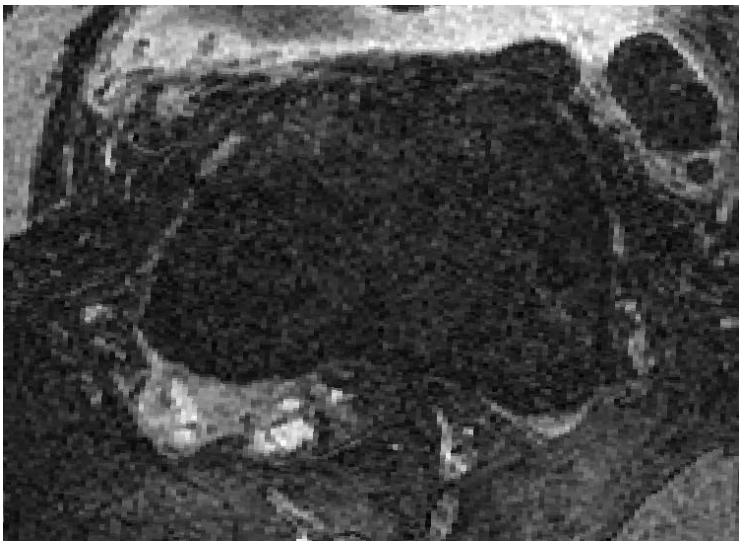


Figure 2. Axial slice of knee MRI. Notice poor contrast between anterior bone and soft tissues. This makes accurate segmentation difficult in this region.

Several methods have been proposed for MRI bone segmentation using various schemes aside from ASMs, such as graph cut [51], [52], and texture-based [53] methods. These methods have demonstrated good ability to segment bone from soft tissue, but errors in segmentation tend to result in irregular surfaces, which differ widely from expected anatomy. These irregularities make the resulting surface reconstructions unsuitable as an anchor for cartilage segmentation or as an input to patient-specific surgical planning. One advantage of ASM segmentation is that the resulting segmentation is constrained to the shape space.

1.4 Segmentation Challenges

An interested party may wonder, what is so difficult about segmentation (or estimation) of articulating cartilage? From a computer vision perspective, the difficulties are many. First and foremost, the structural nature of the tissue, which can be thought of as a "thin-sheet" laying on the bone surface, clearly makes identifying the boundary difficult, specifically in regions of contact. As a result, today's state-of-the-art 3D imaging modalities (CT, MRI) have resolutions which, when used in practice, are often taken very near (or even below) the Nyquist sampling frequency required to adequately represent the cartilage with image voxels. This problem is less of an issue with CT, as multi-detector scanners are able to achieve resolution on the order of tenths of a millimeter in less than a minute for large scan regions. The advantages of CT must be weighed with the disadvantages, such as requiring a contrast agent for visualization of cartilage boundary, which has been known to rarely cause adverse reactions in patients,

and perhaps most importantly, the exposure to radiation can be quite significant [54]. MRI has the distinct advantage of being non-ionizing, but it is considerably more time consuming and expensive. Also, in many orthopedic acquisition protocols, slices are acquired in the sagittal direction with sufficient in-plane resolution to adequately capture anatomical features (often less than half of a millimeter). Unfortunately, slice thickness is often captured at 2 mm and interpolated to 1 mm as a post-processing step, making small changes on the articulating surface due to disease difficult to reconstruct from image data. Therefore, any regions of the cartilage which are not oriented orthogonally to the sagittal plane and are less than 2 mm may not be reproducible. Figure 3 gives an example of the thin-sheet appearance in MRI.

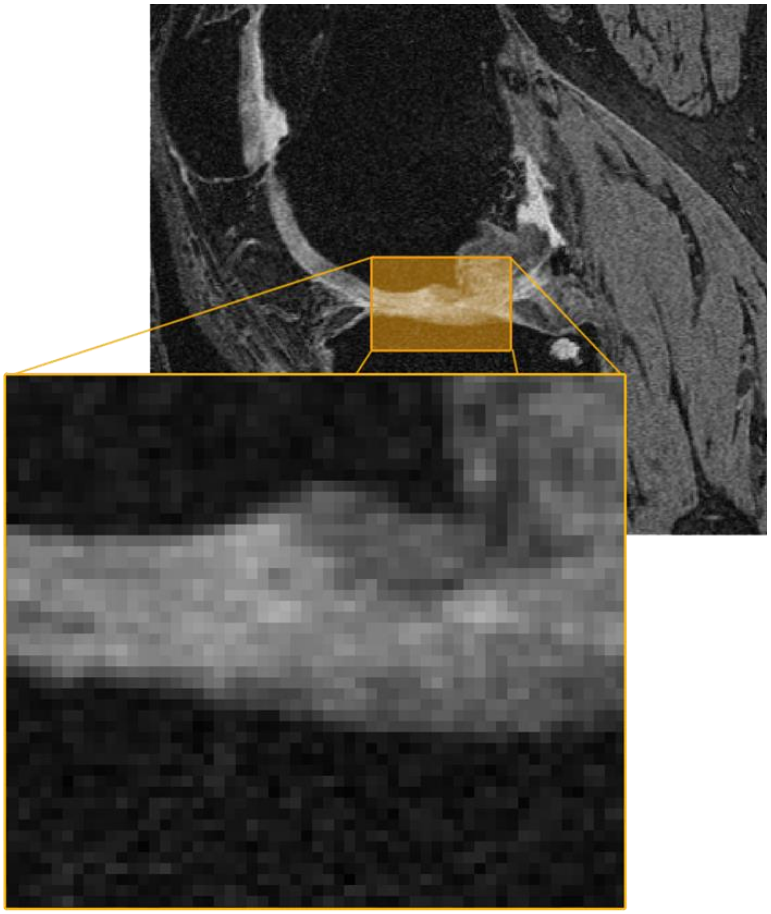


Figure 3. Cartilage as it appears in MRI. Notice the poor contrast in contact areas, as well as the thin-sheet appearance of the tissue – sometimes only a few pixels in width.

Another difficult challenge when segmenting the cartilage is the lack of contrast between cartilage tissue and surrounding soft tissues. While there are many existing protocols for imaging the articulating cartilage, the myriad of tissue types in contact with the articulating surface at any given time make choosing a protocol which differentiates cartilage across the entire surface while maintaining desired properties for diagnosis is not achievable at this time. As such, one or more cartilage-to-soft tissue contact regions may leave the cartilage boundary ambiguous in the image data, as in Figure 4, due to the

similar structural content of the tissues. This is especially evident in the posterior condyles and, perhaps more obviously, in the tibiofemoral and patellofemoral contact regions.

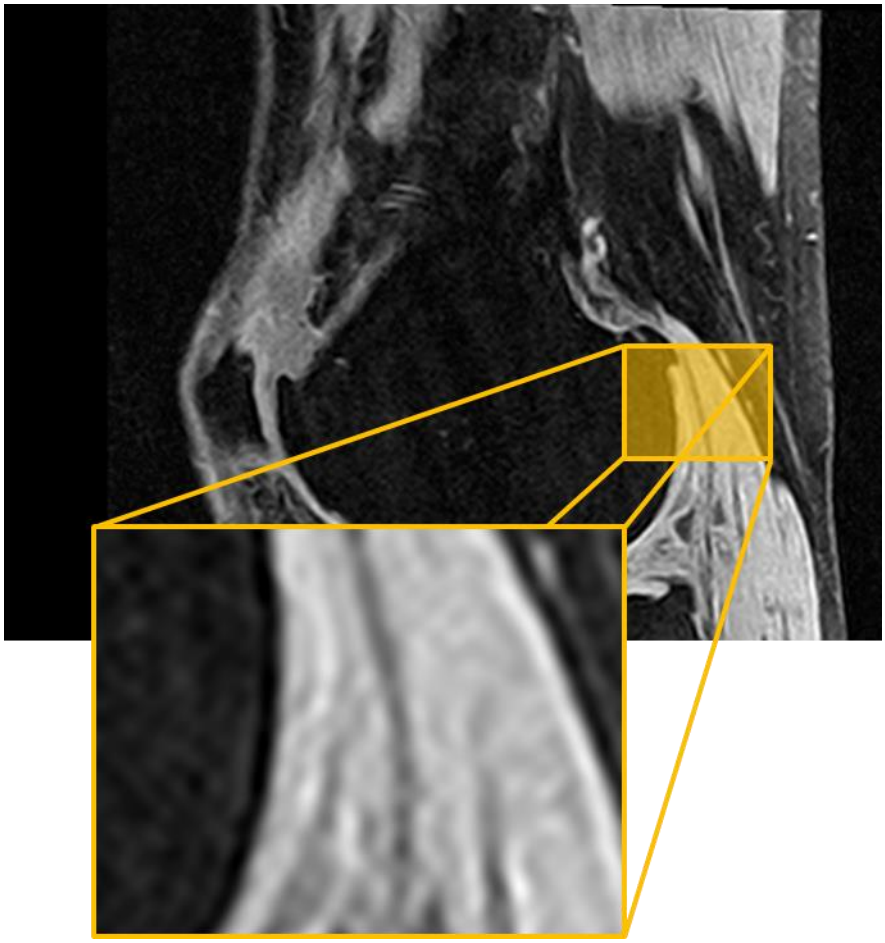


Figure 4. Poor contrast at cartilage-soft tissue interface in posterior femoral condyle increases segmentation difficulty.

Finally, the structural nature of cartilage makes detection of the boundary difficult in that the laminar structure of the tissue often causes many "false" edges within the tissue. This is especially clear in the posterior condyles and the patellar groove. This property of the

tissue also means that it the appearance of the tissue is not often globally consistent, making global feature classification inefficient. The task becomes doubly difficult as the cartilage laminar layers further deteriorate and fibrillation and lesions significantly alter the tissue appearance. Figure 5 shows some examples of the laminar tissue structure.



Figure 5. Laminar properties of images cartilage tissue in the patellar groove. Notice the appearance of a double layer.

Segmentation of the cartilage alone is one matter, but often it is desirable to have representative models of both the cartilage and the bone. Segmentation of the bone is fairly straightforward from CT, unless the bone has significant osteophytes, but can be quite difficult when segmentation is required from MRI volumes. Of course, the appearance of the bone and ease of segmentation is dependent upon the chosen protocol, but many orthopedic MRI protocols are designed with imaging the cartilage and bone

lesions in mind, which can leave the appearance and contrast of the cortical bone suboptimal, especially in regions where the bone does not contact the cartilage (at the bone-cartilage interface, the boundary is easily identified). Figure 2 and Figure 6 show the poor contrast on the anterior portion of the femur and at the tibia tuberosity, respectively. This occurs because cortical bone has low signal in this particular MRI protocol, due to the relatively low water content. When fat suppression is included in the imaging protocol, fat and ligaments also appear similar to cortical bone, thus at contact regions between these particular tissue types, there is little contrast and the boundaries are difficult to differentiate.

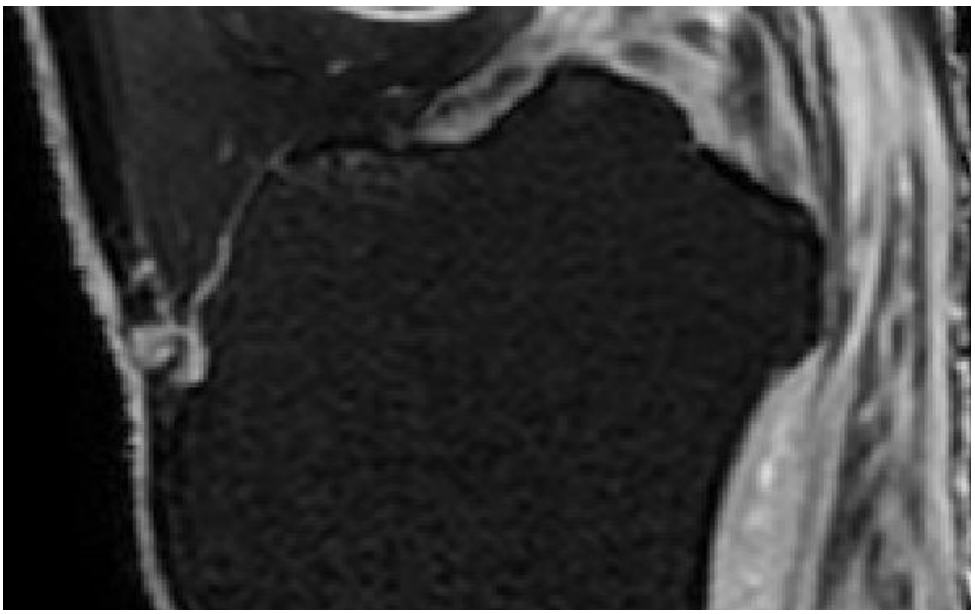


Figure 6. Poor contrast on anterior of tibia where patellar tendon is near the bone.

1.5 Estimation of Cartilage Thickness

Despite the wealth of patient-specific information provided by today's 3D image technology, many arthroplasty patients never undergo imaging with CT or MRI. All patients, however, receive XR imaging. It should also be noted that, despite the radiation exposure, CT (without contrast agent) as an imaging modality would be preferable to MRI due to cost considerations. Also, if a patient has any ferromagnetic material implanted in the body, they are not likely candidates for undergoing MRI imaging. The problem with both CT and XR is that the permittivity of cartilage is essentially the same as that of all the surrounding soft tissues, meaning there is no perceivable difference between cartilage and surrounding tissues in the image data, making accurate cartilage segmentation virtually impossible. As can be seen in Figure 7, there is virtually no distinguishable cartilage tissue visible in CT images.



Figure 7. Cartilage as visible in CT images. Notice little to no contrast for the majority of the cartilage tissue boundaries. It is not possible to accurately segment cartilage from CT images without the aid of some injectable contrast agent.

At least one study has shown that there is some correlation between tibiofemoral joint space width in the medial compartment, as measured on anterioposterior (AP) XR views, and cartilage thickness [55]. It has also been shown that relative cartilage thickness correlates with load distribution on the articulating surface [6]. At the time of this writing, there is no available work assessing the correlation between bony features, such as surgical measurements and widths with cartilage thickness. As a goal, the ability to predict the cartilage thickness based only on information available through cost effective imaging, such as CT and XR, would serve as a major contribution to the field by reducing imaging costs. In general, the workflow for all modalities can be seen in Figure 8.

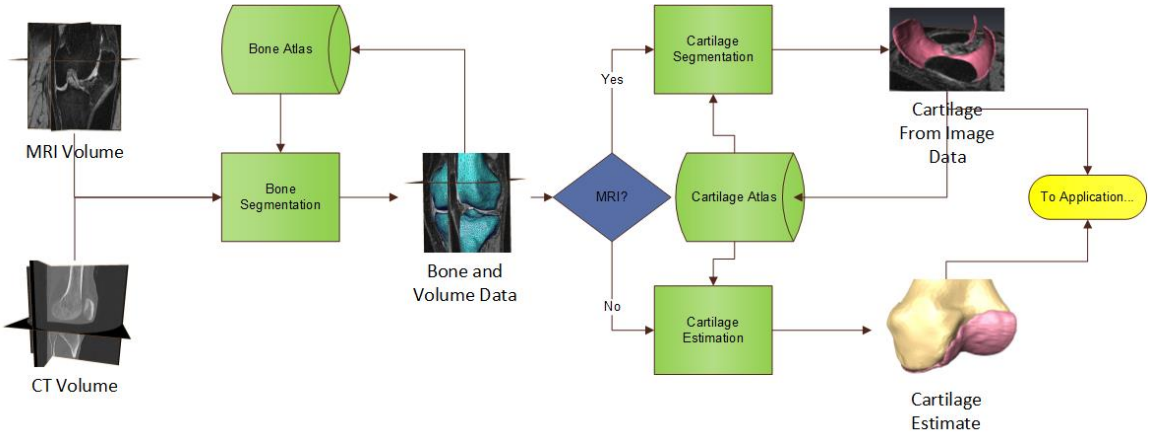


Figure 8. General flow from input of image data to segmentation and/or estimation of bone and cartilage data.

1.6 Contributions

The following list of contributions that are found in this work were developed using many sources of data, including the OAI for imaging data, CMR for segmentation of imaging data and the bone atlas foundations. My individual contributions are:

1. High resolution morphological analysis of tibiofemoral cartilage using statistical shape modeling of bone surfaces as foundation
2. Cartilage morphology of healthy and OA knees
    a. Divided OA knees by KL classification and compartment of defect
    b. Normalized wear patterns for degenerative cases
3. Kinematic analysis of cartilage wear in degenerative cases
    a. Comparison of cartilage wear for varus, valgus and neutral osteoarthritic knees in contact regions at various flexion angles during deep knee bend
4. Novel cartilage segmentation algorithm for MRI knee images

   a. Using SSM of cartilage and knee, network of local classifiers (~2000 for femur and ~1200 for tibia) at surface landmarks defined
   b. Accuracy shown to be as good as or better than current state-of-the-art
5. Unique division of classifier training data for degenerative cases
   a. Examined varus, valgus, neutral and division by KL scoring
6. Defined novel framework for estimation of cartilage from bones only

1.7 Organization of Dissertation

Chapter 2 of this work details different methods for static imaging of the knee joint and their applications. Specifically, subtleties related to this work are highlighted for XR, CT and MRI imaging modalities.

Chapter 3 describes segmentation methods of the bony anatomy, specifically, those based on statistical shape modeling techniques. The specific shape model based segmentation used as the foundation of the cartilage analysis in this work, adapted from previous efforts, is given in detail.

Chapter 4 proposes the cartilage analysis methodology, built on the SSM of the bony anatomy. Morphological features of the tibiofemoral cartilage compartments are reported for varus, valgus and neutral osteoarthritic cases, as well as for normal and healthy knees. A kinematic analysis of the morphological changes due to OA is reported.

Chapter 5 details a novel, local tissue classification for cartilage segmentation using the point correspondence of the statistical shape model.

Chapter 6 details the cartilage estimation framework from the cartilage statistical modeling presented in Chapter 4.

Chapter 7 provides conclusions based on this work, as well as proposing future directions of research based on the proposed methods.

Chapter 2

Imaging of the Knee Joint

The availability and use of diagnostic imaging for all procedures has rapidly risen over the last couple of decades [56]. While the information provided by these procedures can be extremely valuable, the costs associated with imaging are rising as well. For the diagnosis of OA, it would be ideal if every patient could undergo state-of-the-art MRI imaging procedures, but diagnostic quality must be balanced with costs. Therefore, it is important that accurate, patient-specific information can be extracted from the best resolution 3D modalities, as well lower XR costs. In this chapter, a brief overview of available imaging procedures for the knee is given, as well as some discussion of the advantages and disadvantages of each.

2.1 Imaging of Bony Anatomy

Imaging of bony anatomy and imaging the cartilage tissue require separate considerations. In general, CT and XR provide adequate bone visualization, but sacrifice cartilage appearance. A basic XR imaging system consists of a beam source, which generates and focuses the XR beam and a digital sensor, or film, placed so that the beam passes through the body before hitting the sensor. The sensor is excited relative to the strength of the beam hitting it, so that a weaker beam results in lower excitement and a stronger beam (unattenuated) results in a stronger excitation. The level of attenuation is directly mapped to image intensity (higher attenuation appears brighter in the images). The level of attenuation as the beam passes through the body is dependent on the

characteristics of the tissues along the beam path. In general, denser tissues (e.g., bone) will cause more attenuation. The tissue mass attenuation coefficients give some idea of expected contrast between tissues on resultant images.

Table 2. Mass attenuation coefficient for various tissues at 10 KeV (from http://physics.nist.gov/PhysRefData/XrayMassCoef).

Tissue	***Mass Attenuation Coeff.***
Adipose Tissue	*3.268*
Skeletal Muscle	*5.356*
Soft Tissue	*5.379*
Cortical Bone	*28.51*

As can be seen in Table 2, the attenuation coefficients of soft tissues are very similar to one another, and dissimilar to hard tissue, like cortical bone. In reality, this coefficient varies with beam energy – higher energy results in lower attenuation – and image contrast is dependent on many factors, such as beam hardening and blurring. In general, understanding beam attenuation and its relationship with image intensity reveals why imaging bony anatomy with XR-based modalities is sufficient for most cases, but if cartilage or other soft tissues require direct assessment, the poor contrast makes MRI a more suitable imaging modality.

2.1.1. CT and X-Ray

XR is generally considered the standard imaging technique for assessing joint damage. One of the more widely used osteoarthritic scoring systems, the KL score, is assessed by considering osteophyte growth and joint space on radiograph. Some imaging sites have access to long-film XR which can be used to assess overall joint alignment by including the hip, knee and ankle in a single frame while bearing weight, as in Figure 9.

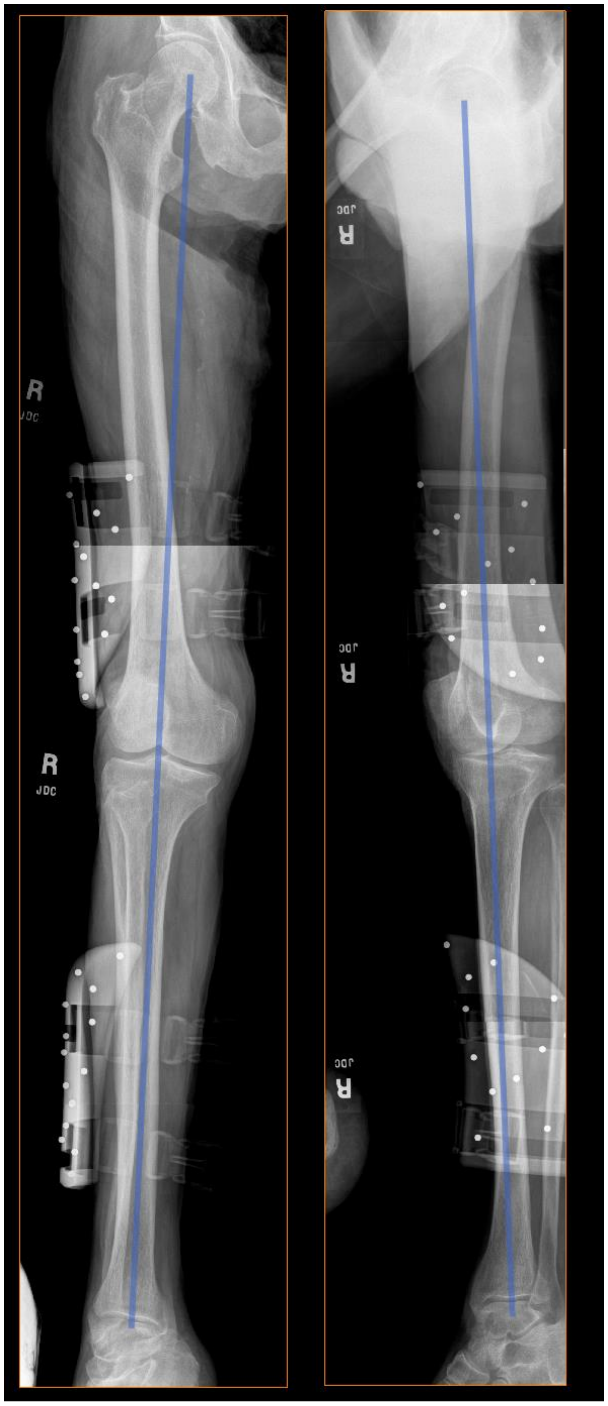


Figure 9. Long-film XR allows imaging of total leg in a weight-bearing position, allowing estimate of hip-knee-ankle lines. Left image is AP view, right is lateral.

Every patient undergoing joint evaluation will receive an XR because it is cost effective, radiation exposure is low, and it is available in most clinics. From XR, the clinician is able to quickly assess joint health, but is limited by the 2D nature of the images if a feature of interest is occluded due to the image direction.

For some applications, sub-millimeter resolution is required in 3D. The most cost effective and accurate modality for this is CT, which is essentially many XR images processed to provide a 3D reconstruction of the imaged volume. Computer tomography is ideal for imaging the bony anatomy because, as with XR, the physics of the modality allow strong contrast between bone and surrounding soft tissue. The 3D information allows accurate quantification of joint structure and spacing across the entire articulating surface, assuming the protocol is chosen such that axial resolution is sufficient to image the space between the contact surfaces. The disadvantages of CT are that the amount of radiation received by the patient can be quite significant and, as with XR, the cartilage tissue is difficult to distinguish due to extremely poor contrast.

2.1.2 MRI

Appearance of bone and features of interest can vary greatly in MRI imaging. The choice of protocol and tissue structure significantly influence image appearance and the ability to distinguish interesting features. For bone, interesting features are often lesions and edema related to OA (Figure 10), as well as the more obvious osteophyte growth and changes related to osteolysis. Damage to the cartilage surface is often directly related to the formation of edema in the subchondral bone.

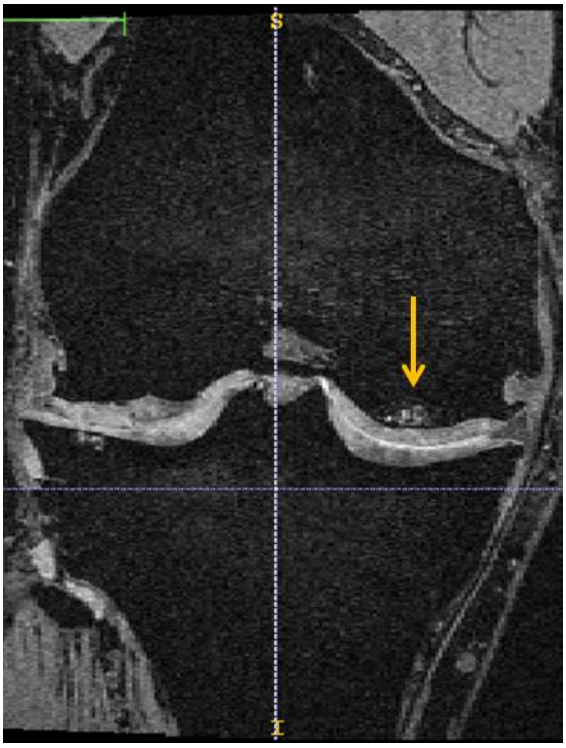


Figure 10. A subchondral lesion on MRI images of patient with osteoarthritis. This knee was given a grade of KL 3.

It is important to realize that MRI imaging is used most often for imaging soft tissue, as the water content of the cortical bone is relatively low, which causes it to virtually always appear black. However, the trabecular bone is readily visible in T1-weighted images or similar, as in Figure 11.



Figure 11. MRI image showing example of scanning protocol with image properties of light trabecular bone and dark cortical bone. The cortical bone appears as a thin black outline around the trabecular tissue. Accurate bone segmentation would require outlining both the trabecular and cortical bone tissue.

One study used a similar protocol to segment the "bone" using graph-cut methods, but actually only segmented the trabecular bone. Therefore, if patient-specific models had been required for measurement, the results would have seemed quite small. Essentially, the trabecular bone will appear similar to adipose tissue in most MRI protocols. This becomes somewhat problematic when using fat suppression to further highlight cartilage

tissue, as this causes the entire bone region to appear dark, as well as surrounding ligaments and adipose tissue, making bone boundaries difficult to detect, as in Figure 2.

2.2 Imaging Knee Joint Cartilage

In cases of OA, it is highly desirable to assess the health of both bone and cartilage tissues. Choosing a modality which balances cost, patient risks and imaging capability can be challenging given the properties of available modalities. This section describes the cartilage imaging capabilities of the most commonly used imaging modalities to highlight the many different appearances cartilage can take in orthopedic practice.

2.2.1 MRI

As of now, if the cartilage itself is to be directly assessed visually and in a non-invasive manner, MRI is the only available modality capable of providing the desired information. Modern MRI capabilities move the challenge from one of capability to one of choice. In other words, there are many options relating to MRI acquisition protocol and scanner choice which can affect the image quality as it relates to cartilage contrast-to-noise ratio. With judicious choice of scanner and acquisition protocol, the cartilage tissue (and even non-morphological information regarding underlying structure) can be accurately assessed.

The simplest and often least controllable aspect of imaging is the scanner. Most often, consideration is given to two major aspects of the instrument – magnetic field strength and magnet design. The strength of the magnetic field directly affects the signal-to-noise ratio with higher strength magnets corresponding to improved signal-to-noise.

Low-field strength scanners have been shown to limit diagnostic effectiveness of OA [57], [58], [59]. This is due to the low contrast-to-noise properties of the cartilage – being a fairly thin structure, as well as having material properties similar to the surrounding joint fluid, makes delineation of the tissue highly dependent on signal-to-noise ratio (SNR) properties. Standard field strength of 1.0 T to 1.5 T is sufficient for most diagnostic needs and is most often used in studies assessing OA diagnostic capability with MRI. A stronger field strength of 3.0 has been shown to improve diagnostic capability [60], [61], as well as volumetric cartilage measurements [62] and is the strength of choice for the OAI study. Higher field strengths, such as 7.0 T, are used almost exclusively for research purposes and have shown somewhat diminishing returns in terms of image improvement [63].

The other scanner consideration is the configuration of the magnet, either considered open or closed. A closed magnet most often relies on a table system to pass the patient through the magnetic bore. These systems are the most common systems in use and tend to give the best SNR, but are limited by allowing acquisition only in the supine position. Additionally, obese patients or those experiencing extreme claustrophobia may require a more open configuration. Open MRI systems were, until recently, often of much lower field strength, usually 0.2 T, reducing SNR, thereby also reducing the ability to assess morphologic changes to cartilage tissue. However, modern systems are on the order of 1.0 – 1.5 T and depending on configuration, can allow imaging of weight-bearing knees, providing valuable static information on mechanical properties of the joint [64]. In general, the SNR of modern open systems should provide

images suitable for assessment and segmentation processing. The major consideration then lies in the choice of acquisition protocol, as this is usually the predominant factor in determining image characteristics.

There are numerous available image protocols tailored to obtain optimal cartilage visibility and contrast in the resultant images. In practice, not every modern protocol is available at acquisition time, and good results are often obtained using any fluid sensitive, fat suppressed sequencing protocol, as well as fast spin echo (FSE) [63]. Popular specific protocols include proton density, T2-weighted FSE, 3D spoiled gradient echo (SPGR), fast low-angle shot (FLASH) and dual echo steady-state (DESS) [58]. The OAI acquires all images at 3.0 T using 3D DESS with thin sections, obtaining nearly isotropic voxels permitting excellent assessment characteristics in all three common reconstruction directions (i.e., sagittal, axial and coronal). For this study, all subjects were from the OAI datasets, but images obtained from any sequence which provides similar cartilage contrast, as well as those having dark bone and lighter intensity cartilage, should be adequate. Interestingly, the researcher may find that the best sequence protocol for diagnosis is insufficient or incompatible with the developed algorithm(s). Also worth noting is that gadolinium enhanced arthrography is possible in MRI and has been shown to be a good tool for assessing joint disease [65], [66], although the procedure is not often used due to the invasive nature of the injection. There are tools currently under development to simulate the effects of contrast through novel sequencing protocols, but these are new and not often available in practice.

2.2.3 CT and X-Ray

As previously mentioned, all patients receive XR when being evaluated for OA of the knee. Standing XR allows indirect evaluation of cartilage health in a load-bearing knee, although the tissue itself is not visible on XR. Additionally, the lack of cartilage on the resultant images means XR is not a valuable tool for assessing early stages of OA degeneration, as absence of findings cannot be considered lack of evidence of OA [63]. Work by Cibere suggests XR is a more apt tool for exclusion of alternative pathologies than as a tool for confirming existence of OA [67]. However, with XR being the least expensive and most common modality available, it is widely used for assessment of OA – specifically with the presence of osteophytes and assessment of joint space width.

XR is useful only for indirectly assessing cartilage thickness, which is accomplished by measurement of the joint space width. Joint space width (JSW) is defined dependent on the image view – most commonly AP with 20-35 degrees of flexion [68] – and is considered to be the minimum distance between femur and tibia in both lateral and medial compartments. It should be mentioned that a widely cited study by Buckland-Wright, et al. suggests JSW correlates with cartilage thickness only in the medial compartment and not the lateral [55]. In general, JSW is considered a standard indication of joint space narrowing, one of the signs of OA. An additional factor to be considered is that reproducing image views and JSW measurements on consecutive XR studies of the same patient is difficult and will result in random changes of measured JSW. Also, studies have shown that JSW can be caused by means other than cartilage degeneration, such as meniscal extrusion or subluxation [69-71]. Despite its limitations,

the cost, availability and traditional use of XR make it the most commonly used modality for assessing OA, although for some applications, the 2D nature of the technology is inadequate.

Occasionally, if 3D assessment is required and the patient is not able to undergo MRI, for reasons such as claustrophobia, obesity, pacemaker, or metal implant near the joint, CT is a viable alternative. Using traditional CT, it is nearly impossible to delineate cartilage from soft tissue, depicted in Figure 7. However, cartilage is accurately imaged with the aid of injected contrast agents in a procedure known as arthrography. Here, the contrast agent is a diluted solution of some radio-opaque material, such as iodine, which fills the joint space, allowing identification of the outer boundary of the cartilage and defects in contact with the outer boundary. In such images, the contrast fills the joint space, causing the space to take on a much brighter intensity, providing contrast between the fluid and darker cartilage tissue.

Studies have shown CT arthrography to be at least as accurate as MRI for assessing cartilage thickness [72, 73]. Additionally, CT arthrography does not decrease sensitivity of identification of chondral lesions as compared to MRI [74], although due to the nature of the contrast agent, subchondral lesions, which do not contact the joint space, are not visible via arthrography. In fact, in some cases CT may be more accurate due to the general better resolution of the scanner over MRI in current state-of-the-art systems.

While CT is much faster than MRI, the arthrography procedure does have considerable risks in addition to the increased procedure time. These include adverse reactions to injection of the contrast agent, which could mean an allergic reaction to the

contrast solution, or increased risk of infection of the injection site, as well as pain and discomfort in the injected joint. This is in addition to the considerable exposure of patients to ionizing radiation.

Cartilage surface can be visualized, however, with the use of contrast agents via arthrogram. Injection of a radio opaque contrast agent, such as iodine, into the knee joint space and waiting 30-60 minutes for the contrast agent to diffuse for full coverage of the anatomy, allows delineation of the cartilage boundaries.

Chapter 3

Segmentation of Bony Anatomy

3.1 Segmentation using SSM

OA affects most of the tissues of the joint, including cartilage, soft tissues and bone. Therefore, it is critical to automate the capture of as many of these anatomical features as possible when developing a segmentation process for the total knee joint. While many methods exist for segmentation of bony anatomy, it is imperative that the selected method take into consideration that the next segmentation process will benefit from the ability to use the bone segmentation as an initialization or reference, as in [39] or [38]. Obviously, if only the bone or cartilage anatomy is required, any number of methods can be chosen for the task. In general though, segmentation is useful only as a data generator for further analysis, thus a method with the following properties is ideal: the method should (1) make the next segmentation step easier while retaining accuracy, and (2) allow easy analysis of morphological differences across the dataset. For example, if a segmentation algorithm is able to quickly segment 30 bones, but a separate method is required for the cartilage and also requires manual analysis to determine morphological changes, then the "system" quickly becomes overly complex and inefficient.

One such method with the ideal properties is segmentation utilizing SSM, as introduced by Taylor and Cootes [75]. This has been used successfully to extract bone anatomy [37, 38, 47] in healthy patients. First, it is necessary to briefly explain the principles of a basic SSM, as it applies to bone.

3.1.1 Building the SSM

The bone shape model is built upon a database of triangulated meshes which represent the surface of a bone. The statistical bone atlas is formed as described previously by Mahfouz, et al. [76]. In this process, the initial mean template mesh is chosen from the database. All subsequent bone models are then resampled to ensure the same number of vertices are present in addition to having identical connectivity. Additionally, the points on the template model have a one-to-one correspondence with points on other models in the database, which is nontrivial to achieve [77].

The process of obtaining correspondence is a hierarchical one, consisting of linear and non-linear transformations. In the first step, the centroids of the template model and new bone model are aligned. Second, a rigid iterative closest point (ICP) registration is performed as described in [78], followed by an affine transformation. Finally, an iterative non-linear warping, called mutual correspondence warping (MCW) [47], is used to achieve final point correspondences after a smoothing step.

Once correspondences are established, the shape model can be represented as a mean model, μ, computed as the mean of each of the N sets of corresponding vertices. Then a data matrix is constructed as:

$$m_i = \left(\left(x_1^i y_1^i z_1^i \cdots x_N^i y_N^i z_N^i\right) - \mu\right) \quad (1)$$

$$M = [m_1| \cdots |m_B] \quad (2)$$

$$[USV^T] = SVD(M) \quad (3)$$

Here, $\boldsymbol{m_i}$ is the feature vector associated with each of the *B* models, each having *N* points. The singular value decomposition is performed on *M*. By projecting a noisy model having the proper point correspondence onto the space defined by the eigenvectors, using some $1 \leq k \leq B$ PCs, an optimal estimate, in a least-squares sense, of the bone shape is obtained from the shape atlas. The percentage of shape variance captured in the projection increases monotonically with *k*. Therefore, as the model to be projected converges to the true anatomy, the number of PCs used for estimation is increased to refine the accuracy of the projection by increasing the allowed shape variation. Improved point correspondence can be attained using more complex point matching and PC methods, but this is out of the scope of the proposed project.

A shape model can be reconstructed by optimizing the weights in a least-squared sense, so that the reconstruction is written as:

$$\boldsymbol{s} \approx \boldsymbol{\mu} + \sum_{\boldsymbol{i=1}}^{B} b_{\boldsymbol{i}} * \boldsymbol{p_i} \qquad (4)$$

The major properties that make SSM a valuable segmentation and modeling tool are the one-to-one point correspondence, allowing modeling and morphological comparison at fine resolution, and the PC projection, which, as described in the next section, allows shape constraint without complex deformation cost functions, as in active contours. Another important characteristic is allowable shape variance that is stored in the PCs with each subsequent PC contributing some percentage to the total available variance. Good,

although not exact, representations of a candidate bone using only a few PCs can now be reconstructed.

3.1.2 Segmentation with SSM

This section defines an iterative method for segmentation with SSM, building on the work by Merkl, et al. [47]. It should be noted that Fripp, et al. developed a similar method [37], although these surface atlases were combined, so that the pose between tibia, femur and patella, as well as the shapes, were included in a single atlas. It is this author's opinion that utilizing separate atlases and registrations provides more system flexibility with respect to application. Examples of situations wherein it may be advantageous to incorporate separate atlases are when images containing only the femur or tibia can be used or when images provided are poorly positioned (e.g., from an open MRI configuration with some flexion). Optimal shape from the shape model space can be found by iteratively deforming a noisy model and projecting it onto the shape model space (also referred to as the "atlas space") to help constrain the shape to the segmented anatomy. Since available shapes in the atlas are limited to the span of the PC vectors, the patient-specific segmentation requires an additional step, where the final atlas projection is "relaxed," so that each vertex is allowed to deform to the highest-scoring edge location. By using image edges, the segmentation method is independent of image intensity and can be used with CT and many MRI sequencing protocols.

The first modification to the method by Merkl, et al. lies in the registration of the surface atlas with the patient volume. The transformation T_{AP} from the atlas to the patient space is the desired component, and the simplest way to find T_{AP} is to use basic manual

input, where the operator identifies three anatomical landmarks on the patient images which correspond to atlas landmarks, as depicted in Figure 12.

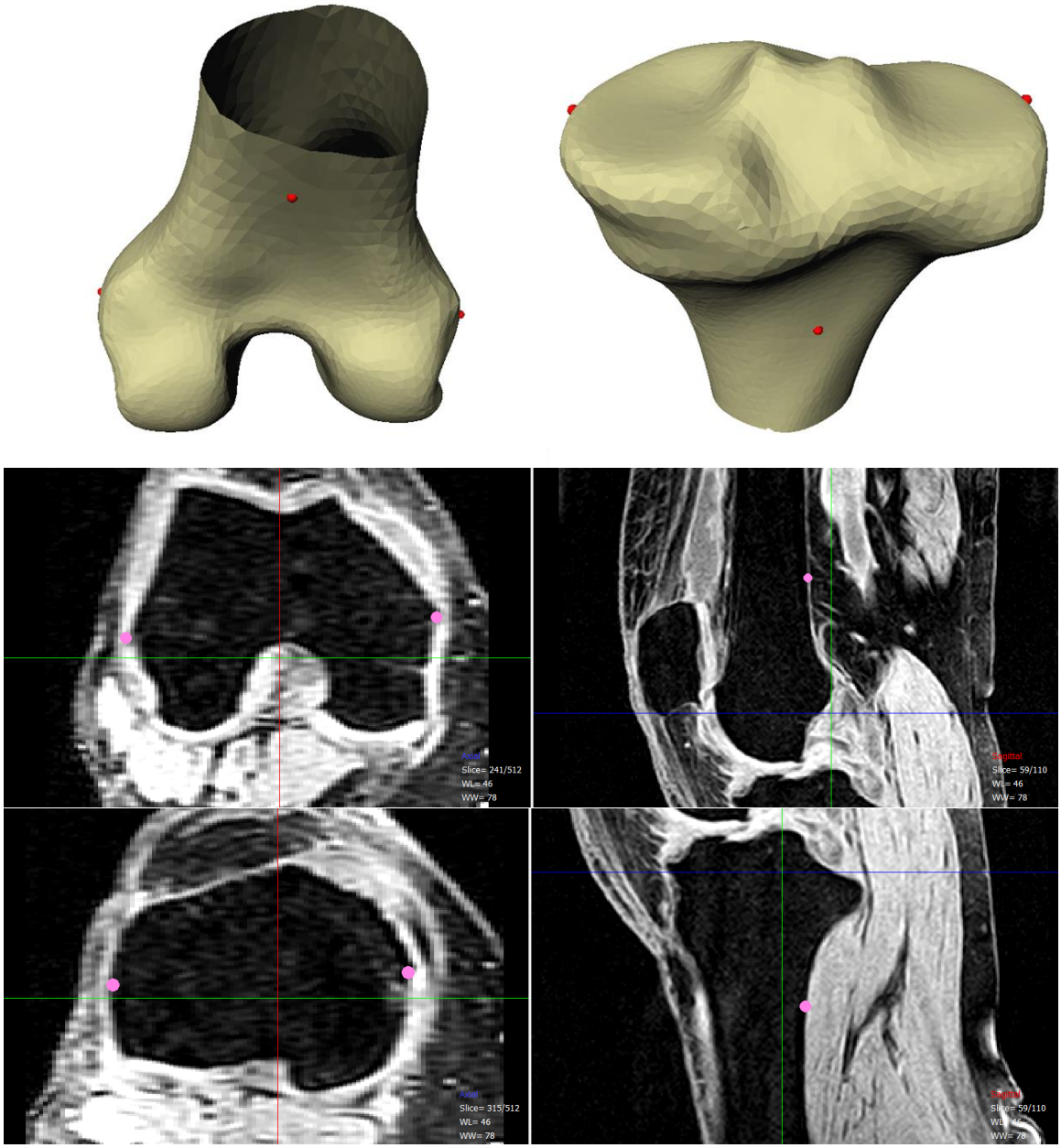


Figure 12. Alignment landmarks on mean surface models (top) and selected on the MRI images for registration (middle and bottom images are femur and tibia, respectively). Transformation between best fit from atlas models and selected points is used for registration of atlas to patient volume.

These landmarks have previously been stored on the atlas mean bone, so that a simple correspondence solution can be solved to obtain the transformation of interest. It should be noted that the mean model may not match the patient anatomy very closely, resulting in a poor registration result. To avoid this, the registration should be performed for every bone in the surface atlas, and the registration resulting in the least error between anatomical points should be kept as the initial model. The transformation should be retained for the iterative step of the algorithm.

After registration is obtained, a projection of a noisy model onto the atlas space as a shape constraining low-pass filter of the image information iteratively determines the optimal shape from the atlas which matches the patient-specific anatomy. An example of the smoothing properties of atlas projection is shown in **Error! Reference source not found.**.

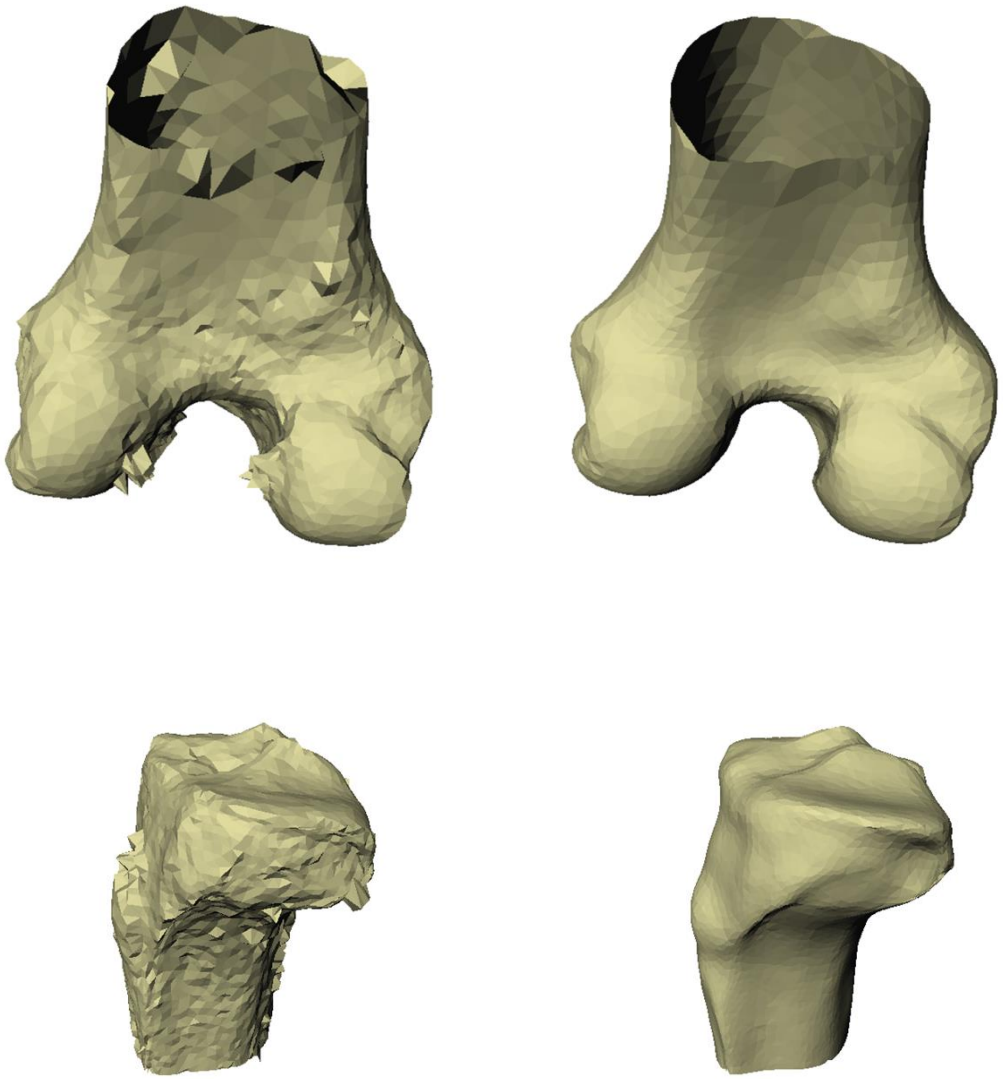


Figure 13. Examples of low-pass filtering properties of projection onto the atlas for femur (top) and tibia (bottom). Noisy models are on the left and model after projection onto the atlas is on the right. Notice significant reduction of noise.

The iterations converge when one of two things occurs, a preset maximum number of iterations is reached or convergence is achieved and the root mean squared error (RSME) between the current iteration and previous iteration is below some threshold.

For each iteration, the following steps are performed:

1) Calculate the normal directions to the surface at each vertex. This is done by averaging the normal directions of connected faces; normal directions should point away from the bone surface; normal directions for a sample bone are shown in Figure 14.

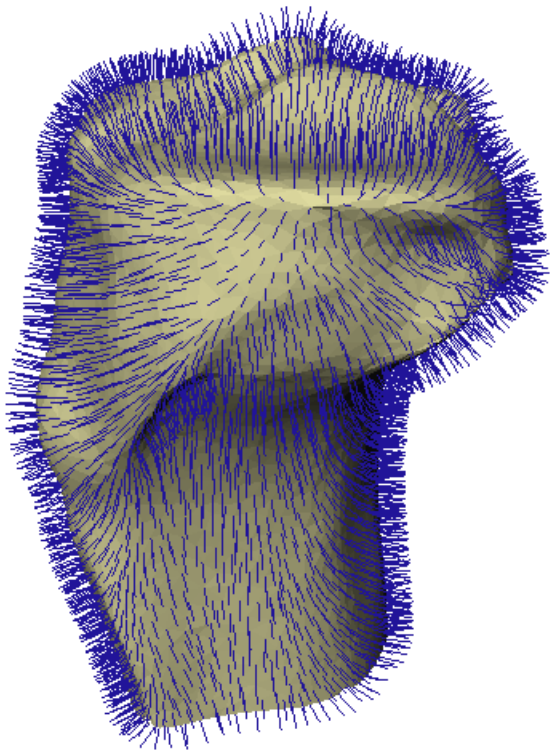


Figure 14. Surface normals at each vertex. Sampling along these profiles is performed to determine the appropriate edge at each vertex.

2) Along each normal direction, sample locations are determined along the ray at a predefined step; this is usually some ratio, r ($0 < r < 1$), of the minimum voxel length. Sampling is performed so the midpoint of the samples is the current bone vertex.
3) At each sample point, linearly (other methods are applicable, although not tested) interpolate image intensity. Image borders are replicated to avoid false edges. This step determines the signal used for edge detection. An example signal is shown in Figure 15.

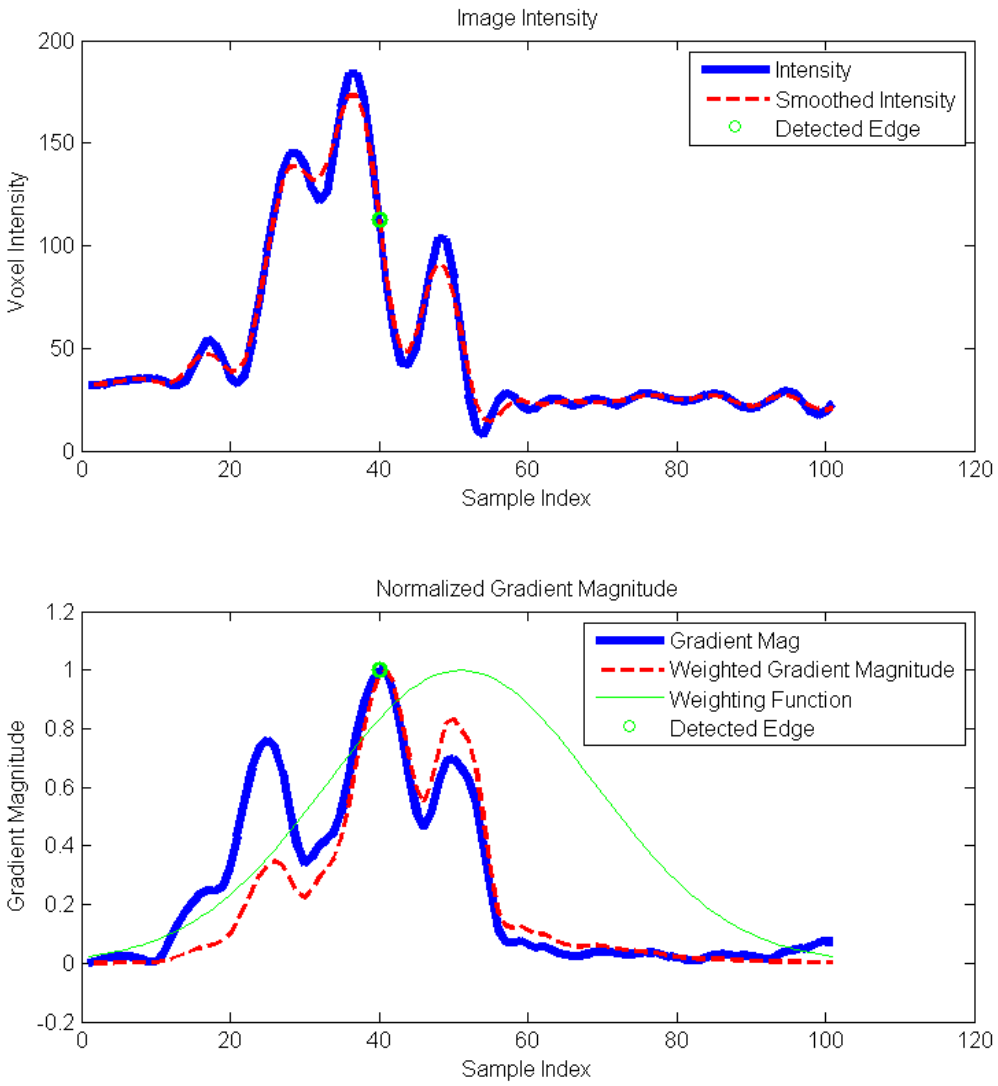


Figure 15. Example intensity signal, smoothing and detected edge for bone segmentation.

4) Image noise is removed by utilizing the Savitzky-Golay algorithm [79]. This filter defines a kernel, which can be used to approximate a local polynomial regression on the kernel window. By solving the regression with a single kernel, smoothing is fast while keeping strong edges.
5) Edges are then taken as the local maxima of the magnitude of the first order image gradient.
6) The signed edges are removed next. For MRI, locations where intensity moves from dark (inside the bone) to bright (soft tissue) are necessary to remove the signed edges. The opposite is true for CT.
7) Edges are scored by gradient magnitude and distance from the bone. Distance weighting is done by multiplication with a Gaussian window centered about the midpoint. The window takes the form of:

$$w(n) = e^{-\frac{1}{2}\left(\alpha\frac{n}{N/2}\right)^2} \quad (5)$$

Here, alpha defines the window width and *N* is simply the total number of points. In this case, *n* is the index relative to the central point. It is possible to choose a different alpha for inside the vertex and one for outside, if it is desired to weight one side more strongly. Weighting is illustrated in Figure 15.

8) Finally, if the statistics have been calculated (iteration > 2), each sample is given a likelihood of belonging to the boundary, based on self-intensity and the nearest two samples. For CT, this is intended to model the similarity of the bony boundary intensities across the anatomy. For MRI, this is intended to guarantee

the best possible results at the BCI surface. This step can be thought of as a dynamic local appearance model in the sense that the appearance model is updated with each iteration.

9) The edge with the highest score based on the following scoring function is kept:

$$S = \alpha G + \beta L \quad (6)$$

Here, alpha ($0 <= \alpha <= 1$) and beta ($\beta = 1 - \alpha$) represent the respective weighting given to the gradient magnitude, *G*, and the appearance likelihood, *L*. The vertex is then moved at the location of the highest scoring edge.

3.2 Anchor Point Refinement

Often, the appearance of the bone-soft tissue interface is poorly defined. This is especially apparent in regions where little to no cartilage is present from degeneration or in the anterior regions of the femur and tibia. The method developed for segmenting these regions accurately is a simple, semi-automated tool using supposed "anchor points," which guides the segmentation by selecting a small cloud of points in the poorly-defined region. These points define the anticipated location of the true bone boundary, but work for all surface vertices within a given diameter – allowing local and non-local refinement in a short period of time.

3.3 Atlas Parameters

The bone atlas is divided by gender and anatomy. The male statistical atlas contains 199 femur and 199 tibia, and the female atlas contains 112 femur and 115 tibia. All atlases of the same anatomy have point correspondence. The femoral atlas bones have 4,120 points, and the tibial atlas bones have 4,812 points. For all bones, variance is shown as a function of PC count in Figure 16 and Figure 17.

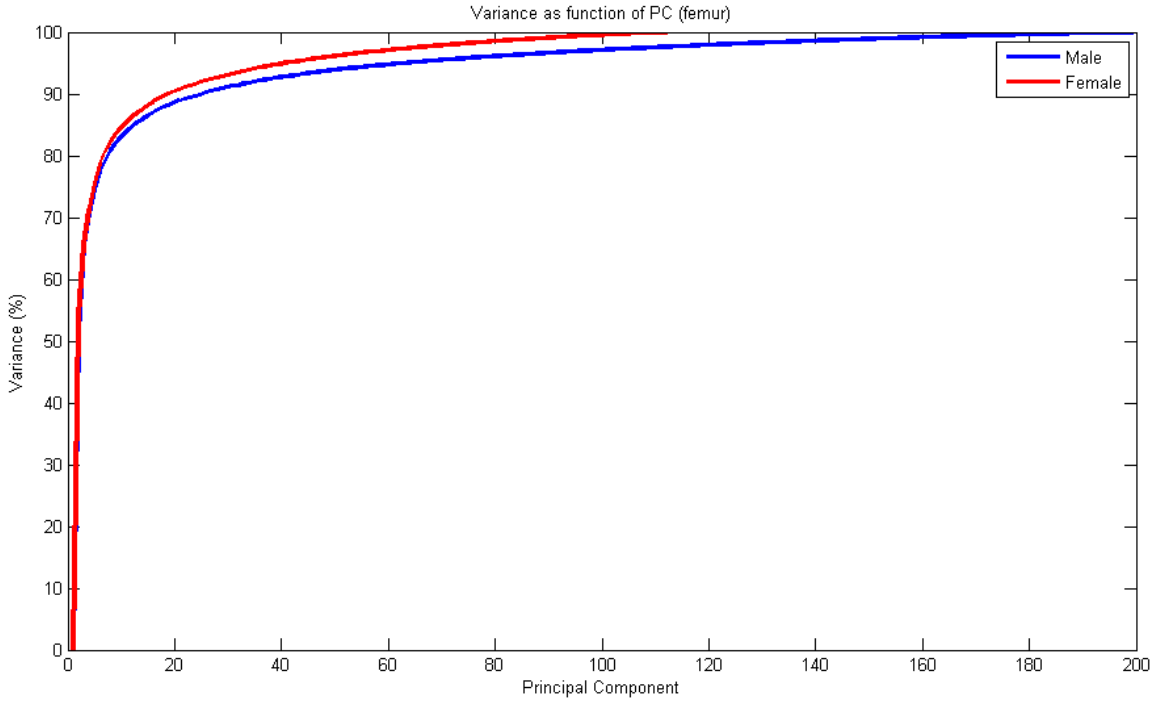


Figure 16. Cumulative variance of PCs for the femur SSM.

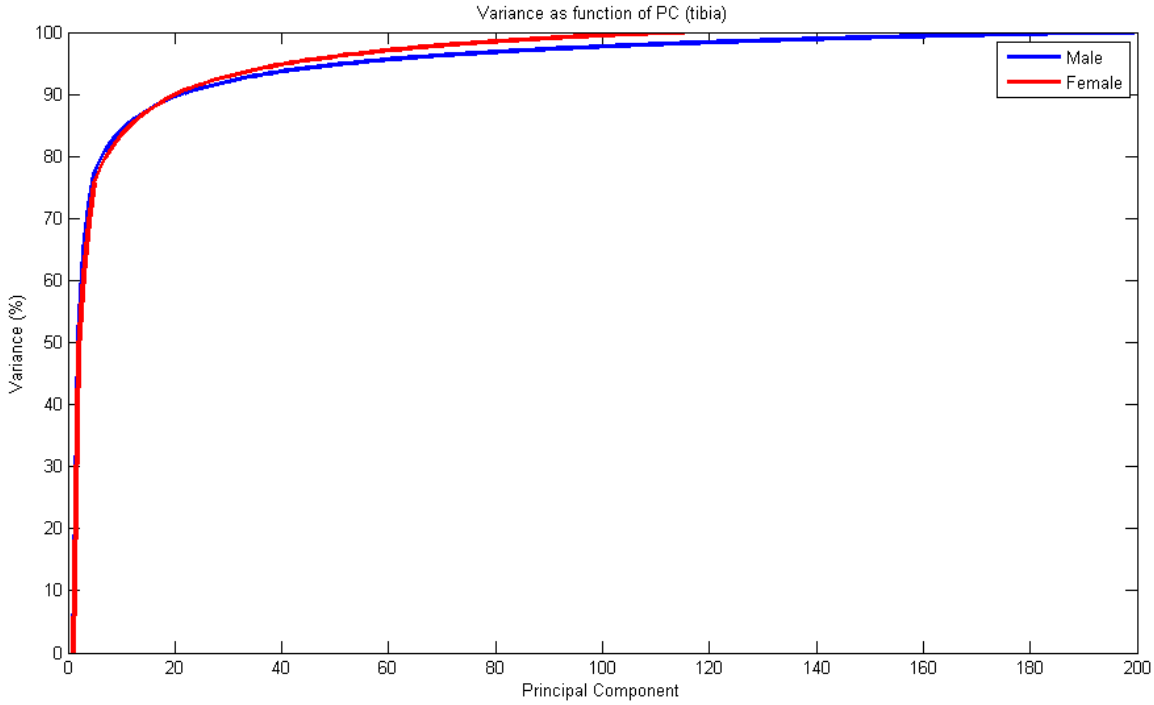


Figure 17. Cumulative variance of principal components for tibia SSM.

3.4 Use of Segmented Bones

The goal of these bone segmentation steps is to provide an accurate patient-specific bone for each case *with atlas correspondence* that can be used as an anchor for cartilage analysis and segmentation. These analyses and segmentations permit modeling the cartilage at each corresponding vertex from the surface atlas, described in subsequent chapters.

Chapter 4

Morphological Changes in Osteoarthritic Knees

4.1 Cartilage Thickness Distribution

Osteoarthritis of the knee brings about many changes in the affected joint, ranging from fluctuations in cartilage distribution, development of osteophytes, or subchondral edemas. Ultimately, these changes lead to, or are brought about by, abnormal kinematic motion. These kinematic changes alter the distribution of stresses on the articulating surface, often leading to suboptimal load distribution. As a knee moves through the various degrees of flexion, the femorotibial contact regions progress from the central compartments of the femur surface to a posterior position. Movement on the contact area on the tibial surface is slightly more complex, but has been defined in several studies. It is likely that this contact pattern, and deviations from the described pattern, can give insight into degenerative changes in OA knees.

In healthy patients, the cartilage thickness is higher in regions which undergo the majority of stresses during normal gait [80]. Furthermore, Li, et al. showed that the cartilage-to-cartilage contact regions were associated with the thickest cartilage [6]. Wirth and Eckstein, et al. further studied cartilage loss in the femorotibial joint in OA subjects by segmenting the cartilage plates and assigning regions for examination [81, 82]. The regions on the articulating surfaces, defined for the femur and the tibia, were located relative to manually selected landmarks as described in [27]. The findings by Wirth suggest that centrally located compartments of both joints undergo the majority of

cartilage wear. There are, however, some shortcomings in the works of Wirth and Eckstein, such as poor resolution and reduced study reproducibility due to manually defined landmarks – both of which can be overcome using SSMs. Mahfouz et al. have used high resolution SSM of the bony anatomy to perform morphological analyses [83] across gender and ethnicities [84, 85] . Similar SSM of the bone can be used to drive the morphological cartilage analyses, not unlike Fripp [86], who used SSM for cartilage segmentation and Williams [87], who used some form of SSM for morphological analysis, but reported overly thick cartilage (approximately 25 mm in patellar groove).

Tibiofemoral contact regions are relatively small when compared with overall articulating surface size. The problematic issue of resolution lies in the comparison of results from the kinematic data to the rather large compartments used in the analysis by Wirth. For example, the contact regions of the medial tibia appear to lie partially inside the central tibial plate and one or more of the surrounding regions. Therefore, it is unknown if the cartilage wear is in regions associated with contact areas about which data is currently known. This work seeks to answer several questions regarding morphological cartilage analysis and changes related to OA. First, the cartilage wear maps will be generated for varus, valgus and neutral knees. Second, these wear patterns will be generated using high resolution methods by utilizing SSMs and associated point correspondences. Finally, these wear patterns will be associated with known kinematic contact regions.

4.2 Methods

4.2.1 Subject Selection

All subjects were from the existing OAI, jointly sponsored by the National Institutes of Health, the National Institute of Arthritis and Musculoskeletal and Skin Diseases and the pharmaceutical industry. The OAI acquires all images at 3.0 T using 3D DESS with thin sections, obtaining nearly isotropic voxels, allowing for excellent assessment characteristics in all three common reconstruction directions (i.e., sagittal, axial and coronal). Voxel size for all images was 0.7 mm x 0.365 mm x 0.365 mm, providing adequate resolution for segmentation of cartilage anatomy. Image sizes were 384 x 160 x 160. Healthy subject were those with KL score of 0, while degenerative subjects were considered as KL score of 1 or above. For healthy subjects, 40 male and 40 female were used – divided by gender, with demographics as listed in Table 3.

Table 3. Subject demographics for healthy cartilage dataset.

	Caucasian Male	***Caucasian Female***
Average Age (years)	63	63
Age Range (years)	47 - 76	45-77
Number Right	26	30
Number Left	14	10
Average Year of Birth	1942	1942

For cases with degeneration in one or both tibiofemoral compartments, the demographics of all selected patients are listed in Table 4.

Table 4. Subject demographics for cartilage datasets with degeneration.

	Caucasian Male	***Caucasian Female***
Average Age (years)	63	65
Age Range (years)	48 - 78	46-78
Number Right	19	19
Number Left	3	7
Average Year of Birth	1942	1940

The total number of patients in each group, as divided by compartment of wear and KL score is listed in Table 5 and Table 6.

Table 5. Makeup of male subject dataset by KL score and compartment of degeneration.

Male	**KL1**	**KL2**	**KL3**	**Total**
Varus	5	3	2	**10**
Valgus	2	1	5	**8**
Neutral	2	1	1	**4**
Total	**9**	**5**	**8**	**22**

Table 6. Makeup of female subject dataset by KL score and compartment of degeneration.

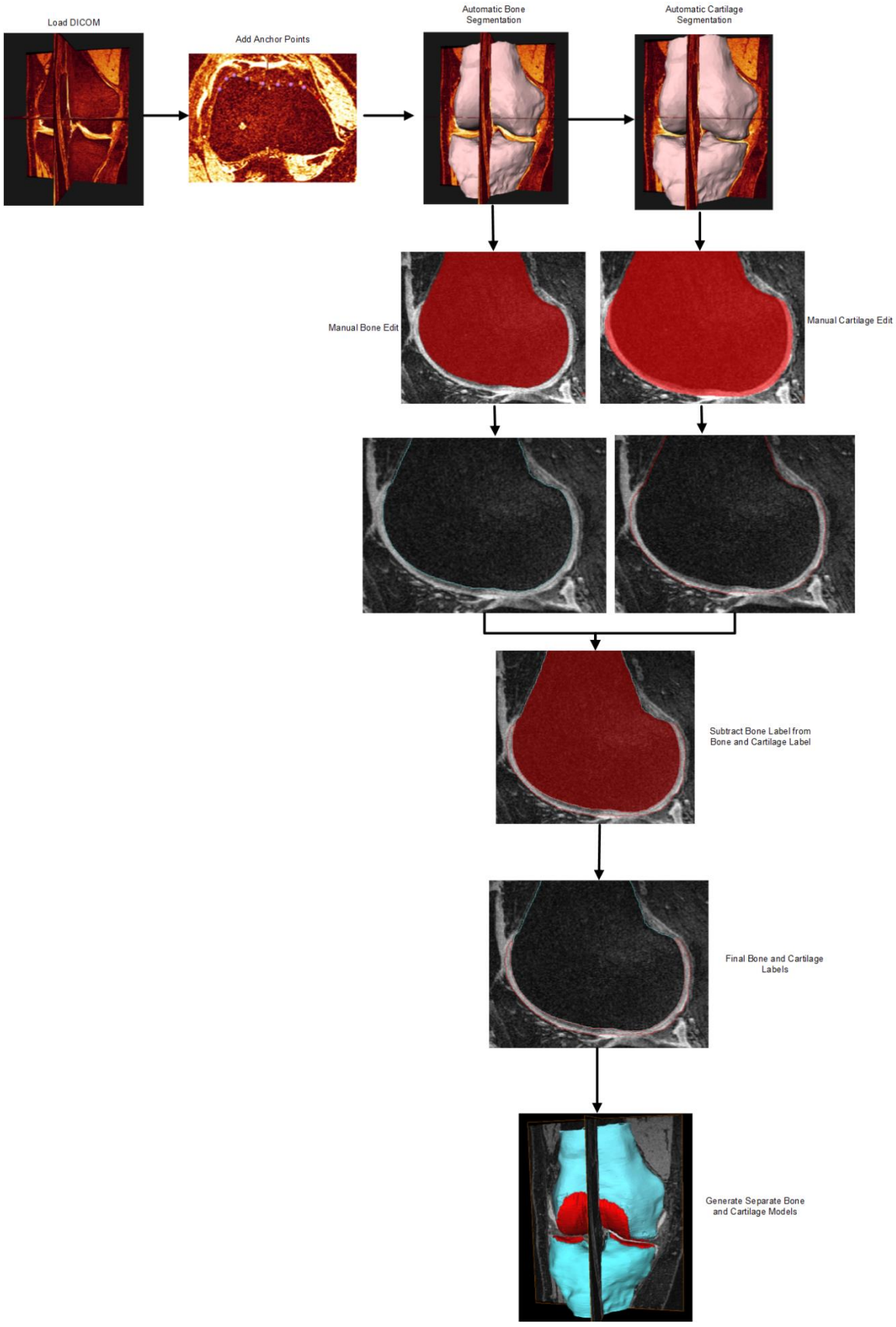
Female	**KL1**	**KL2**	**KL3**	**Total**
Varus	5	2	3	**10**
Valgus	2	4	4	**10**
Neutral	1	3	2	**6**
Total	**8**	**9**	**9**	**26**

Data for these analyses are from the OAI public use data set(s). The OAI is a public-private partnership comprised of five contracts (N01-AR-2-2258; N01-AR-2-2259; N01-AR-2-2260; N01-AR-2-2261; N01-AR-2-2262) funded by the National Institutes of Health, a branch of the Department of Health and Human Services, and conducted by the OAI Study Investigators. Private funding partners include: Merck Research Laboratories; Novartis Pharmaceuticals Corporation, GlaxoSmithKline; and Pfizer, Inc. Private sector funding for the OAI is managed by the Foundation for the National Institutes of Health. This manuscript was prepared using an OAI public use data set and does not necessarily reflect the opinions or views of the OAI investigators, the NIH, or the private funding partners.

4.2.2 Cartilage Thickness Calculation

For all cases in the dataset, cartilage thickness was calculated at each location belonging to the possible BCI on the bone surfaces from the statistical atlas. This was done using a multi-tiered, semi-automated segmentation approach consisting of automatic bone segmentation, as described in Chapter 3, followed by a manual cartilage segmentation step, and finally, processing of the segmented labels as depicted in **Error! Reference source not found.**.

Figure 18. Semi-automatic segmentation of bone and cartilage from MRI images from the OAI dataset. The first step is to utilize the segmentation algorithm in Chapter 3 to segment the bone and cartilage data. Any remaining errors are then manually segmented using available tools. The resulting labels after the manual step represent the bone and the bone + cartilage. Subtraction of the two labels allows accurate cartilage reconstruction while guaranteeing accurate BCI for thickness and location calculations.


Load DICOM
Add Anchor Points
Automatic Bone Segmentation
Automatic Cartilage Segmentation
Manual Bone Edit
Manual Cartilage Edit
Subtract Bone Label from Bone and Cartilage Label
Final Bone and Cartilage Labels
Generate Separate Bone and Cartilage Models

For each case, after the resulting bone model has been converted to have atlas correspondence, the bone segmentation is used as the "anchor" for cartilage thickness and bone-cartilage interface determination. Cartilage thickness at each vertex on the bones must now be determined. For each BCI vertex, v_i, defined as a bone vertex with cartilage present along the normal direction from the bone, there is an associated thickness statistics (mean and standard deviation), as well as probability, of cartilage being present. Cartilage thickness for each subject is calculated as follows:

1) Use atlas based segmentation with anchor points to segment the bone data with point correspondence with the statistical atlas (Chapter 3).
2) Add cartilage layer to bone segmentation using semi-automatic segmentation tools.
3) Subtract bone + cartilage mask from bone mask to obtain cartilage mask only.
4) Project rays normal to the bone surface and sample cartilage mask at sufficiently high frequency (0.1 mm in this case) at every bone vertex.
5) Add all vertices with at least one sample point inside of the cartilage mask to the BCI list.
6) For each vertex profile, extract first intersection point and next intersection point with a subsequent miss. The distance between these two points corresponds to cartilage thickness at the vertex.

This procedure was conducted for all cases in the dataset, and each bone vertex has an associated cartilage thickness. Mean thickness was determined at each vertex for each

dataset. Osteoarthritic data was divided by affected compartment and classification, whereas healthy data was divided by gender.

4.2.3 Cartilage Thickness Analysis

For each case in the pathological datasets, the thickness at each vertex was normalized by the mean healthy thickness of the associated gender (male knees normalized by healthy male thickness, female by healthy female). This gave a mean fractional wear associated with each vertex for all OA cases, mean cartilage thickness maps were generated for all data.

4.3 Results

4.3.1 Healthy Cartilage

The following images give quantitative maps of the cartilage at each vertex on the statistical atlas. From these results, a standard to which degenerative cartilage may be compared has been established.

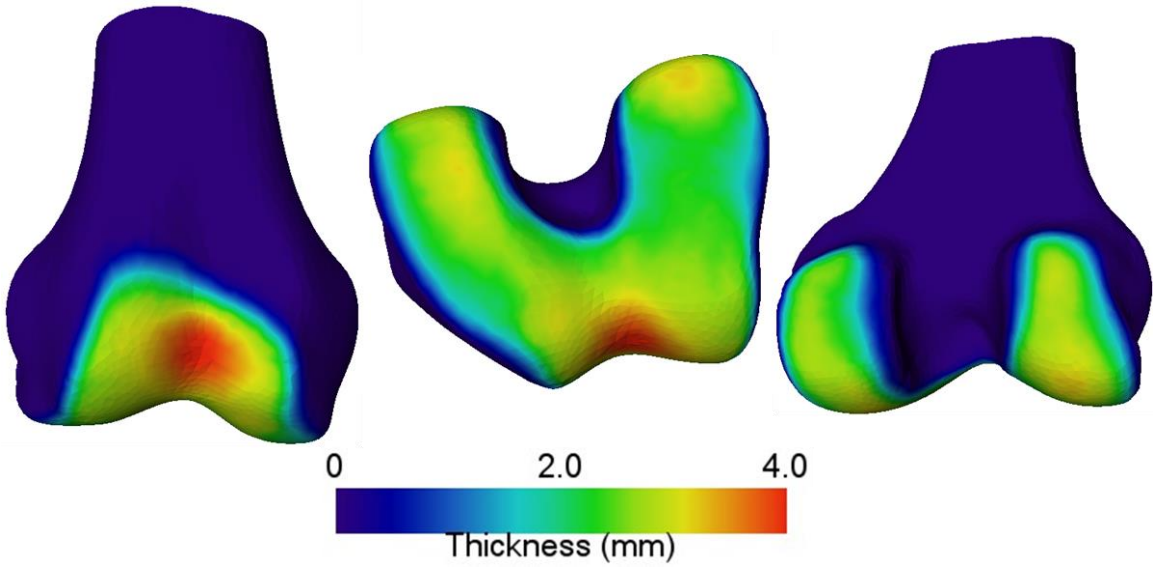


Figure 19. Mean cartilage thickness for Caucasian male femur.

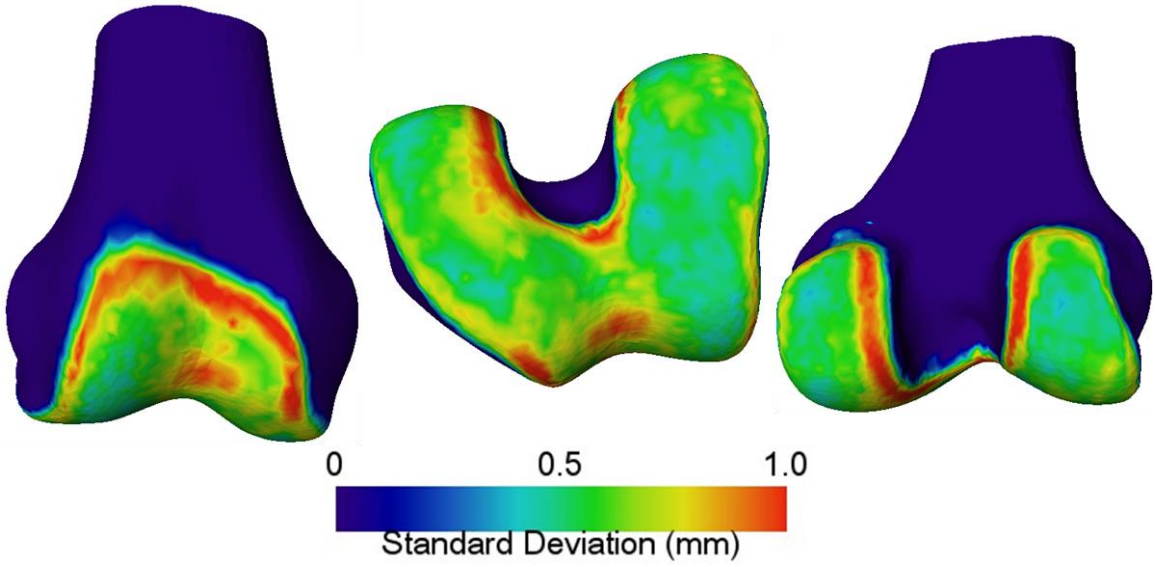


Figure 20. Standard deviation of cartilage thickness for Caucasian male femur.

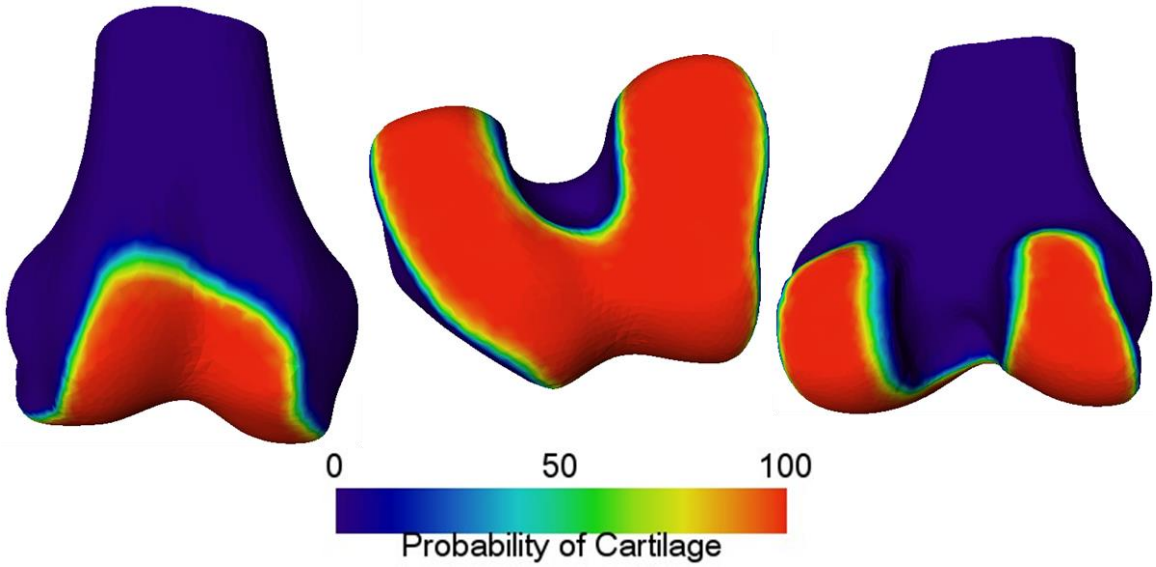


Figure 21. Probability map for femoral cartilage presence on Caucasian male femur.

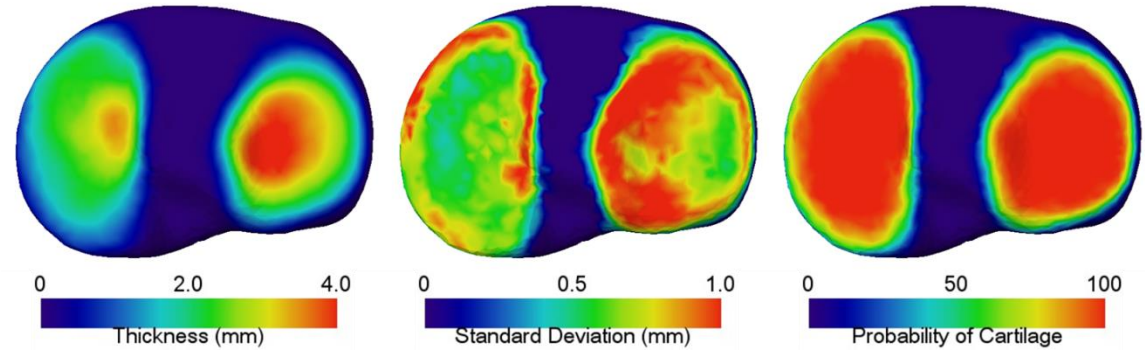


Figure 22. Mean thickness (left), standard deviation (middle) and probability (right) of Caucasian male tibia cartilage.

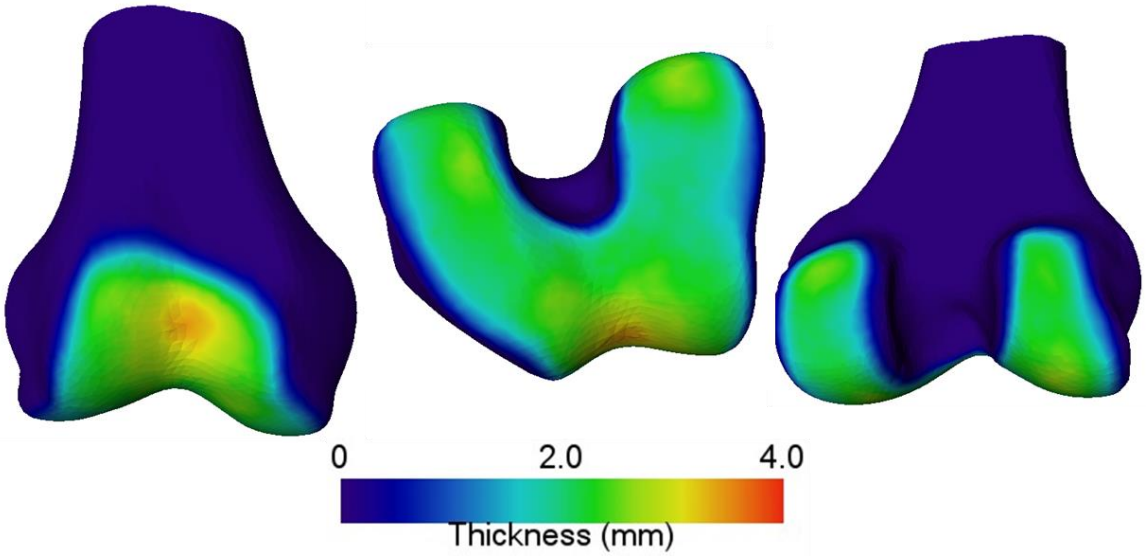


Figure 23. Mean cartilage thickness for Caucasian female femur.

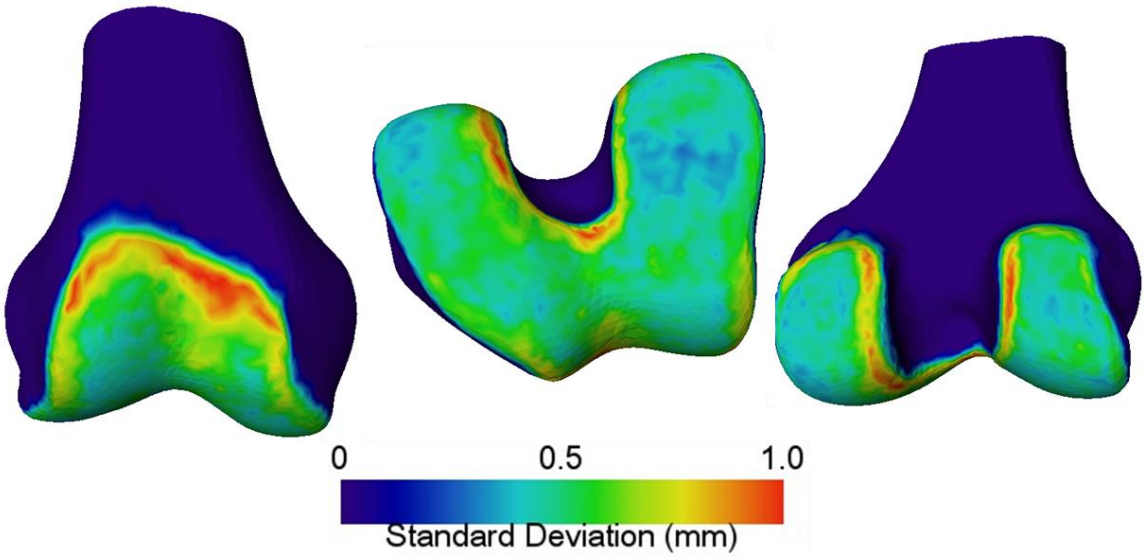


Figure 24. Standard deviation of cartilage thickness for Caucasian female femur.

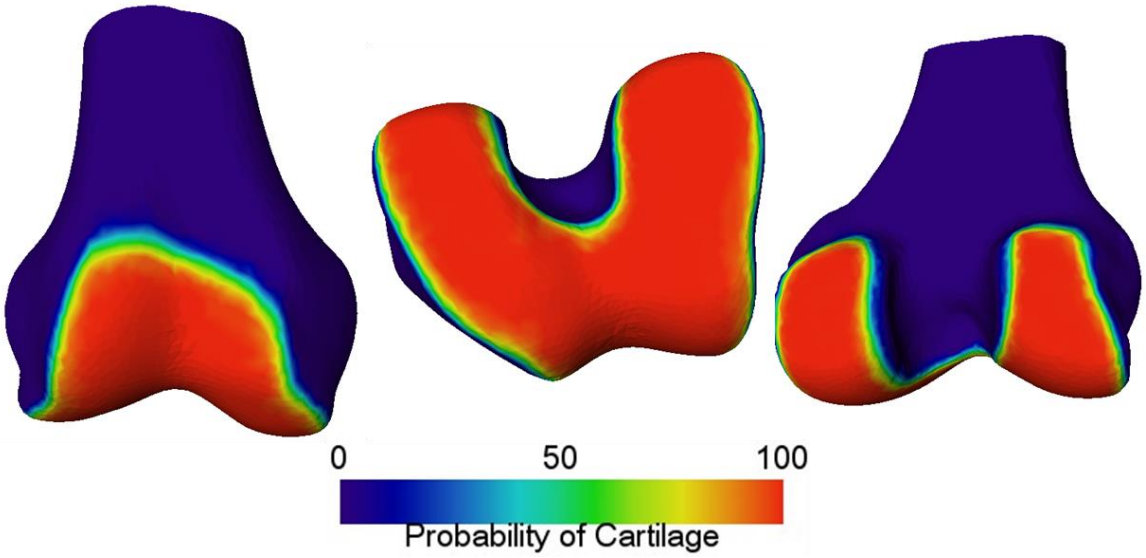


Figure 25. Probability of cartilage presence for Caucasian female femur.

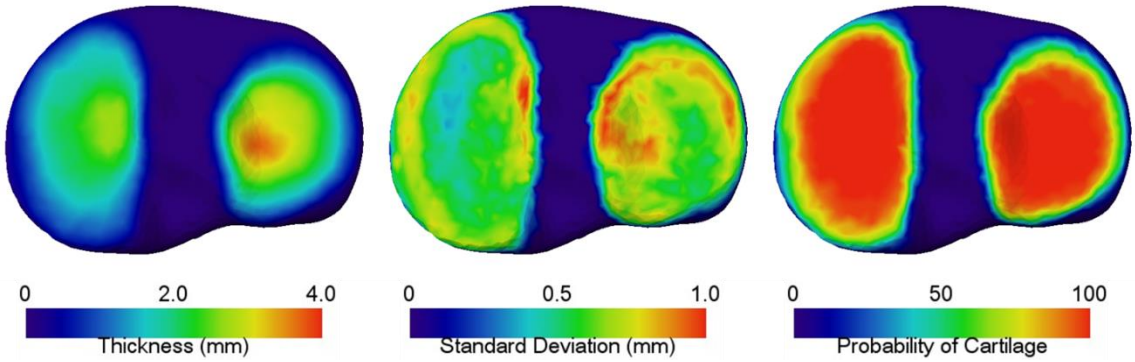


Figure 26. Mean thickness (left), standard deviation (middle) and probability (right) of Caucasian female tibia cartilage.

Table 7. Global quantitative results for cartilage tissue in healthy male and female.

Gender	Bone	Volume (voxels)	Mean thickness (mm)
Male	Femur	$1.627 * 10^5$	1.93
Female	Femur	$1.114 * 10^5$	1.59
Male	Tibia	$6.420 * 10^4$	1.42
Female	Tibia	$4.285 * 10^4$	1.16

4.3.2 Osteoarthritic Cartilage Maps

The following cartilage maps represent those found in various degrees of degeneration, as divided by compartment and classification level (KL). In addition to basic statistics, the normalized fraction of the healthy mean map is likewise reported.

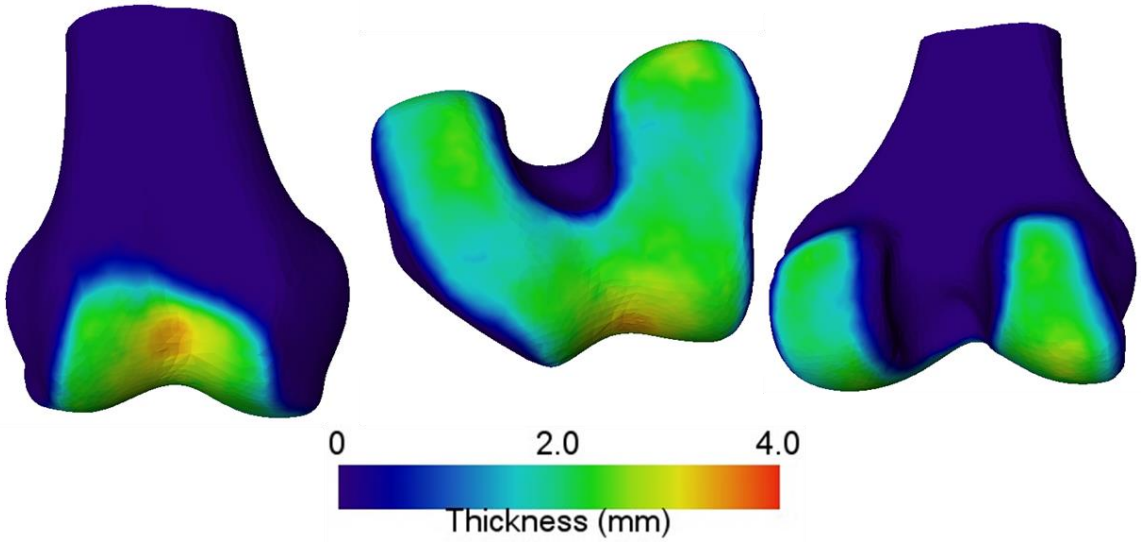


Figure 27. Mean cartilage thickness of KL-1 grade femur.

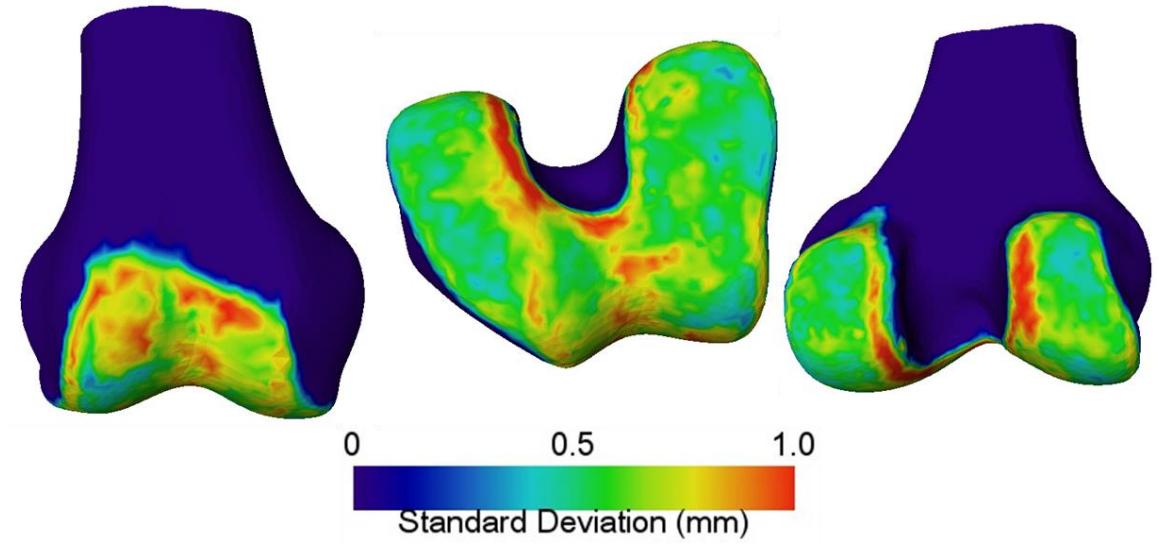


Figure 28. Standard deviation of cartilage thickness for KL-1 grade femur.

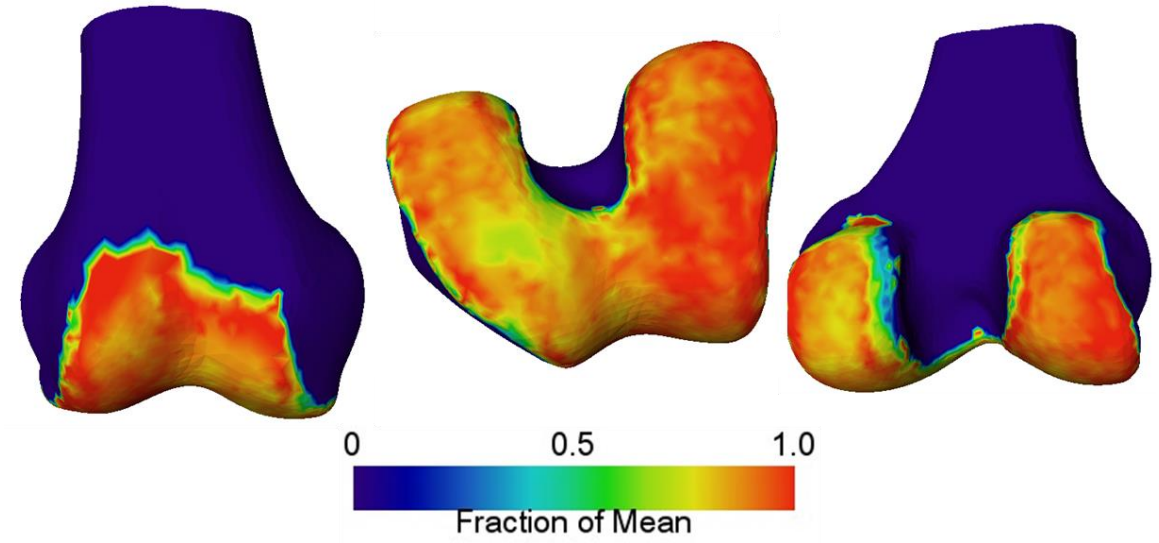


Figure 29. Normalized fraction of mean healthy (KL-0) thickness for KL-1 grade femur.

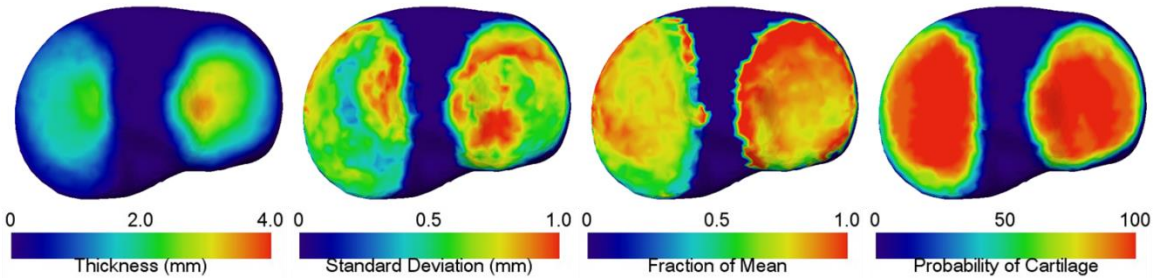


Figure 30. Cartilage for KL-1 grade tibia.

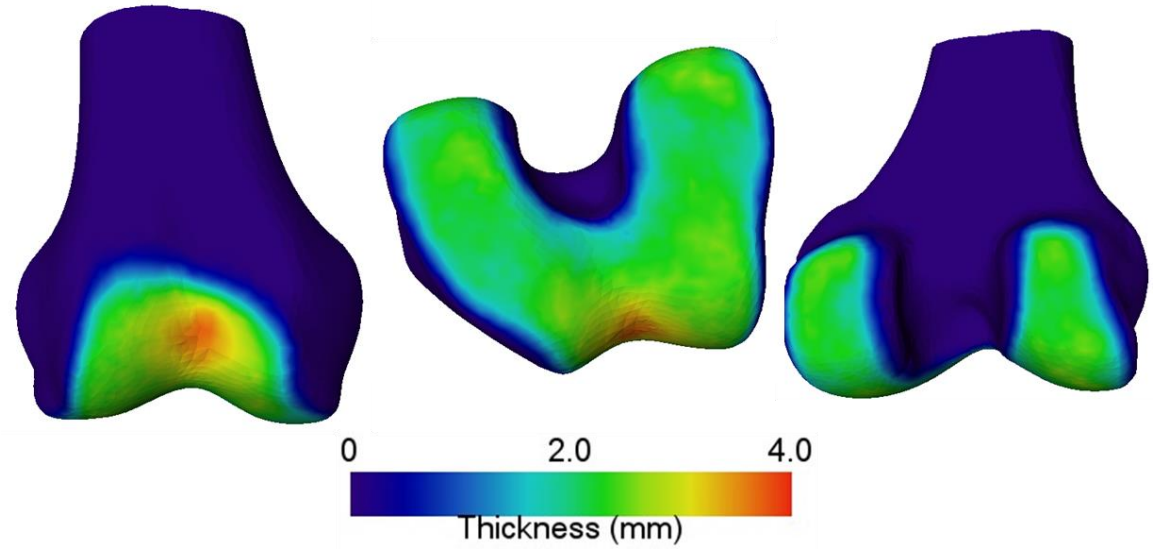


Figure 31. Mean cartilage thickness for KL-2 grade femur.

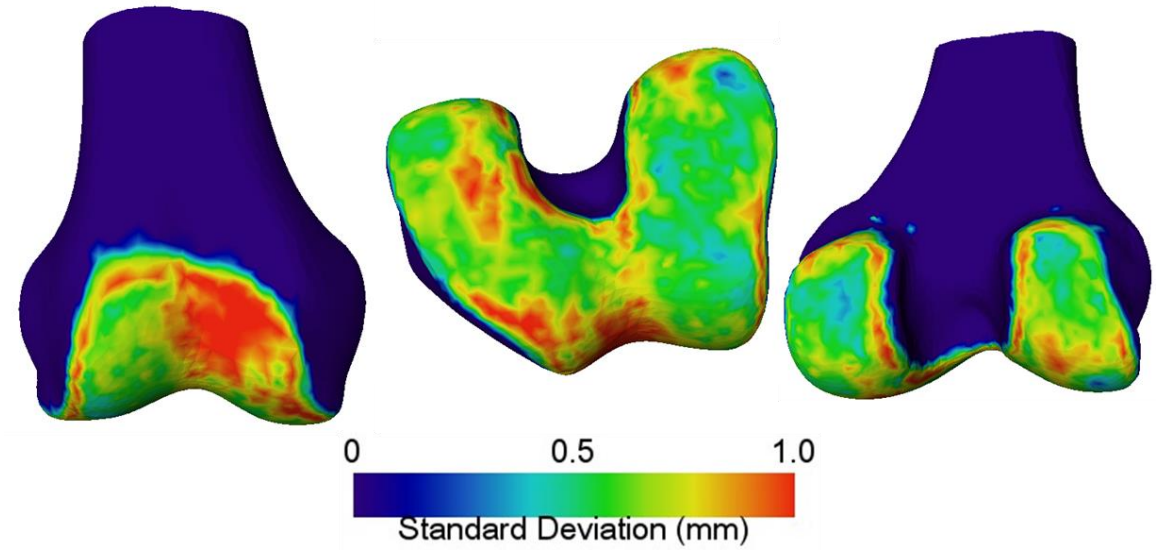


Figure 32. Standard deviation of cartilage thickness for KL-2 grade femur. Note that despite thickness map appearing to be nearly normal, the deviation in the patellofemoral region is high.

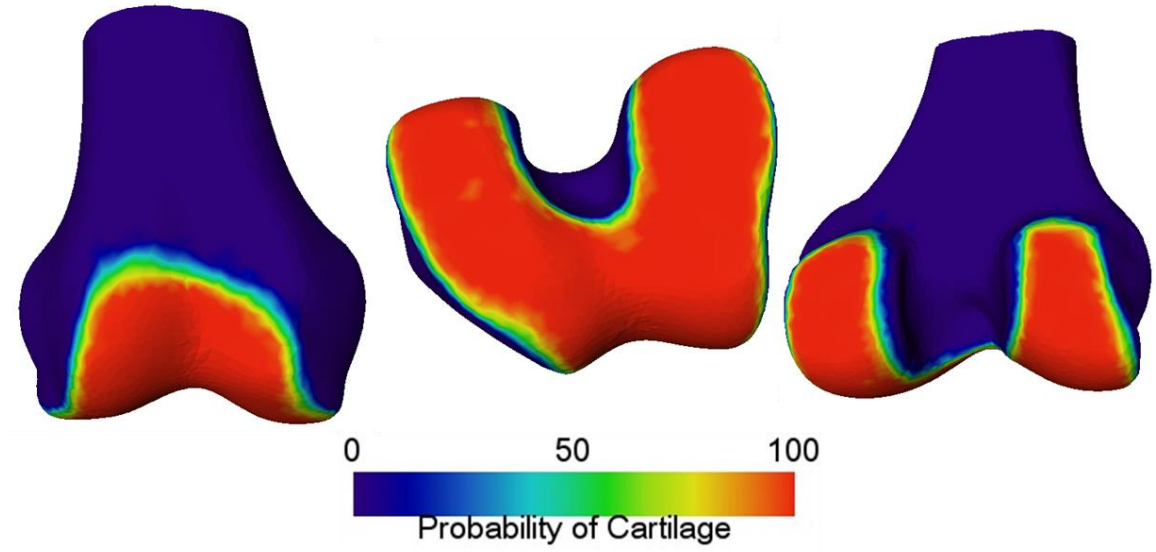


Figure 33. Probability of cartilage presence for KL-2 grade femur. Note some patches of missing cartilage in the medial compartment.

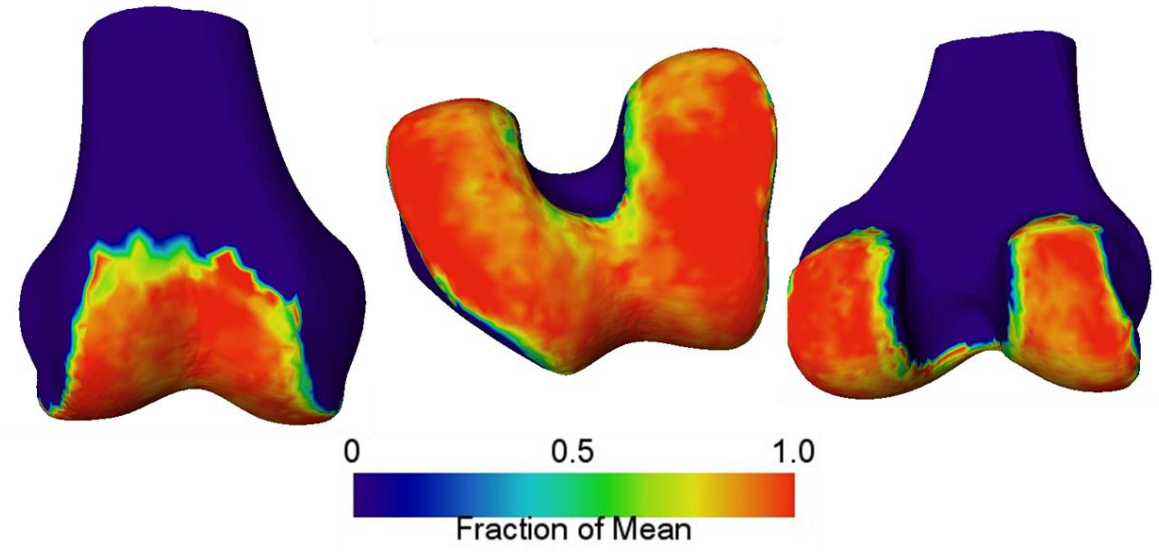


Figure 34. Normalized fraction of mean healthy (KL-0) thickness for KL-2 grade femur.

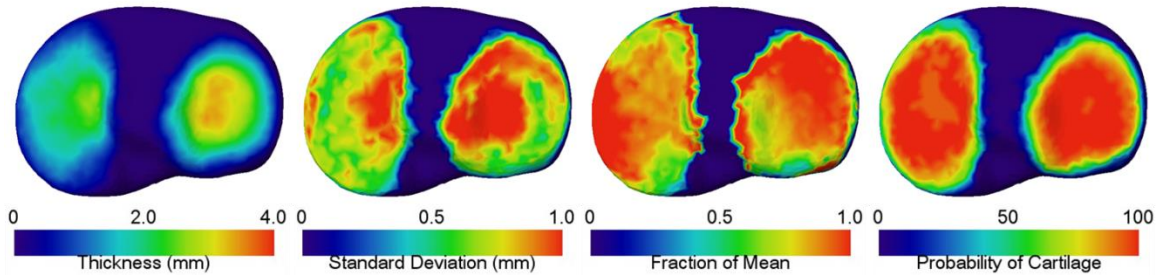


Figure 35. Cartilage for KL-2 grade tibia.

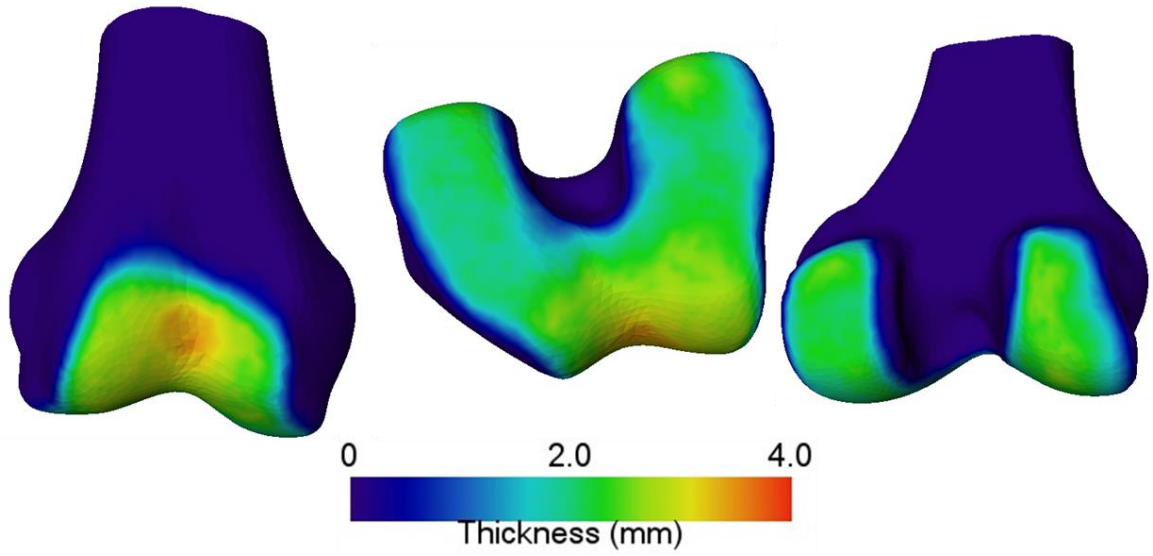


Figure 36. Mean cartilage thickness for KL-3 grade femur.

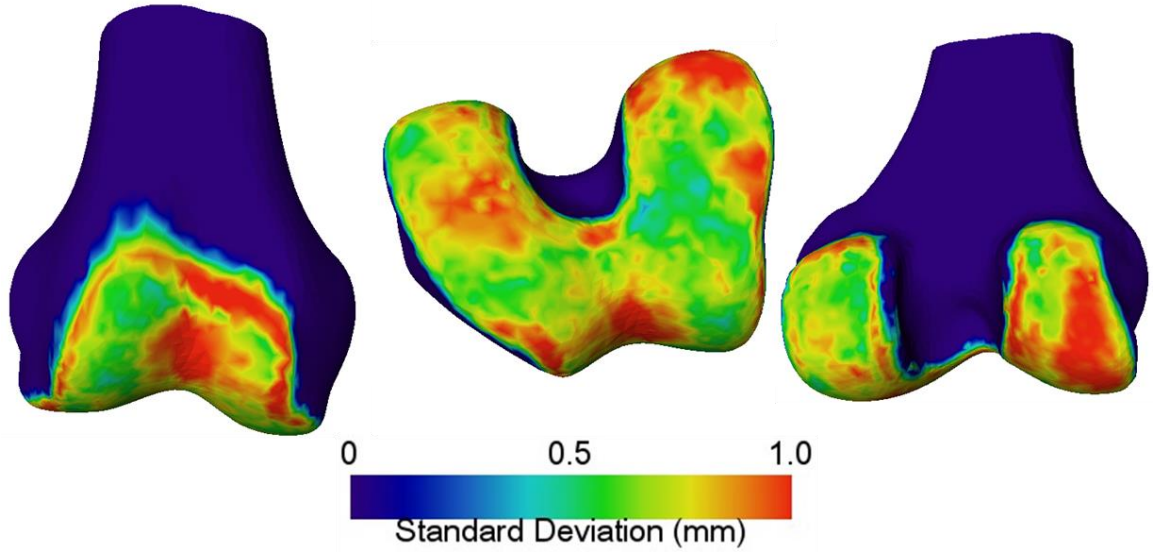


Figure 37. Standard deviation of cartilage thickness for KL-3 grade femur.

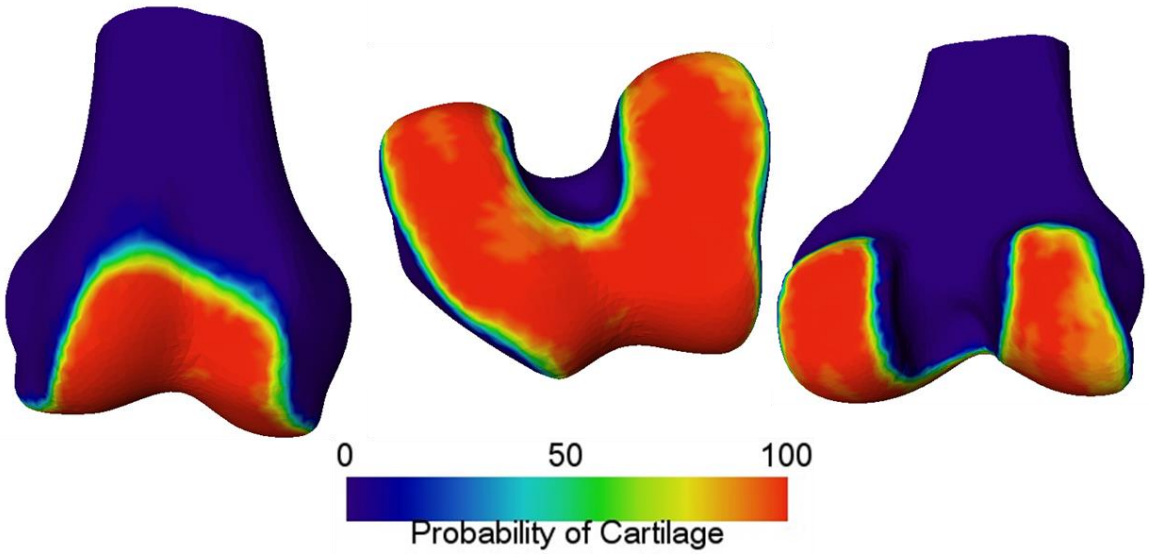


Figure 38. Probability of cartilage presence in KL-3 grade femur. Notice the higher probability of missing cartilage than in KL-2 femurs, as expected.

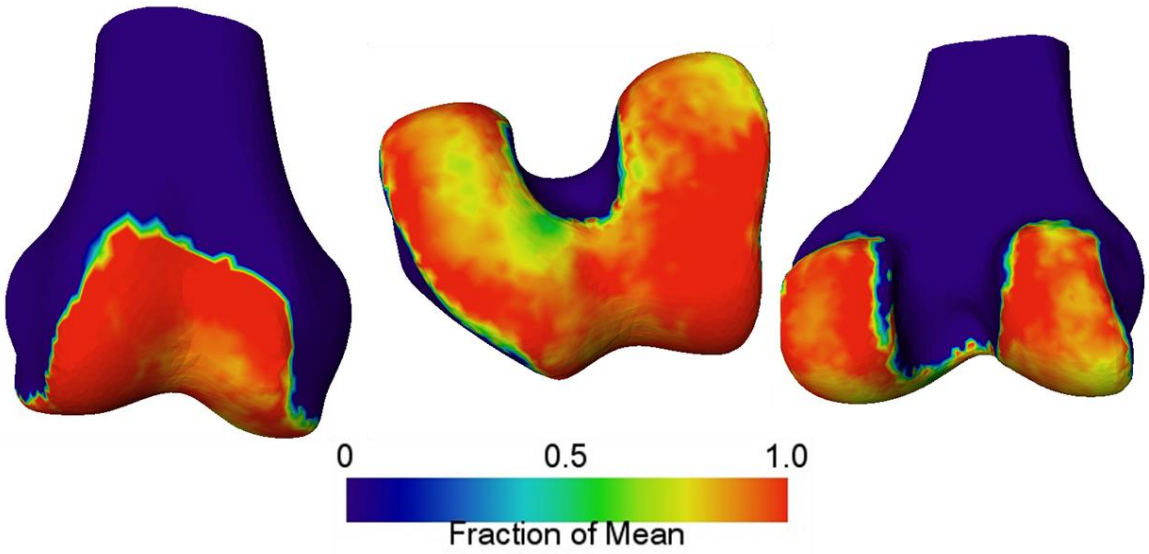


Figure 39. Normalized fraction of mean healthy (KL-0) cartilage thickness for KL-3 femur.

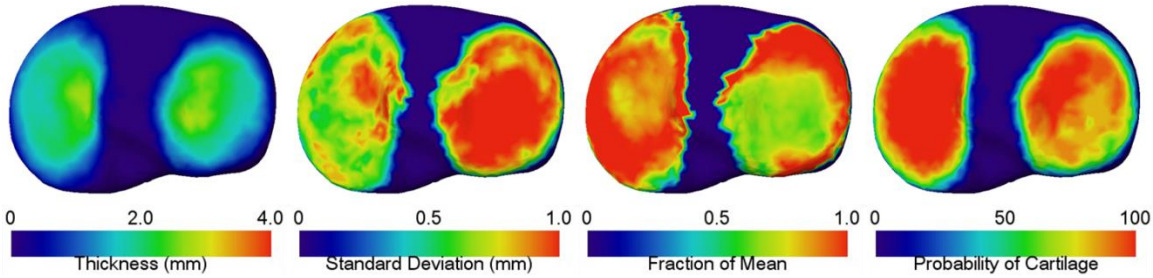


Figure 40. Cartilage for KL-3 grade femur.

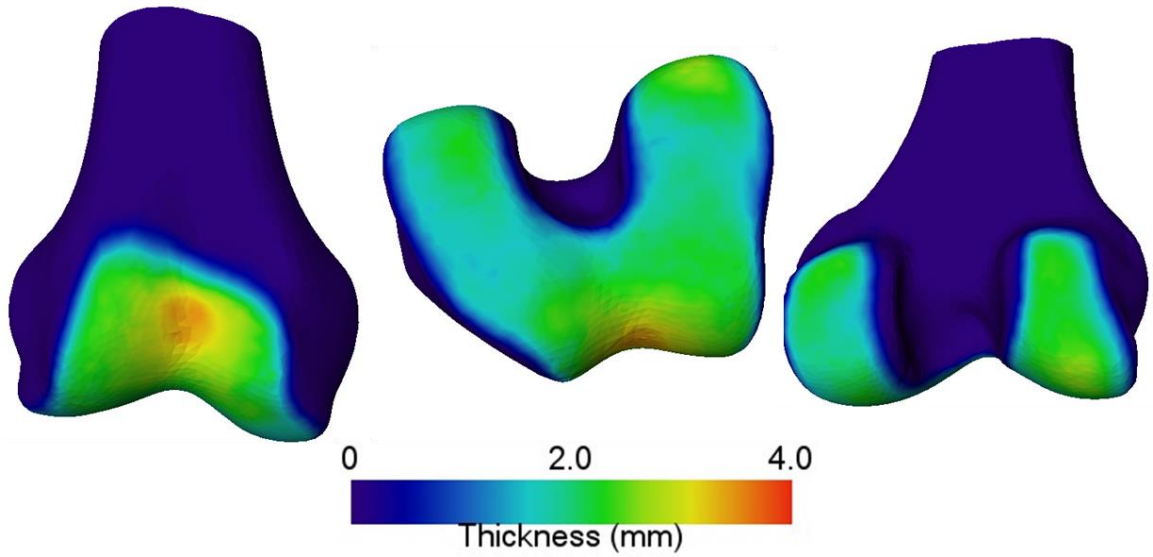


Figure 41. Mean femoral cartilage thickness for cases with varus defects. Note thin cartilage in medial tibiofemoral compartment.

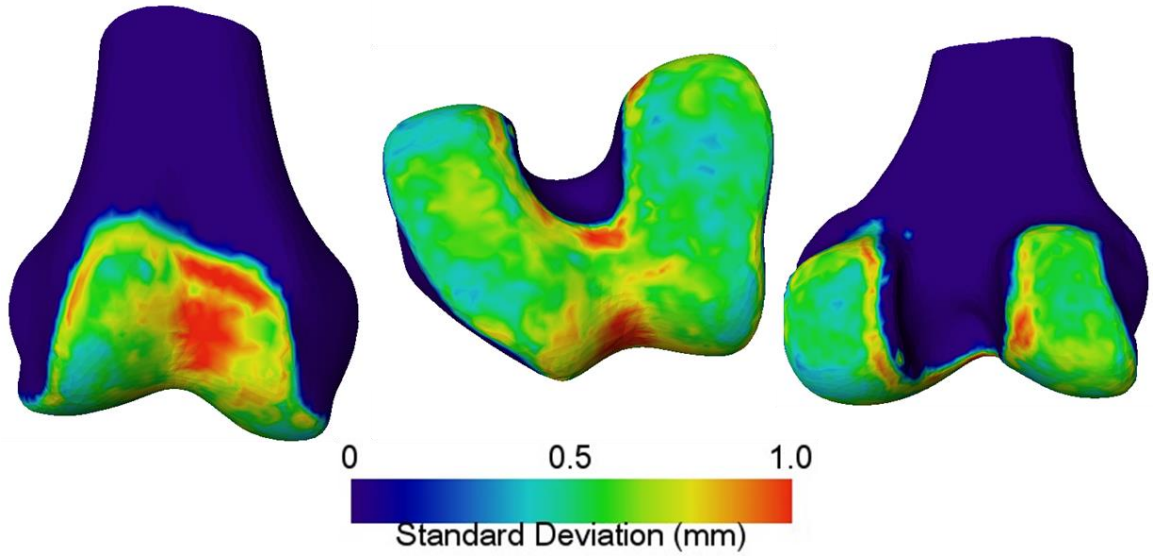


Figure 42. Standard deviation of femoral cartilage thickness for cases with varus defects.

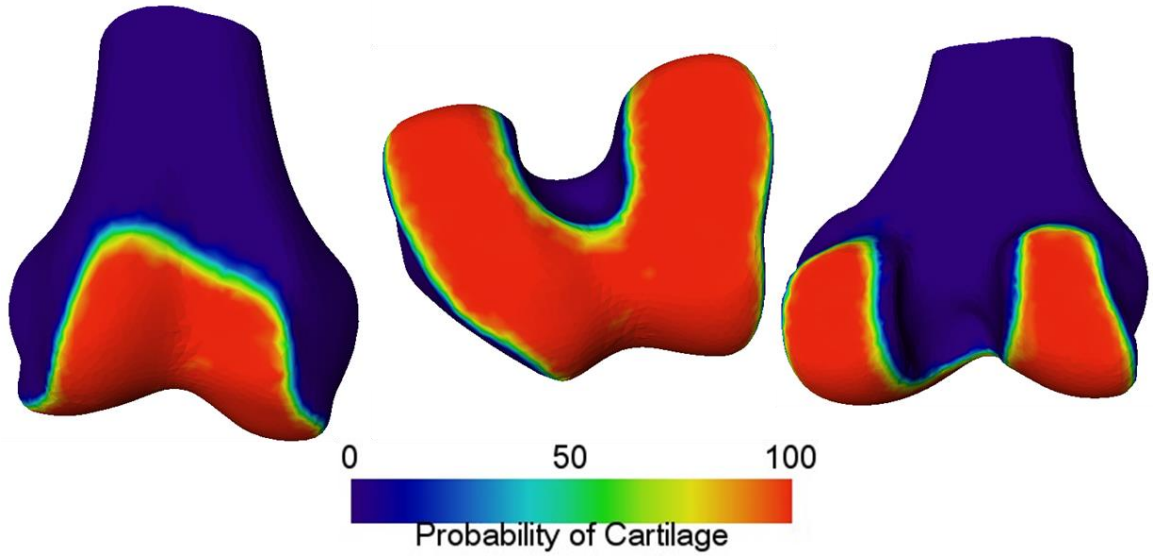


Figure 43. Probability of femoral cartilage for varus knees.

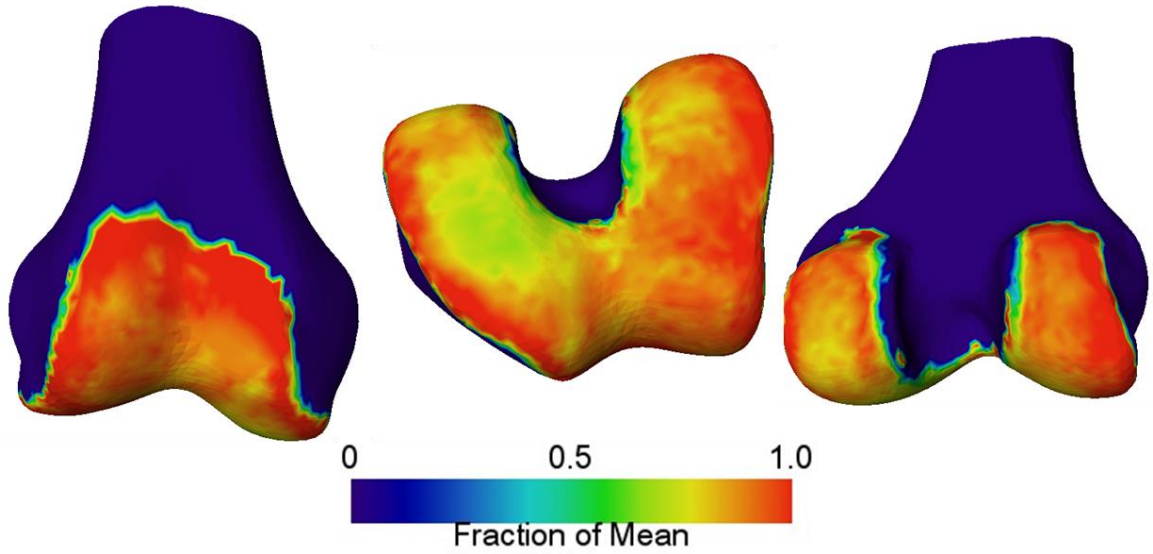


Figure 44. Normalized fraction of healthy thickness for femoral cartilage in varus knees. Note significant cartilage wear in the medial tibiofemoral compartment, which is expected in knee joints with varus malalignment.

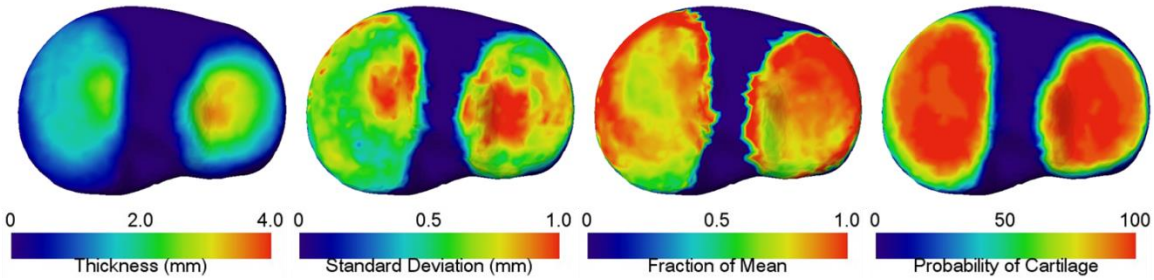


Figure 45. Cartilage for tibia in varus knees. Note majority of tibia wear is in the medial compartment.

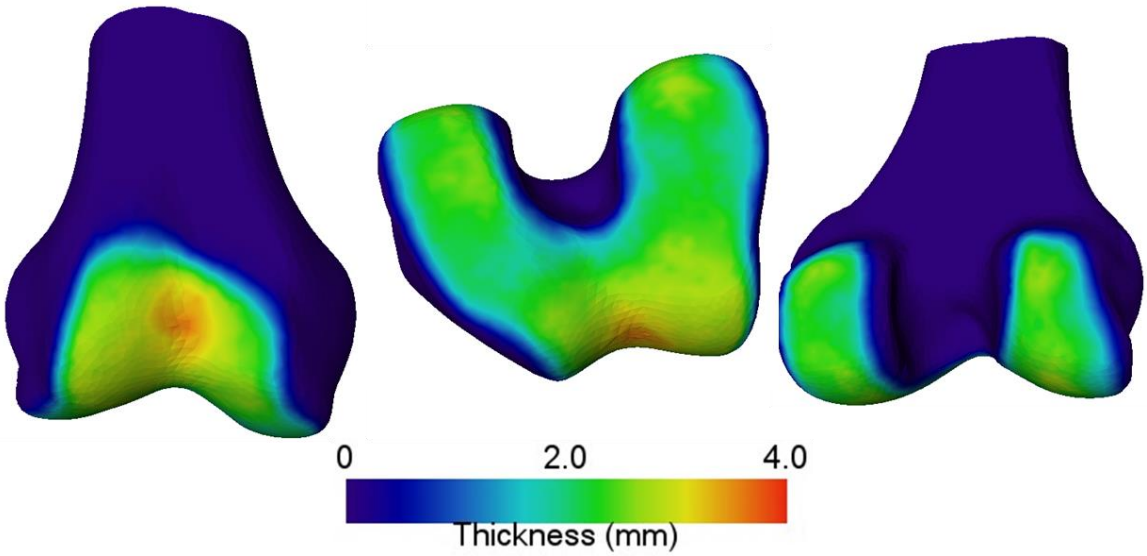


Figure 46. Mean femoral cartilage thickness in knees with valgus defects. Note that the femoral cartilage looks nearly healthy.

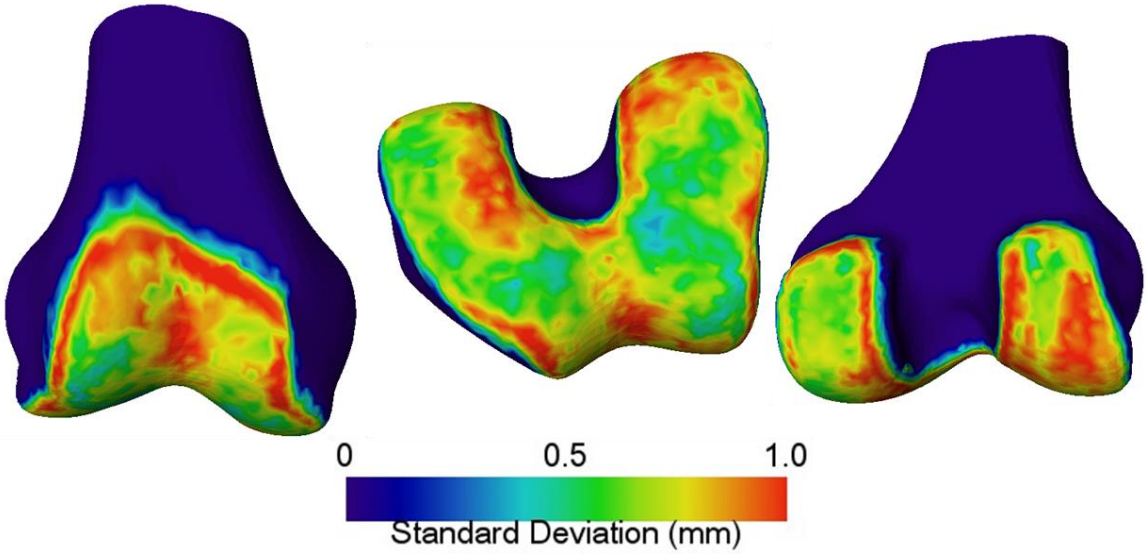


Figure 47. Standard deviation of femoral cartilage thickness in knees with valgus defects.

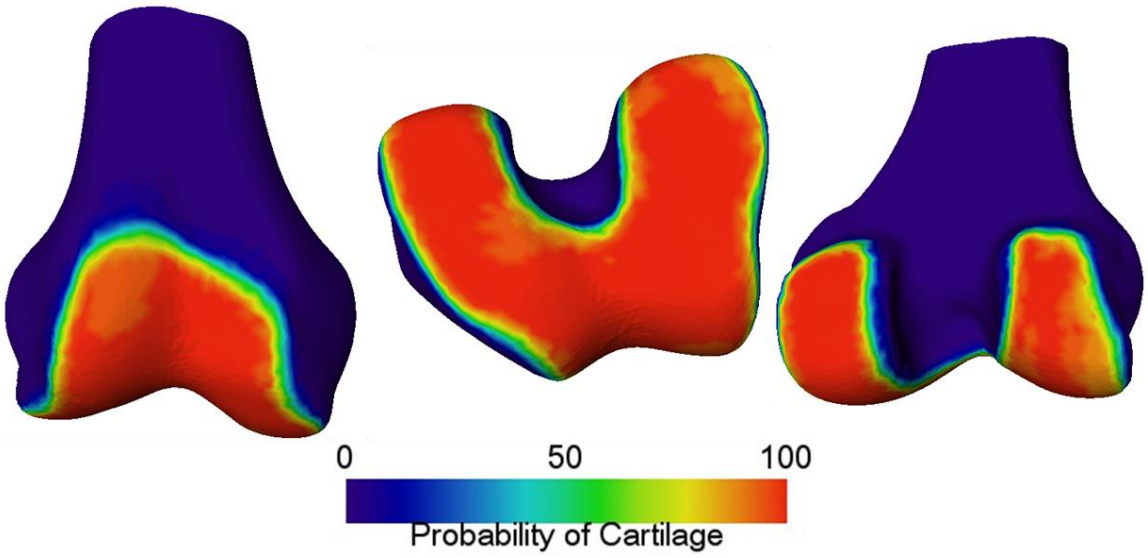


Figure 48. Probability of femoral cartilage in valgus knees.

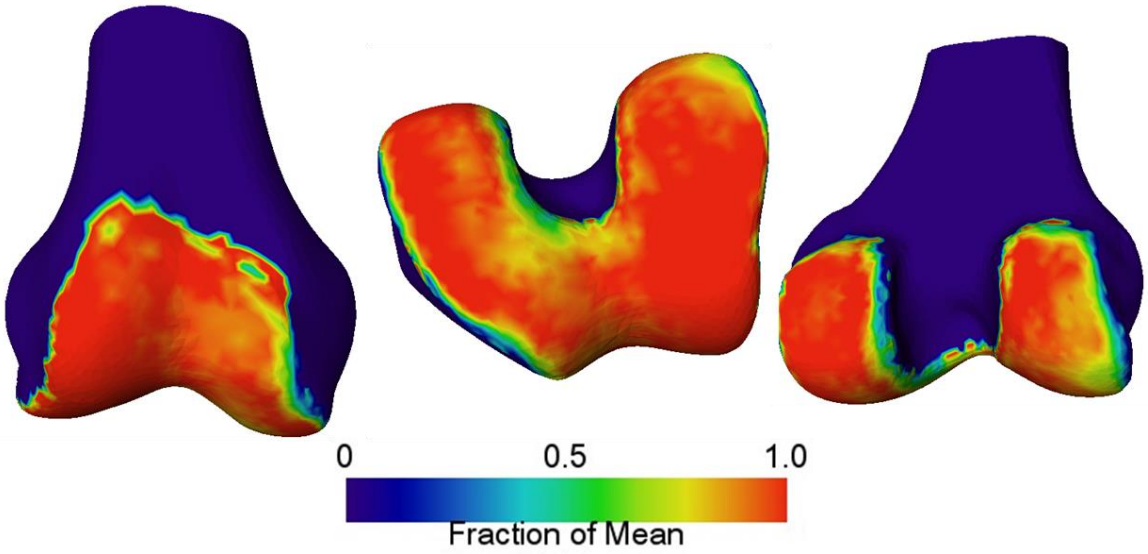


Figure 49. Normalized fraction of healthy thickness for valgus knees. Note the lateral wear is mainly in the posterior compartment of the femur.

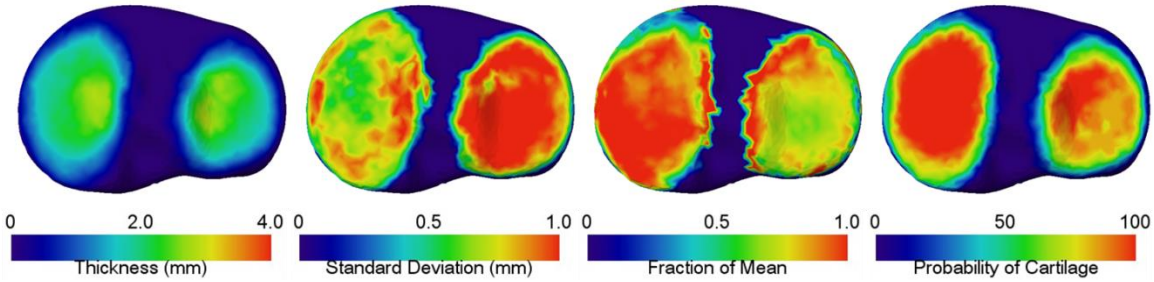


Figure 50. Cartilage for tibia in valgus knees. Note that most of the tibiofemoral wear is in the lateral tibia compartment.

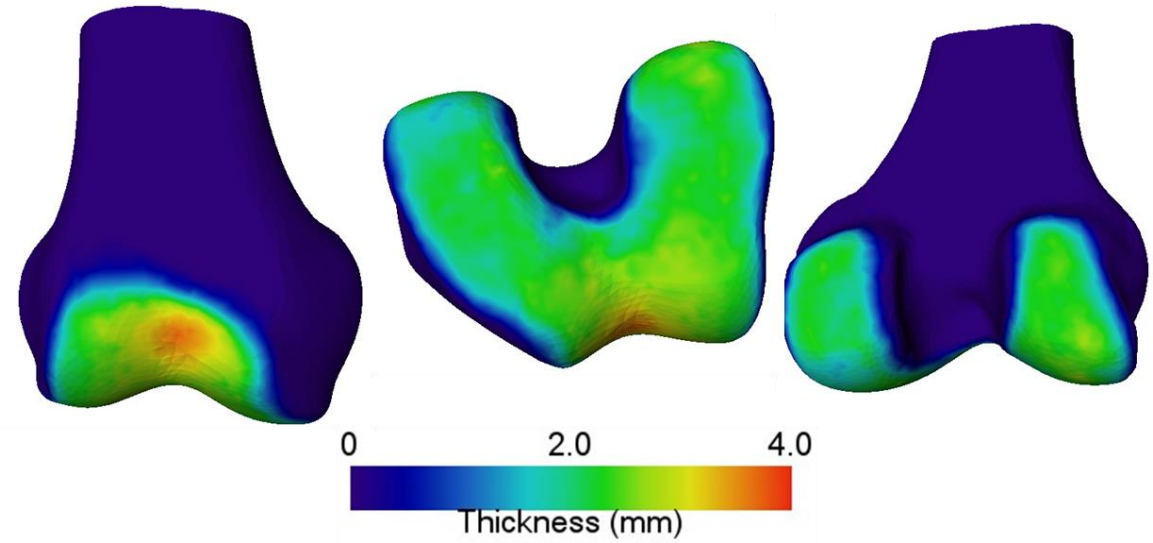


Figure 51. Mean femoral cartilage thickness in knees with defects in both compartments.

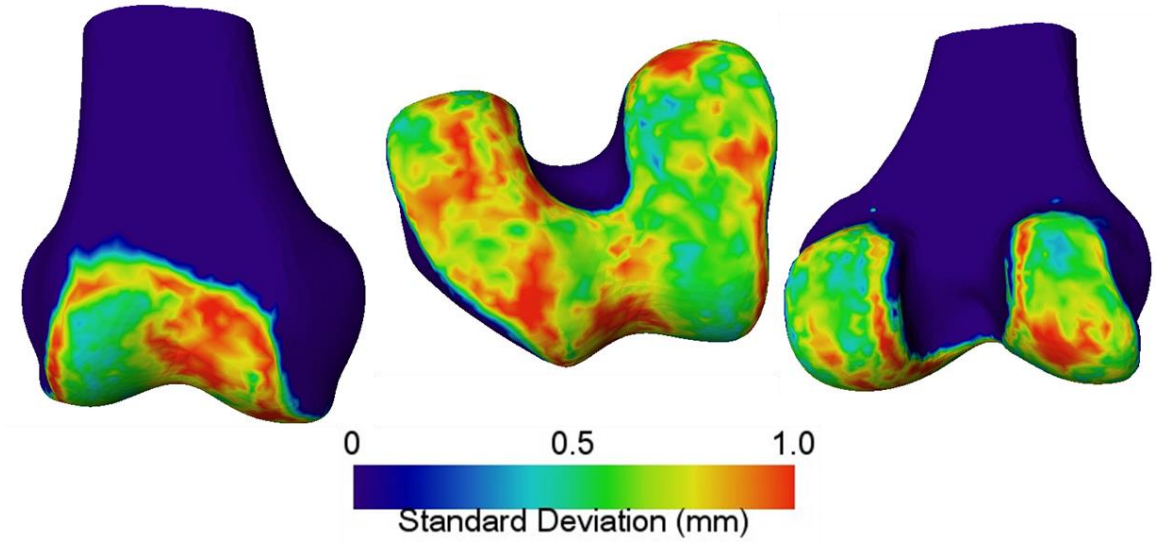


Figure 52. Standard deviation of femoral cartilage thickness in knees with defects in both medial and lateral compartments.

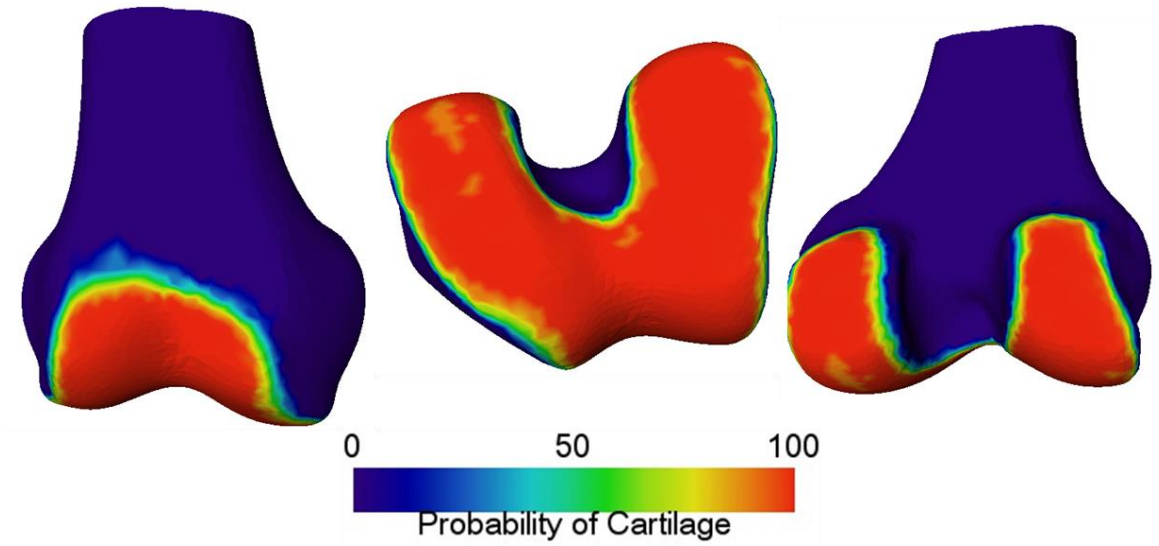


Figure 53. Probability of femoral cartilage in knees with defects in both medial and lateral compartments.

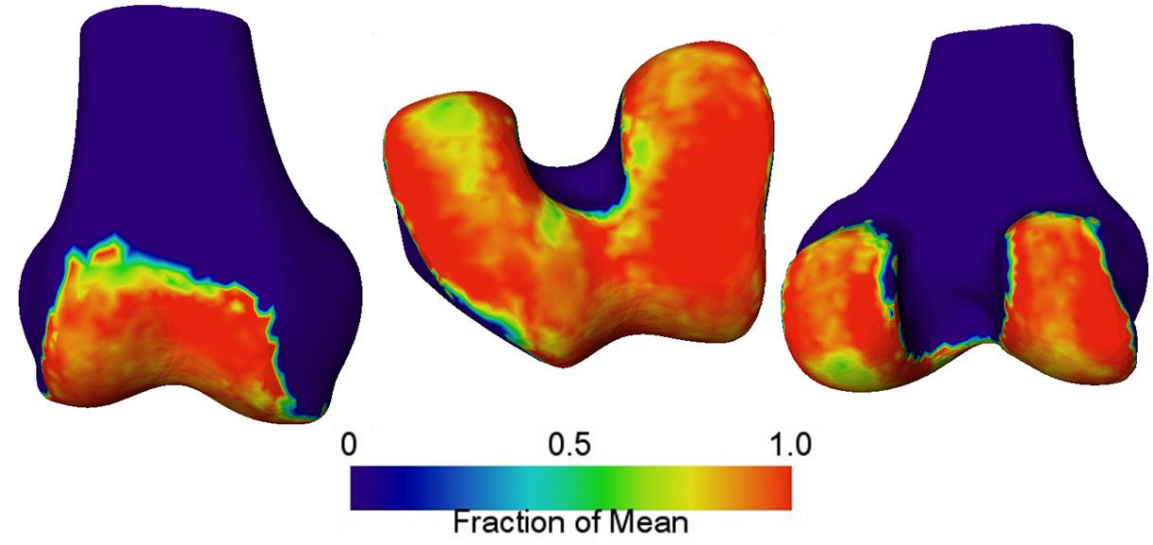


Figure 54. Normalized fraction healthy thickness in knees with defects in both compartments.

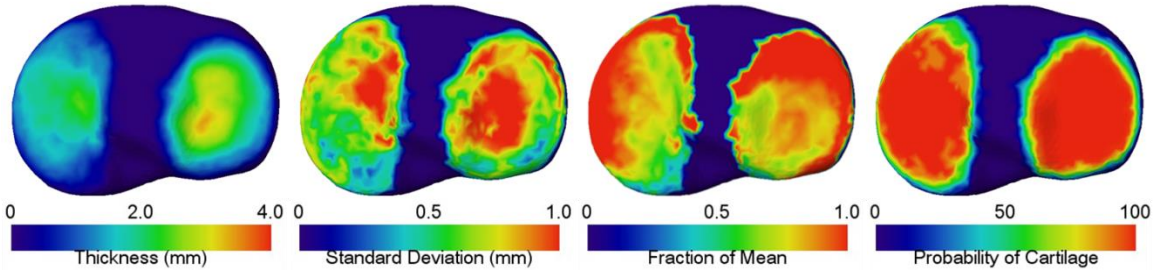


Figure 55. Cartilage for tibia with defects in both medial and lateral compartments.

Table 8. Quantitative statistics for all divisions of degenerative cartilage tissues. Of note is the inability to tell differences by examining only the mean thickness, but that the standard deviation gives some indication of degeneration.

Degenerative Type	*Anatomy*	*Mean Volume (voxels)*	*Volume std. dev. (voxels)*	*Mean thickness (mm)*	*Fraction of Healthy (%)*
KL-1	Femur	1.265E+05	3.776E+04	1.637 ± 0.882	96.7 ± 65.7
KL-2	Femur	1.315E+05	3.403E+04	1.697 ± 0.886	99.7 ± 101
KL-3	Femur	1.297E+05	3.780E+04	1.725 ± 0.964	119.7 ± 209
Neutral	Femur	1.377E+05	4.283E+04	1.724 ± 0.844	123 ± 299
Varus	Femur	1.259E+05	3.510E+04	1.609 ± 0.854	100 ± 106
Valgus	Femur	1.280E+05	3.400E+04	1.758 ± 1.033	111 ± 282
KL-1	Tibia	4.613E+04	1.396E+04	1.143 ± 0.912	93.4 ± 81.3
KL-2	Tibia	4.438E+04	1.348E+04	1.173 ± 0.935	100 ± 126
KL-3	Tibia	4.404E+04	1.747E+04	1.130 ± 0.793	128 ± 163
Neutral	Tibia	4.528E+04	1.492E+04	1.178 ± 0.854	125 ± 170
Varus	Tibia	4.688E+04	1.472E+04	1.175 ± 0.920	104 ± 88.3
Valgus	Tibia	4.251E+04	1.538E+04	1.067 ± 0.856	93.9 ± 123

4.4 Kinematic Evaluation of Pathological Wear

To evaluate kinematic contributions to pathology (or vice versa), the contact maps at various flexion angles were generated on the tibia SSM. Four subjects underwent a fluoroscopy procedure during a deep knee bend activity. Patient-specific, 3D models were segmented from CT scans each of the subjects. Each model was registered to the fluoroscopic frames using a previously described 3D-to-2D registration method [88] at the flexion angles of 0°, 20°, 40°, 60°, 80°, 100°, and 120°. For each angle, the contact map was identified on the tibia after conversion of the patient-specific tibia model to SSM correspondence. Additionally, cartilage was estimated using the method described in Chapter 6 for the 0° pose. The contact map was identified using the closest 10% of all points on each condyle of the femur and projecting onto the tibia SSM. Figure 56 shows the division of the femoral atlas into medial and lateral compartments.

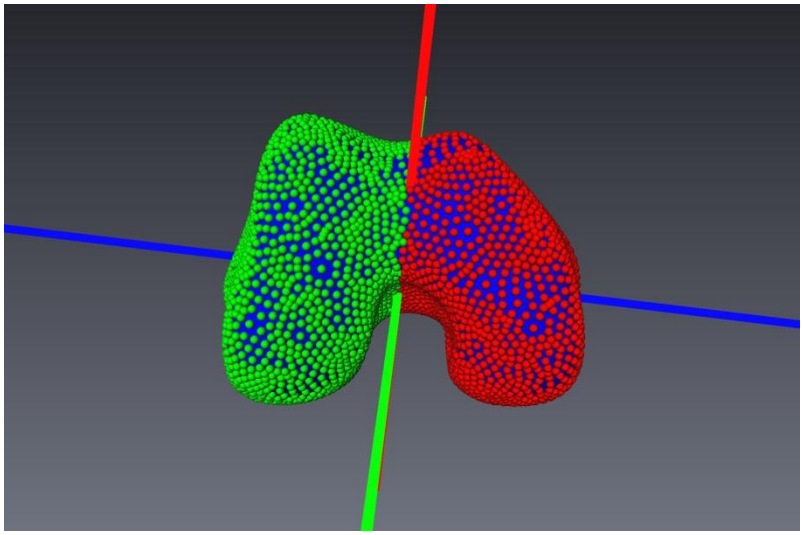


Figure 56. Division of the medial and lateral condylar vertices on the mean femoral atlas model. The division plane was taken as the mean model point with normal direction along the principal axis pointing in the most ML direction.

Regularization of the contact region was performed for each region by calculating the probability of each atlas landmark as belonging to the contact region, and finding the probability weighted mean vertex on the mean tibia for each region. This was done using the following equation:

$$\boldsymbol{v_\mu} = \frac{\sum_i P_C^i * \boldsymbol{v_i}}{\sum_i P_C^i} \qquad (7)$$

Where P_C^i is the probability that vertex $\boldsymbol{v_i}$ belongs to the contact region. The overall contact region was then estimated as the two ring neighboring set (union of neighbors of the neighbors of $\boldsymbol{v_\mu}$). Contact regions for all angles of flexion are seen in Figure 57.

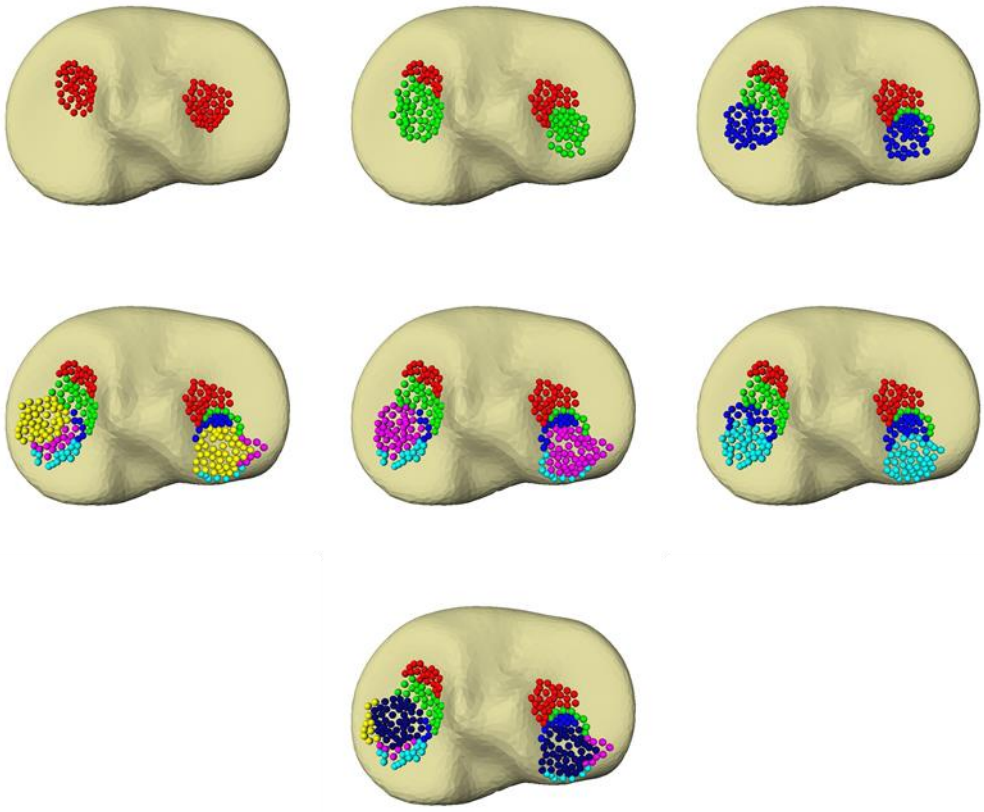


Figure 57. All contact regions starting at 0° flexion on the top left and continuing in 20° increments in a serpentine fashion to the right. Each new color represents current contact region overlaid on previous regions.

At each vertex in each contact region for medial and lateral compartments, the mean fraction of healthy thickness for each degenerative category (varus, valgus and neutral) was determined. The following plots show statistics for each flexion angle in each compartment and for each degenerative category.

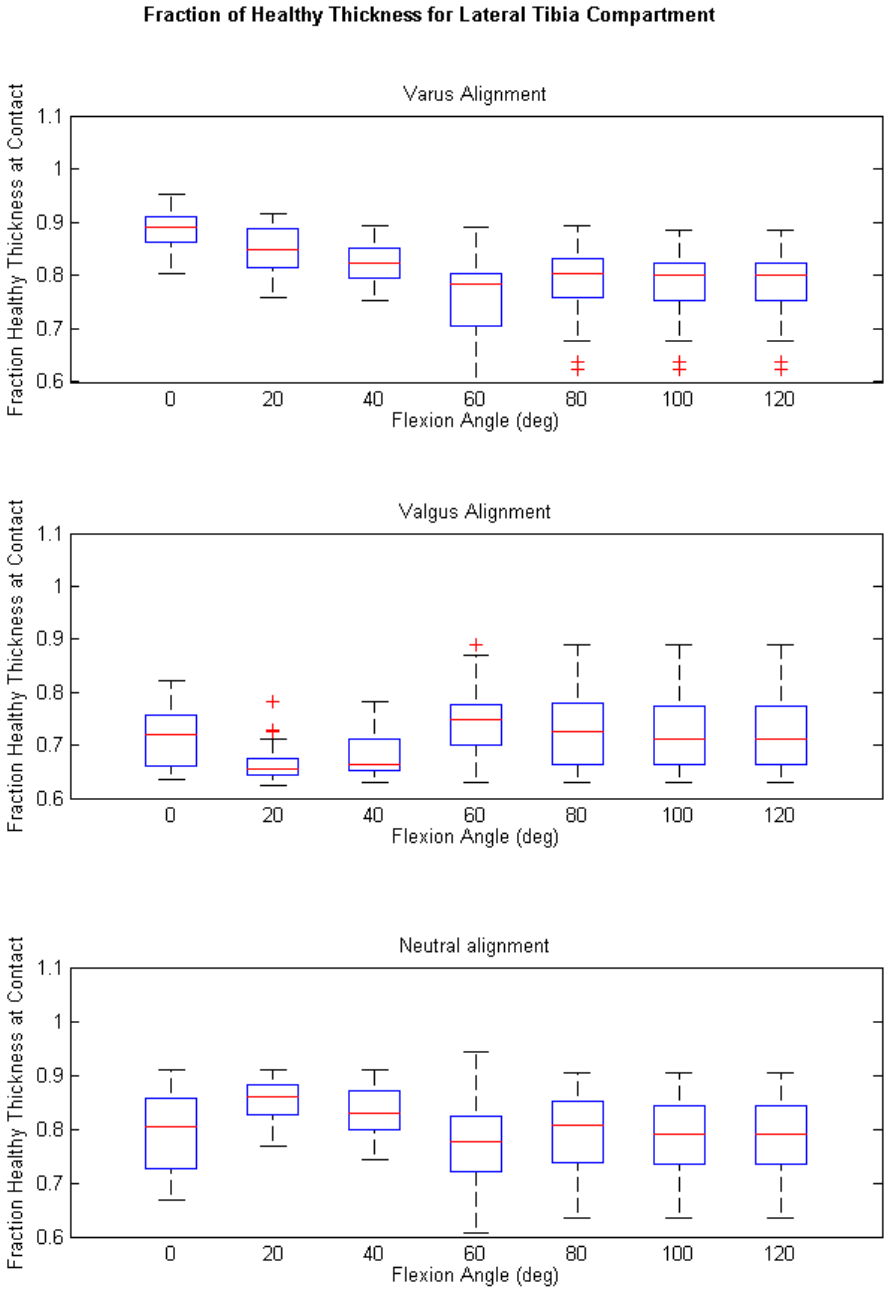


Figure 58. Fraction of healthy thickness for contact regions at each flexion angle in the lateral tibia compartment. Each subplot represents a different category of knee alignment. Notice that in the varus and neutral knees, degeneration is present in the lateral compartment, but to a lesser extent than for valgus knees.

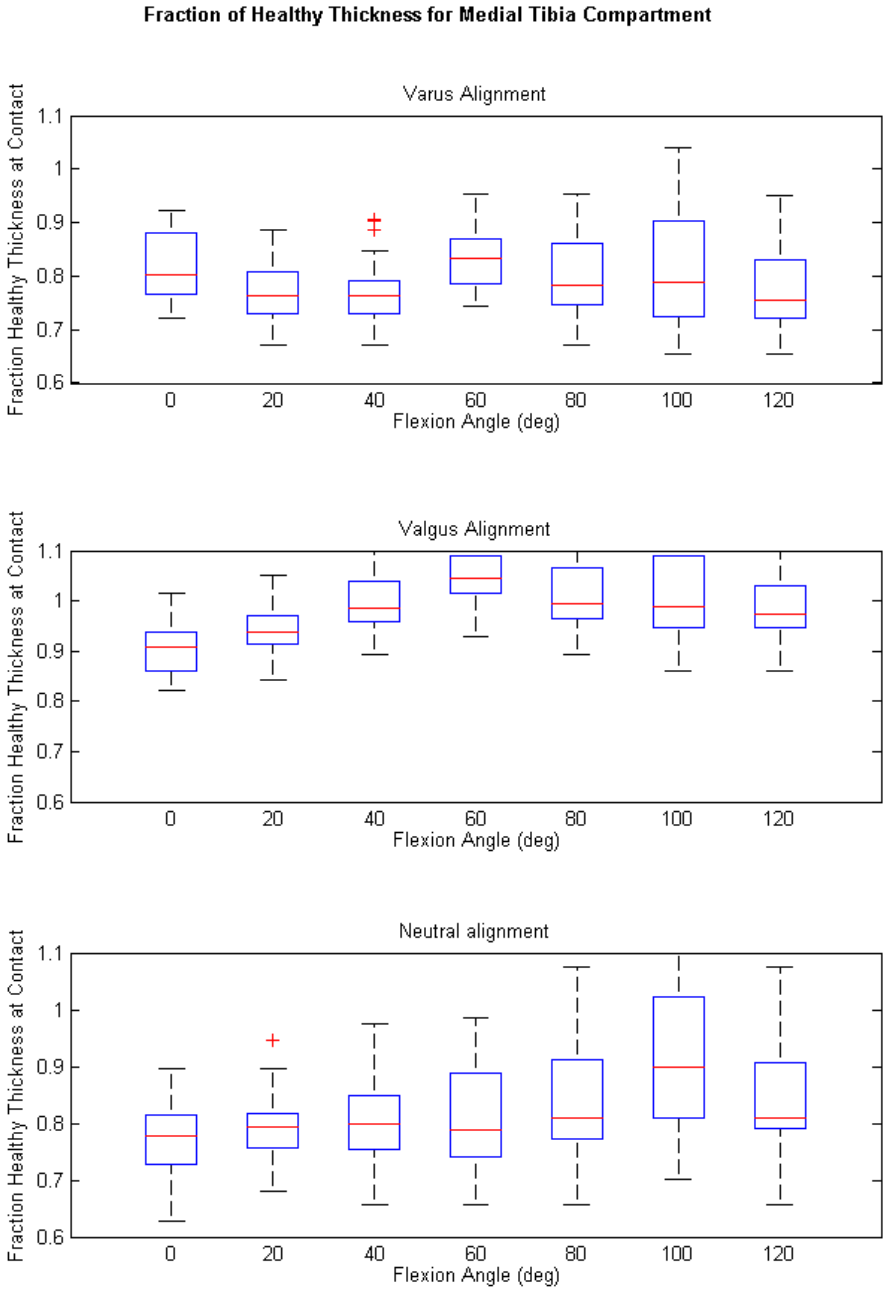


Figure 59. Fraction of healthy thickness for contact regions at each flexion angle in the medial tibia compartment. Each subplot represents a different category of knee alignment. Notice that in the valgus knee, there is little to no wear in the medial compartment, possibly suggesting that the lateral compartment is experiencing the vast majority of the loading.

4.4 Conclusions

This chapter has proposed a novel method for the examination of cartilage morphology with both high precision and resolution. Using this method, accurate maps of healthy and pathological cartilage maps were generated, illustrating the difference between gender and wear patterns. The results for varus and valgus knees corresponded with conclusions presented by the paper by Eckstein, et al. [82], which concluded that in valgus knees, cartilage wear tends to be focused on extreme (inner and outer) compartments of the femur, and even more so on the lateral tibia. This is in contrast with varus knees, where the medial femoral compartment experiences approximately the same level of wear as the medial tibial compartment.

Moreover, association of the cartilage wear region with early kinematic data may shed some light as to which activities patients with early onset OA should avoid and which activities tend to cause damage in varus/valgus malaligned knees. In a world with growing orthopedic related costs, this can provide valuable insight into OA treatment. Clearly, in valgus cases, the vast majority of loading occurs on the lateral compartments, and nearly no degeneration is present in the medial tibia compartment. Additionally, the association of wear with flexion angle suggests the majority of wear occurs between 20° and 60° flexion. This work is the first of which the author is aware that relates flexion angles with cartilage wear patterns in different cases of knee malalignment, and results suggest that much can be learned from a larger study. To improve accuracy, subjects should undergo MRI, so that patient-specific cartilage pads can be accurately segmented, instead of estimated as conducted in this work. The inclusion of the femur in the next

phase of the study may reveal more about cartilage wear as it relates to subject kinematics.

Chapter 5

Local Supervised Learning for Cartilage Segmentation

This chapter describes a novel tissue classification method that uses the point correspondence property of SSMs to anchor individual classifiers that can be used to account for local changes in tissue properties. In other words, the point correspondence characteristic of the SSM allows definition of a classifier for each vertex on the BCI, permitting a local tissue classifier to be defined with high resolution at each vertex. When combined, this surface classification scheme can be used to accurately model local changes in tissue properties which can negatively affect global classification methods. The assumption here is that pathological and morphological changes are not randomly distributed, and indeed existing literature suggests cartilage thickness is distributed to provide adequate support in regions which experience the most stress in normal activities [6]. Additionally, distinct lesion development patterns have been reported [89]. While these patterns would be very difficult to model globally, locally supervised learning methods may capture the pathological changes due to OA in an implicit way. The method for defining the classifiers is below with application to cartilage tissue segmentation.

5.1 Classifiers and Point Correspondence

The overall classification system requires that a classifier be defined at each vertex of the anchoring surface, whether it is simple (Naïve Bayes) or complex (support vector machine). In this work, the anchoring surface is a bone segmented as in Chapter 3, which

has retained point correspondence with the atlas. Thus, each vertex v_i defining the anchoring surface has associated with it a soft (or hard, if no probability is desired) classifier, $\boldsymbol{C_i^k}$. The dataset features and targets must now be defined.

For each vertex, $\boldsymbol{v_i}$, on the surface, we define a direction normal to that surface. Along this direction, a profile, $\boldsymbol{P_i}$, is defined. $\boldsymbol{P_i}$ consists of n points with each point having an associated feature vector, $\boldsymbol{x_j^i}$, where $j \in [0, n]$. Each feature vector, $\boldsymbol{x_j^i}$ is used as an input for classifier $\boldsymbol{C_i^k}$ and is given a target value, $\boldsymbol{t_j}^{\boldsymbol{i}}$. For cartilage classification this target value is given value "1" if the location of $\boldsymbol{x_j^i}$ corresponds to a cartilage sample and value "0" if not. To regularize the classifier, vertices belonging to the neighborhood, $\boldsymbol{N_i^k}$, are classified by the central vertex and all vertices, $v \in \boldsymbol{N_i^k}$. The parameter k controls the size of the neighborhood, where $\boldsymbol{N_i^0}$ contains all vertices directly connected to v_i. $\boldsymbol{N_i^1}$ contains all vertices touching every vertex in $\boldsymbol{N_i^0}$, with the exception of the original vertex, v_i, and so on for increasing k. Thus, larger k corresponds to more global classification. Figure 60 shows the size of various neighborhoods.

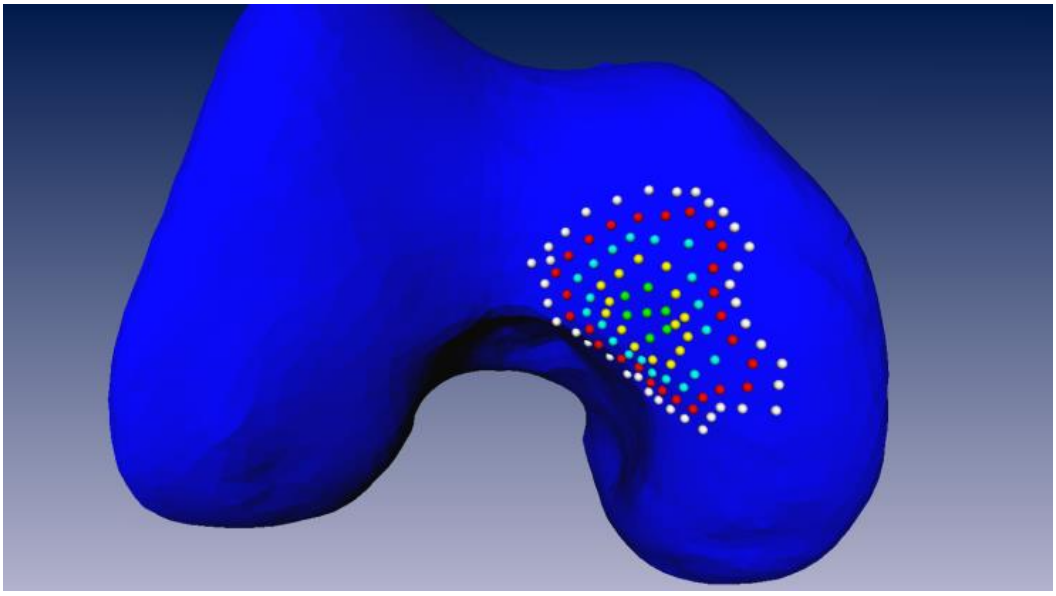


Figure 60.Various neighborhoods of a vertex. The central vertex of the green neighborhood is the origin vertex, $\boldsymbol{v_i}$*. Green vertices correspond to* N_i^0*,yellow to* N_i^1*, and so on. Larger neighborhoods reduce local tissue modeling.*

5.2 Extracting Feature Vectors and Targets

One unique challenge in defining classifiers at each vertex is of extracting the feature vectors and targets for each profile $\boldsymbol{P_i}$. As stated before, the direction of the profile is along the direction normal to the surface, passing through the vertex $\boldsymbol{v_i}$. Each profile is then sampled, this work uses every 0.1 mm, or approximately 1/3 of the shortest voxel dimension. Here, we sample the profile uniformly, at 0.1 mm, extending out from the anchoring bone until 101 samples are obtained. This guarantees we exceed the maximum cartilage thickness of the databases (~8 mm).

To extract accurate profiles and cartilage labels, the dataset was prepared by semi-automatically segmenting bone surface models using the technique described in Chapter

3. The cartilage was then added to each bone manually and the resulting binary label was subtracted from the bone binary label, leaving only the cartilage label.

5.2.1 Defining the Bone-Cartilage-Interface and Cartilage Labels

The BCI consists of the vertices with correspondence to the statistical atlas that have at least one instance of cartilage in their associated normal profiles, $\boldsymbol{P}$. For each case in the dataset, the set of BCI points is found by intersection of the profile points with the cartilage binary label. If a profile contains any profile points inside the label (inside of a voxel labeled as cartilage), then the associated vertex is added to the BCI set, the union of all individual BCI sets. The cartilage thickness at each vertex can simply be defined as the distance from the originating vertex to the farthest point labeled as cartilage on the profile. This definition allows a general way of modeling thickness and likelihood of cartilage (or any other tissue) above a reference surface.

5.2.2 Extracting Features

For a given profile belonging to the BCI, feature vectors are extracted at each sample point. The feature vector is extracted from patient pose and image information simultaneously. Each feature vector consists of a combination of image and surface information. For this work, 11 total features were used. These are:

- Image intensity (linearly interpolated)
- First order difference along *x-axis*
- First order difference along *y-axis*

- First order difference along *z-axis*
- Second order difference along *x-axis*
- Second order difference along *y-axis*
- Second order difference along *z-axis*
- Distance from origination surface
- Distance to adjacent surface
- First order difference along the profile
- Edge labeled value

For this work, the edge-labeled value defines the "region" that the current sample is in along the profile. Each region is identified by detected edges, taken as inflection points in the first order profile. For example, between the beginning of the profile and the first detected edge, all points are given edge label 0, between first detected edge and second are given edge label 1 and so on. The idea being that cartilage has a layered structure, which can begin to deteriorate in OA patients, so that in healthy patients the boundary may reside at the end of region 0 or 1; however, in degenerative patients, the boundary label can be higher. This value varies across the anatomy, making relying on a global edge detection method unreliable. The philosophy is illustrated in Figure 61.

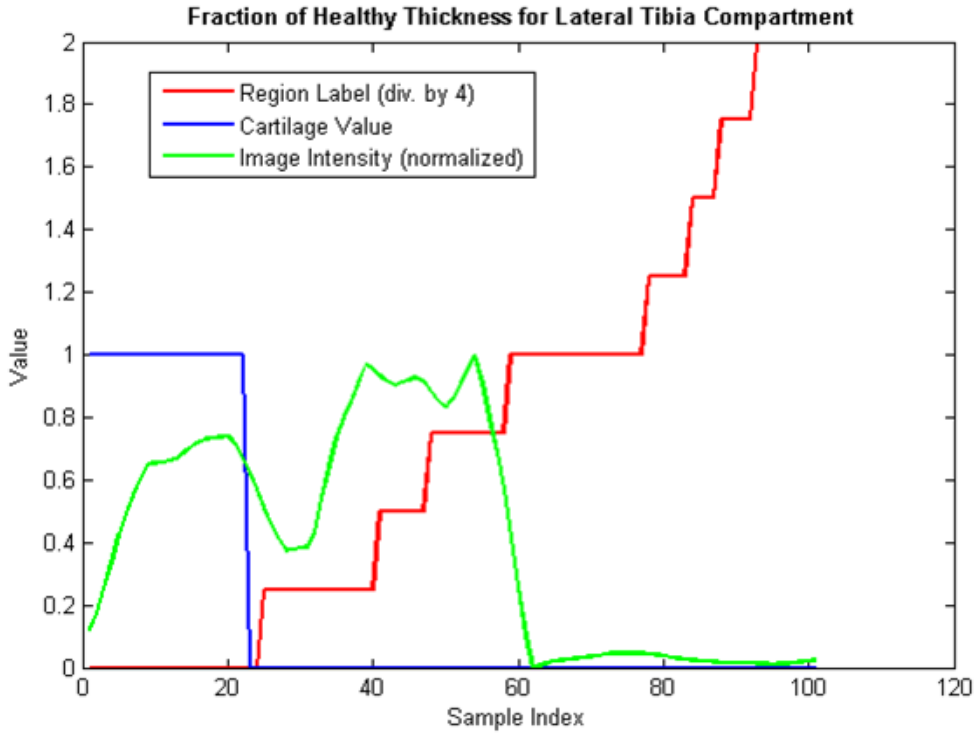


Figure 61. Edge labeled region values (red) as detected from the intensity profile along the normal direction (green). Cartilage label is shown in blue for reference. In this example, edge region 0 corresponds to the cartilage tissue.

Preprocessing steps for feature extraction include image diffusion for denoising [90] and Savitzky-Golay filtering [79] to smooth first order difference along the profile direction. All features were normalized to zero mean and unit variance.

5.2.3 Choice of Classifier

For this work, a soft classification system was desired so that the results could be analyzed from a probabilistic perspective, as well as a hard classifier perspective. It should be noted that many classifiers were tested, including support vector machine [91] (many types) and relevance vector machine [92], but none were found to be as effective as a simple, or efficient, Naïve Bayesian classification scheme. This is consistent with

existing literature, as the Naïve Bayesian classifier is often found to be as good as or better than state-of-the-art classification schemes in real world applications [93-95].

5.2.4 Classification of Points along a Profile

For vertex, v_i, we seek to classify each point in the associated 1D profile, $\boldsymbol{P_i}$ as "1" for cartilage or "0" for other tissue. To include the neighborhood information in the classification scheme, each feature point in $\boldsymbol{P_i}$, is classified using all classifiers in the neighborhood $\boldsymbol{N_i^k}$ for a total of $\left|\boldsymbol{N_i^k}\right|$ posterior probabilities, where $\left|\boldsymbol{N_i^k}\right|$ is the number of vertices in $\boldsymbol{N_i^k}$. Because each vertex in $\boldsymbol{N_i^k}$has a unique Euclidean distance to the central vertex, v_i, the posterior probabilities are weighted by the inverse distance to the central vertex. Intuitively this is equivalent to saying that the ability of a classifier to predict cartilage tissue likelihood decreases with the distance to the location being classified. For this work results were examined using majority voting for each point, inverse distance weighted voting, mean posterior probability, inverse distance weighted mean posterior probability, and a single surface classifier (not including neighboring classifiers). Using a soft classifier, the edge with the highest probability was taken as the cartilage boundary.

5.2.5 Regularization by SSM

Finally, to utilize the prior information present in the atlas for regularizing the classification output, the result of the majority voting method was projected onto a cartilage thickness SSM using a leave-one-out approach with the input data. This SSM was then used to project the classification output of the majority voting method onto the atlas space.

5.3 Segmentation Results

5.3.1 Datasets of Healthy Knees

The dataset of normal knees consisted of 40 Caucasian males and 40 Caucasian females from the OAI public dataset healthy control cohort. Supervised classification was performed using the leave-one-out method for femur and tibia separately. The datasets were separated by gender.

5.3.2 Datasets of Osteoarthritic Knees

For OA classification, the baseline data was divided two distinct ways to analyze impact on classification accuracy. First, the data was divided by KL grading, and classification was performed. Independently, the same data set was divided by deformity location (medial, lateral or bilateral), and classifiers were built for each deformity region. The data consisted of the same data as in Chapter 4.

5.3.3 Error analysis

Classifier accuracy, surface distance error, DSC [96] are reported. The DSC between two volumes was calculated as:

$$DSC = \frac{2 * V_1 \cap V_2}{(V_1 + V_2)} \qquad (8)$$

Where the intersection represents the number of overlapping voxels and the sum represents the sum of the number of total voxels belonging to each volume.

5.3.4 Healthy Results

Sample segmentations for femur and tibia are shown in **Error! Reference source not found.** and Figure 63. Table 9 and Table 10 list results for all healthy segmentation methods.

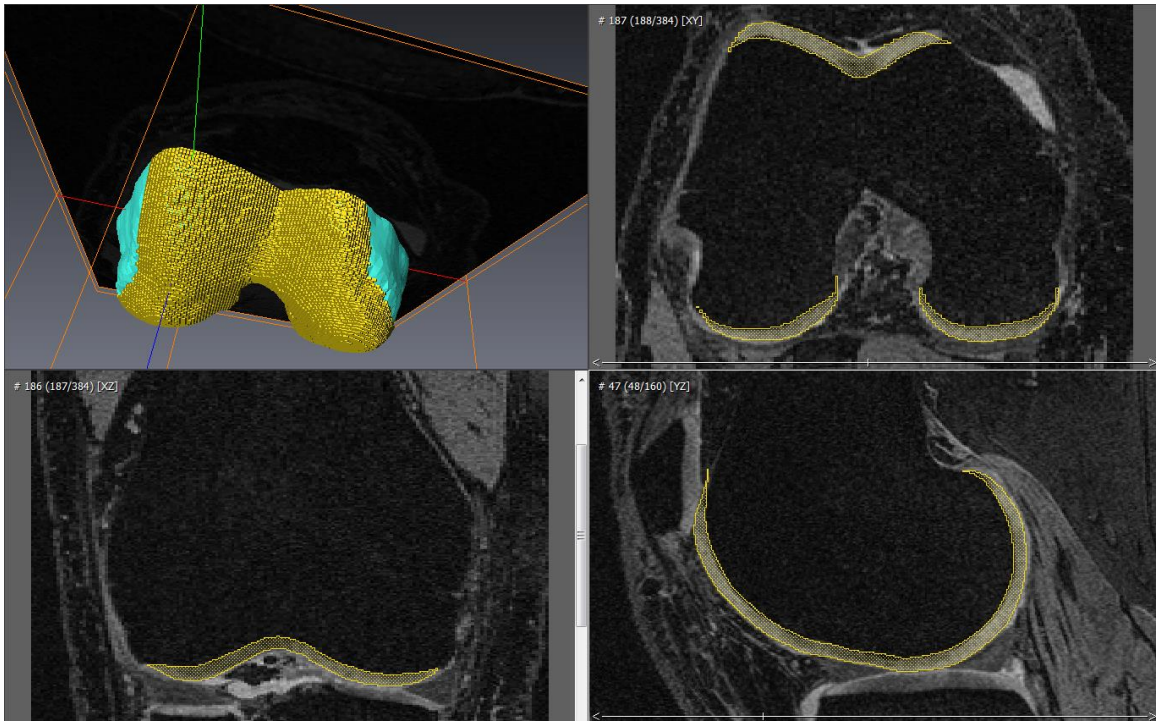


Figure 62. Sample segmentation for a healthy femoral case.

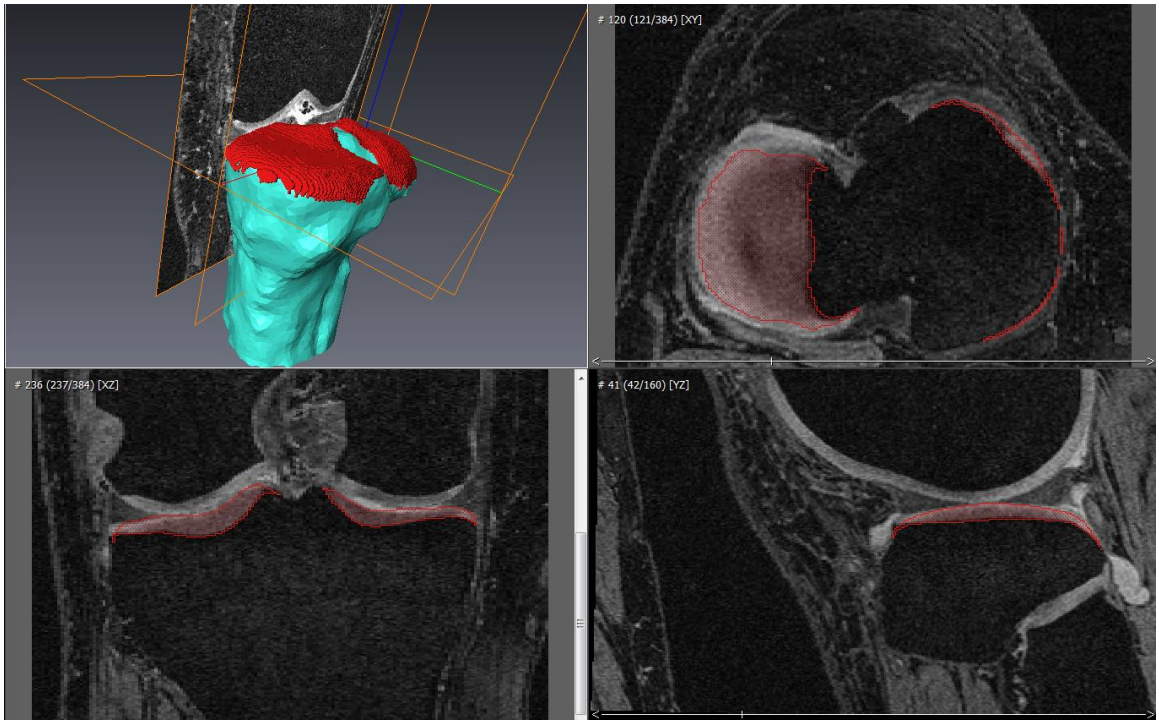


Figure 63. Example segmentation of tibia cartilage.

Table 9. Segmentation results for femoral cartilage of healthy male and female subjects.

		Inv. Distance Prob.	***Inv. Distance Voting***	***Majority Voting***	***Mean Probability***	***Atlas Projection***	***Single Classifier***
Healthy Male	Signed Error (mm)	0.010	-0.106	-0.056	0.061	-0.165	-0.211
	RMSE (mm)	0.585	0.501	0.501	0.606	0.412	0.472
	Std. Dev. Error (mm)	0.816	0.686	0.683	0.840	0.452	0.632
	Max Error (mm)	5.525	5.510	5.408	5.493	3.947	5.545
	DSC	0.862	0.878	0.878	0.856	0.885	0.879
	Volume Fraction	1.007	1.080	1.044	0.971	1.116	1.153
Healthy Female	Signed Error (mm)	-0.055	-0.120	-0.083	-0.019	-0.140	-0.202
	RMSE (mm)	0.480	0.439	0.437	0.492	0.350	0.404
	Std. Dev. Error (mm)	0.673	0.613	0.607	0.687	0.406	0.555
	Max Error (mm)	6.040	5.980	5.858	5.965	4.551	6.010
	DSC	0.866	0.874	0.875	0.861	0.887	0.877
	Volume Fraction	1.043	1.094	1.062	1.012	1.115	1.169

Table 10. Segmentation results for tibial cartilage of healthy male and female subjects.

		Inv. Distance Prob.	***Inv. Distance Voting***	***Majority Voting***	***Mean Probability***	***Atlas Projection***	***Single Classifier***
Healthy Male	**Signed Error (mm)**	-0.196	-0.219	-0.198	-0.176	-0.196	-0.231
	RMSE (mm)	0.497	0.482	0.482	0.501	0.426	0.481
	Std. Dev. Error (mm)	0.751	0.728	0.728	0.755	0.508	0.726
	Max Error (mm)	6.535	6.513	6.508	6.535	4.252	6.518
	DSC	0.848	0.850	0.851	0.847	0.856	0.849
	Volume Fraction	1.173	1.196	1.176	1.155	1.169	1.207
Healthy Female	**Signed Error (mm)**	-0.221	-0.227	-0.191	-0.192	-0.212	-0.229
	RMSE (mm)	0.384	0.382	0.377	0.378	0.370	0.383
	Std. Dev. Error (mm)	0.619	0.614	0.603	0.608	0.456	0.614
	Max Error (mm)	7.135	7.065	6.505	6.610	4.147	7.065
	DSC	0.848	0.847	0.851	0.852	0.844	0.846
	Volume Fraction	1.238	1.247	1.209	1.208	1.223	1.249

For all healthy femurs, the best DSC was achieved using majority voting with projection onto the statistical thickness atlas. DSC achieved was 0.887 for female femur cartilage and 0.885 for male femur cartilage. Using the SSM to regularize the classification result also achieved the best overall RMS error for each gender: 0.412 ± 0.452 mm for male and 0.350 ± 0.402 mm for female femoral cartilage.

For all healthy tibias, best DSC was 0.856 using SSM projection for the male tibia and 0.852 using neighborhood mean probability for the female tibia. For both male and female tibia, best RMS error was achieved using SSM projection (0.426 ± 0.502 mm and 0.370 ± 0.456 mm, respectively).

The mean segmented thickness for each gender can be seen in Figure 64,Figure 65,Figure 66, and Figure 67.

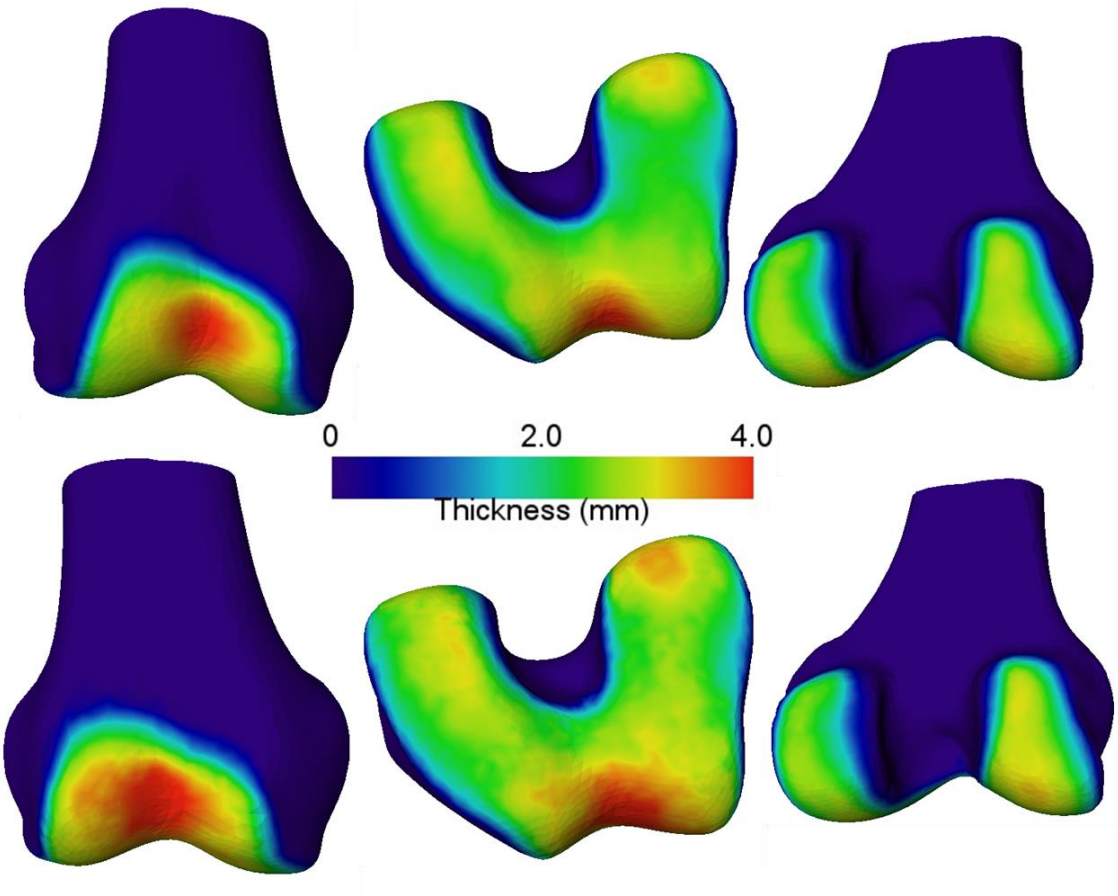


Figure 64. Comparison of true mean cartilage thickness (above) and segmented mean thickness (below) as segmented using SSM projection method for healthy male femur. The overall patterns agree closely, with some apparent oversegmentation seen as a thicker cartilage pad.

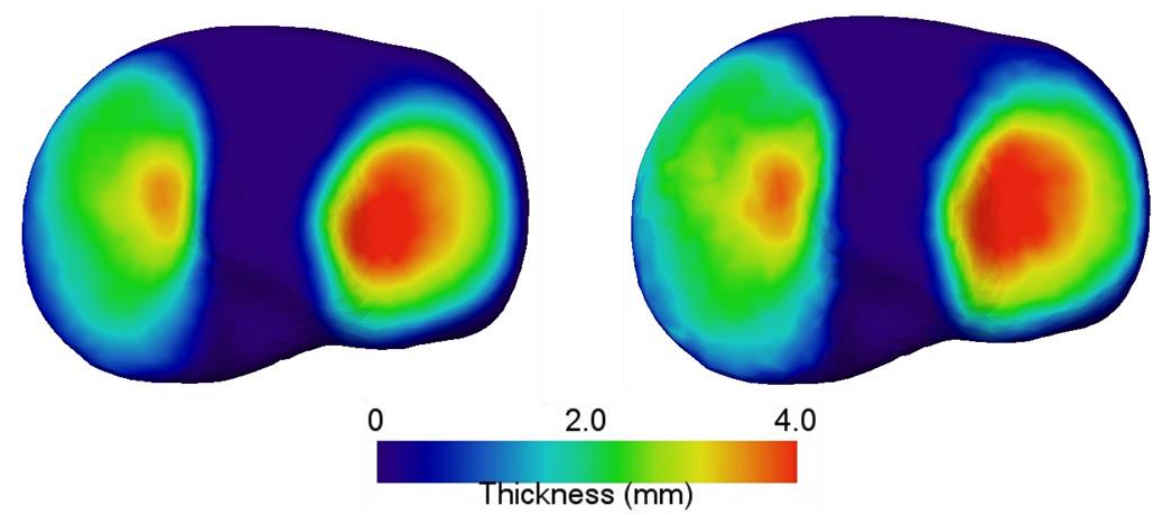


Figure 65. Mean cartilage thickness of male tibia (left) compared with the mean thickness of segmented cartilage (right) using SSM projection method.

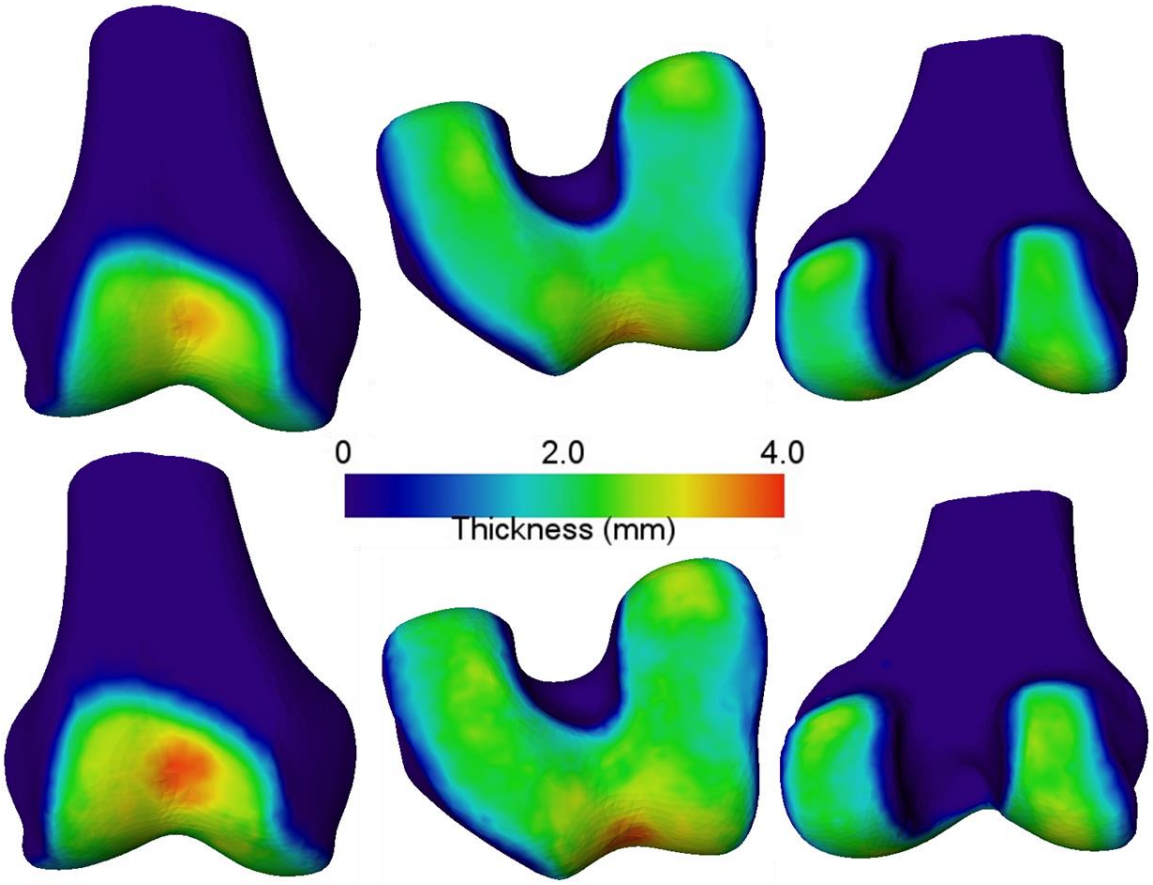


Figure 66. Mean cartilage thickness of healthy female femur (top row) compared to segmented female femur (bottom row) as segmented using the SSM method.

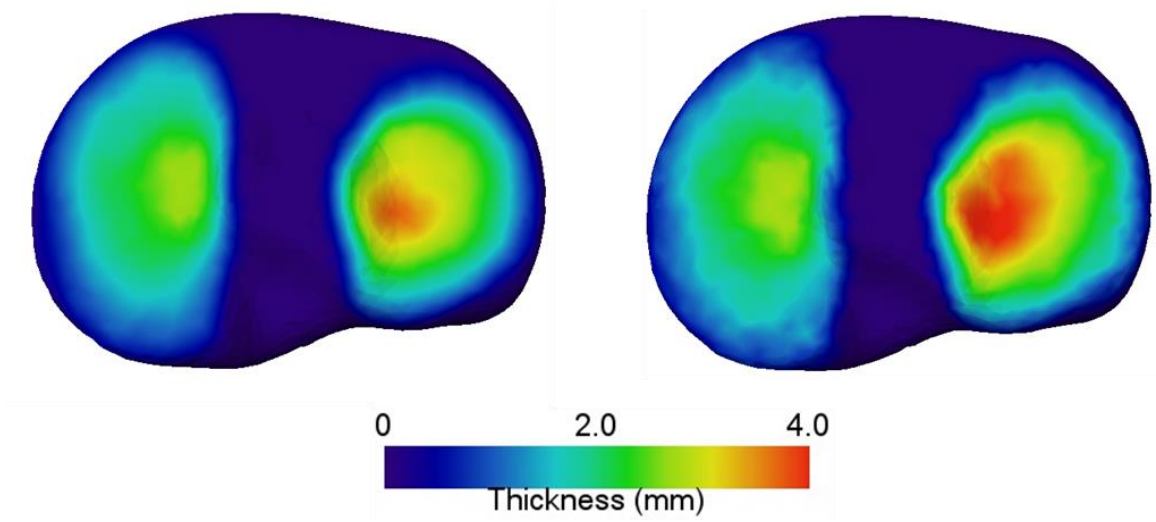


Figure 67. Mean cartilage thickness of healthy tibia (left) compared to mean segmented thickness (right) as by SSM projection method. The medial compartment appears nearly identical, but there is some oversegmentation in the lateral compartment.

5.3.5 Osteoarthritic Results

All segmented results are reported in Table 11,

Table 12, Table 13, and Table 14. As expected, best accuracy was decreased with each ascending level of degeneration for both femur (0.855 DSC for KL1 to 0.829 for KL3) and tibia (0.817 DSC for KL1 to 0.783 for KL3). Dividing the degenerative data by classification yielded mean DSC for all cases of 0.844 for the femur and 0.801 for the tibia. Dividing the degenerative data by compartment of wear yielded DSC of 0.851 for the femur and 0.806 for the tibia.

Table 11. Segmentation results for the femoral cartilage as divided by KL score.

		Inv. Distance Prob.	*Inv. Distance Voting*	*Majority Voting*	*Mean Probability*	*Atlas Projection*	*Single Classifier*
KL1	**Signed Error (mm)**	0.333	0.258	0.288	0.357	0.280	-0.177
	RMSE (mm)	0.667	0.632	0.628	0.674	0.461	0.478
	Std. Dev. Error (mm)	0.857	0.822	0.821	0.864	0.477	0.618
	Max Error (mm)	5.288	5.300	5.300	5.288	4.373	5.706
	DSC	0.783	0.804	0.799	0.776	0.824	0.855
	Volume Fraction	0.748	0.803	0.780	0.729	0.780	1.144
KL2	**Signed Error (mm)**	0.347	0.263	0.294	0.369	0.253	-0.185
	RMSE (mm)	0.717	0.681	0.674	0.721	0.480	0.521
	Std. Dev. Error (mm)	0.891	0.852	0.850	0.896	0.511	0.652
	Max Error (mm)	6.507	6.460	6.460	6.500	5.871	6.887
	DSC	0.777	0.798	0.794	0.771	0.820	0.848
	Volume Fraction	0.742	0.803	0.779	0.724	0.803	1.149
KL3	**Signed Error (mm)**	0.202	0.153	0.172	0.216	0.171	-0.112
	RMSE (mm)	0.438	0.419	0.414	0.440	0.327	0.334
	Std. Dev. Error (mm)	0.831	0.797	0.793	0.835	0.553	0.625
	Max Error (mm)	7.482	7.488	7.488	7.482	7.041	7.547
	DSC	0.761	0.781	0.777	0.754	0.784	0.829
	Volume Fraction	0.746	0.807	0.781	0.724	0.777	1.167

Table 12. Cartilage segmentation results for the degenerative tibia dataset as divided by KL score.

		Inv. Distance Prob.	*Inv. Distance Voting*	*Majority Voting*	*Mean Probability*	*Atlas Projection*	*Single Classifier*
KL1	**Signed Error (mm)**	0.168	0.094	0.131	0.184	0.088	-0.201
	RMSE (mm)	0.499	0.475	0.466	0.499	0.371	0.446
	Std. Dev. Error (mm)	0.762	0.716	0.713	0.764	0.461	0.635
	Max Error (mm)	5.381	5.244	5.250	5.388	3.887	5.500
	DSC	0.786	0.809	0.804	0.782	0.817	0.817
	Volume Fraction	0.805	0.891	0.848	0.788	0.900	1.232
KL2	**Signed Error (mm)**	0.182	0.102	0.146	0.201	0.119	-0.216
	RMSE (mm)	0.543	0.525	0.512	0.544	0.433	0.489
	Std. Dev. Error (mm)	0.800	0.766	0.758	0.804	0.515	0.648
	Max Error (mm)	5.180	5.207	5.173	5.193	3.614	5.233
	DSC	0.766	0.788	0.783	0.759	0.780	0.802
	Volume Fraction	0.804	0.892	0.844	0.782	0.872	1.239
KL3	**Signed Error (mm)**	0.164	0.080	0.126	0.181	0.107	-0.252
	RMSE (mm)	0.557	0.537	0.522	0.558	0.444	0.517
	Std. Dev. Error (mm)	0.786	0.752	0.744	0.788	0.519	0.695
	Max Error (mm)	5.188	5.218	5.194	5.141	3.986	6.388
	DSC	0.752	0.773	0.769	0.748	0.767	0.783
	Volume Fraction	0.814	0.906	0.857	0.795	0.876	1.283

Table 13. Segmentation Results for femoral cartilage using degenerative dataset divided by compartment of wear.

		Inv. Distance Prob.	*Inv. Distance Voting*	*Majority Voting*	*Mean Probability*	*Atlas Projection*	*Single Classifier*
Valgus Wear	**Signed Error (mm)**	0.189	0.139	0.157	0.203	0.160	-0.131
	RMSE (mm)	0.413	0.395	0.390	0.416	0.321	0.318
	Std. Dev. Error (mm)	0.820	0.787	0.781	0.826	0.532	0.630
	Max Error (mm)	6.250	6.217	6.217	6.250	5.342	6.611
	DSC	0.771	0.791	0.788	0.764	0.784	0.833
	Volume Fraction	0.754	0.818	0.794	0.735	0.785	1.190
Varus Wear	**Signed Error (mm)**	0.313	0.238	0.266	0.334	0.263	-0.187
	RMSE (mm)	0.654	0.623	0.616	0.660	0.430	0.461
	Std. Dev. Error (mm)	0.849	0.815	0.811	0.856	0.474	0.601
	Max Error (mm)	6.765	6.765	6.755	6.760	6.117	6.875
	DSC	0.790	0.811	0.805	0.783	0.833	0.859
	Volume Fraction	0.757	0.814	0.790	0.738	0.791	1.155
Neutral Wear	**Signed Error (mm)**	0.392	0.309	0.345	0.418	0.278	-0.151
	RMSE (mm)	0.716	0.676	0.671	0.723	0.499	0.496
	Std. Dev. Error (mm)	0.903	0.867	0.866	0.908	0.539	0.645
	Max Error (mm)	7.040	7.040	7.040	7.040	6.559	7.080
	DSC	0.781	0.805	0.798	0.772	0.819	0.865
	Volume Fraction	0.717	0.776	0.747	0.695	0.792	1.127

Table 14. Cartilage segmentation results for degenerative tibia divided by compartment of wear.

		Inv. Distance Prob.	*Inv. Distance Voting*	*Majority Voting*	*Mean Probability*	*Atlas Projection*	*Single Classifier*
Valgus Wear	**Signed Error (mm)**	0.152	0.067	0.112	0.168	0.083	-0.249
	RMSE (mm)	0.549	0.525	0.515	0.550	0.440	0.514
	Std. Dev. Error (mm)	0.813	0.776	0.769	0.814	0.516	0.719
	Max Error (mm)	4.622	4.744	4.628	4.539	3.192	5.311
	DSC	0.734	0.761	0.756	0.731	0.762	0.772
	Volume Fraction	0.819	0.919	0.867	0.800	0.900	1.295
Varus Wear	**Signed Error (mm)**	0.180	0.102	0.138	0.197	0.114	-0.206
	RMSE (mm)	0.490	0.460	0.448	0.492	0.379	0.435
	Std. Dev. Error (mm)	0.774	0.723	0.716	0.777	0.487	0.647
	Max Error (mm)	5.960	5.920	5.955	5.990	4.615	6.840
	DSC	0.794	0.819	0.816	0.789	0.811	0.824
	Volume Fraction	0.805	0.892	0.853	0.786	0.874	1.236
Neutral Wear	**Signed Error (mm)**	0.253	0.181	0.220	0.272	0.134	-0.122
	RMSE (mm)	0.527	0.500	0.492	0.530	0.441	0.438
	Std. Dev. Error (mm)	0.752	0.709	0.704	0.757	0.497	0.601
	Max Error (mm)	4.840	4.990	4.940	4.810	3.555	5.210
	DSC	0.766	0.795	0.787	0.760	0.781	0.835
	Volume Fraction	0.727	0.804	0.761	0.707	0.866	1.137

5.4 Conclusions

In this chapter, a novel segmentation method was proposed using SSM as an anchor to define a high resolution map of local tissue classifiers for cartilage segmentation. A second unique contribution is the division of degenerative training data by KL classification and compartment of wear. The hypothesis that division by wear compartment may yield better results was confirmed with higher DSC being achieved using this method. The reason for this is that the local tissue classifier may encode implicit information regarding the degenerative wear pattern, including local changes in thickness and local appearance changes due to pathology. Overall results compare favorably to existing state-of-the-art, as seen in Table 15.

Table 15. Segmentation results from the proposed method compared with state-of-the-art. Best healthy result and best degenerative result are highlighted in bold.

Author	*Number of Cases*	*Mean DSC Femur*	*Mean DSC Tibia*
Shan [97]	12 Healthy, 6 Degen	0.782	0.826
Folkesson [42]	51 Healthy, 63 Degen	0.77	0.81
Fripp [38]	20 Healthy	0.848	0.826
Lee [98]	10 Degen	0.825	0.808
Yin [39]	48 healthy, 12 Degen	0.84	0.8
Wang [43]	176 Degen (88 subjects)	0.847	**0.837**
Proposed	80 Healthy	**0.886**	**0.851**
Proposed	26 Degen	**0.851**	0.806

Further improvement can likely be obtained by refining the training sets to include more cases in each degenerative group. Additionally, the simple classification method can be further refined by feature selection at each vertex, which should improve overall accuracy of the classifier. In conclusion, the proposed method has been shown to perform as well as, and in many cases, better than the current state-of-the-art.

Chapter 6

Cartilage Estimation

Often, the standard of care imaging of OA patients is limited to available modalities such as XR, or, if the case is severe and metal hardware (e.g., screws, trauma plates, etc.) are present, CT. These modalities fail to capture cartilage tissue properties, making accurate segmentation of the cartilage impossible to compute directly. Therefore, an estimation of cartilage thickness and location must be made using *a priori* information regarding a known model of the cartilage, as well as the available bone shape and pose. Many applications attempt to estimate the cartilage layer with a uniform thickness at approximate locations, or just avoid it altogether. Clearly, as seen in Figure 68, the cartilage layer is anything but uniform. This is especially true in pathological cases.

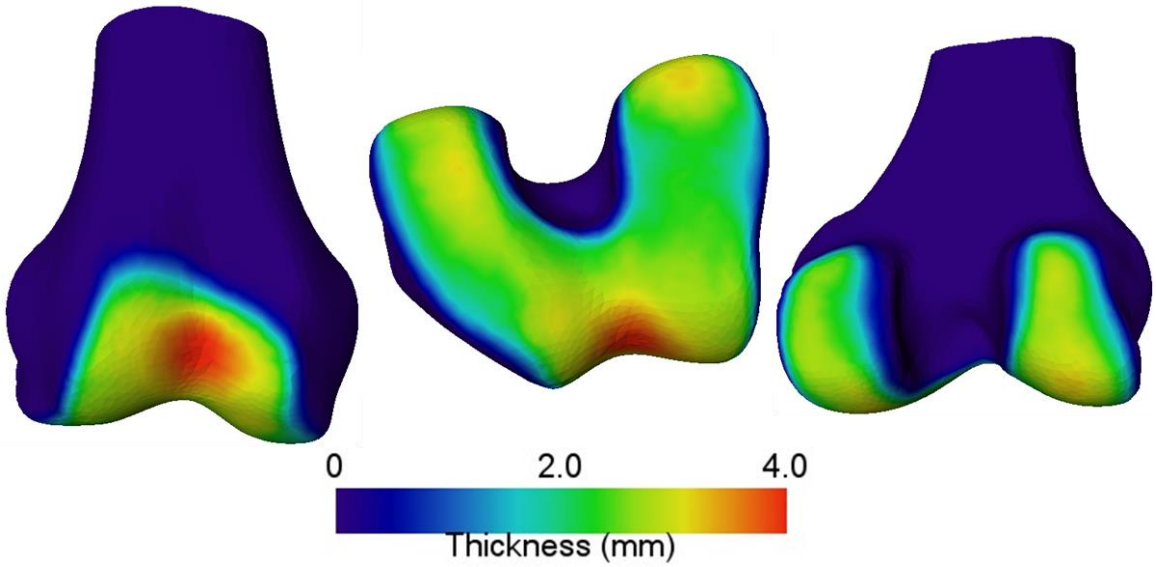


Figure 68. Caucasian male mean femur thickness. Note stark difference in cartilage thickness across the surface. Clearly, approximating the thickness as uniform will not suffice for most applications.

Additionally, any surgical landmarks which would normally be placed on the cartilage surface, such as distal and posterior femoral landmarks, will be quite different if placed on the bone surface as opposed to the appropriate position as dictated by the cartilage layer. This difference can adversely affect the accuracy of planning measurements (e.g., posterior-condylar axis or spherical axis). This work proposes a novel method for estimation of cartilage thickness by constructing SSMs of the bone (Chapter 3) and cartilage models (Chapters 4 and 5) and using pose information to produce full cartilage models. By building the thickness model with OA patient cartilage layers and dividing the data into compartmental wear patterns, the overall deformities in the cartilage can be modeled in a manner sufficient for estimation. Estimation of both healthy and pathological cartilage will be explored.

6.1 Building the *a priori* Information

The first step to building the estimation model was to build the database of *a priori* information. Here, the same dataset as described in Section 4.2 was used. Models were built for levels 1-3 on the KL scale and for healthy patients separately. The bone segmentations, described in Chapter 3, with atlas correspondence were used to anchor the cartilage model and to guarantee a level of point correspondence. Then, the thickness model was defined as a vertex and thickness pair for the union of all bone-cartilage interface points across all subjects. For OA patients, data was divided by deformity location, as this gave the best prediction results during classification.

6.1.1 Calculating the Cartilage Thickness and Location Model

The cartilage thickness and locations are as described in Chapter 4. Additionally, a cartilage atlas was built using PCA as the bone, but with thickness as the input instead of 3D models. The first PC of this atlas is linearly related to the mean thickness, or scale of the cartilage layer. Other PCs are more difficult to conceptualize, but contribute in a monotonically decreasing way to overall thickness variation of the cartilage layer.

6.2 Estimation Methods

6.2.1 Constructing the Initial Estimate

The initial estimate of the cartilage is constructed starting with the segmented bones in the imaged pose. For this work, all data was obtained from the OAI MRI database, so that

the imaged pose represents the leg in full extension while the patient is in the supine position. An example of this bone configuration is depicted in Figure 69.

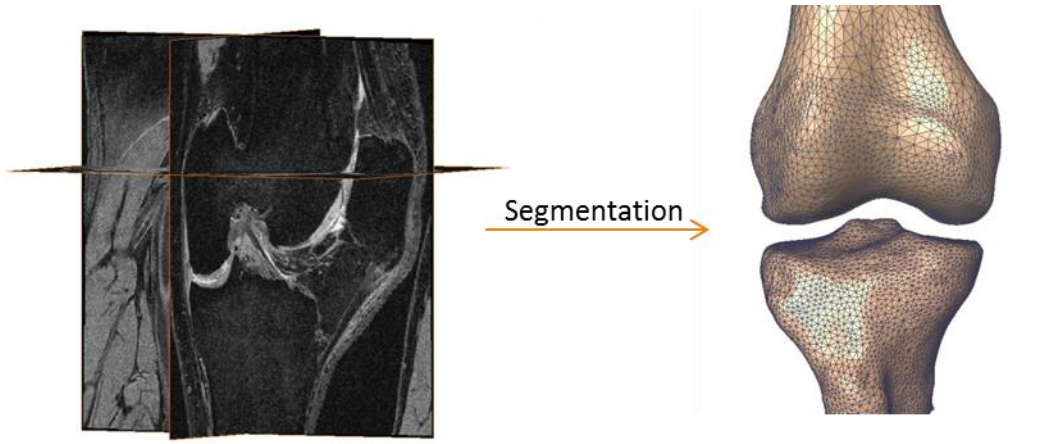


Figure 69. Segmentation of MRI image results in the SSM bone models in the appropriate pose.

The cartilage SSM was then used to approximate the patient-specific cartilage as follows:

1) For all vertices on the bone model, the model surface normal was calculated at each.
2) Using the cartilage SSM as a lookup table all vertices belonging to the BCI, V_{BCI}, were found.
3) At each vertex, $\in V_{BCI}$, the bone surface vertex was moved along the normal the distance of the mean thickness at *v* as defined by the mean cartilage model.
4) Each BCI vertex was tested on both the new cartilage femur and the tibia models for being internal to the articulating model.
5) For all internal points, thickness was reduced by some factor, *p*, where $0 < p < 1$.

6) Steps 5 and 6 were repeated until there were no internal points *or* until cartilage thickness at all internal points was very near 0.
7) Results were regularized by projection of resulting thickness onto cartilage SSMs (femur and tibia, respectively).

6.3 Results

Estimation results for all cases can be seen in Table 16. For healthy cases, the mean DSC was 0.848 for the femur and 0.800 for tibia. For degenerative cases divided by KL score, estimation DSC was 0.790 for the femur and 0.716 for the tibia. When degenerative data was divided by compartment of wear, DSC was 0.796 for the femur and 0.720 for the tibia. In general, estimation of the cartilage tended to underestimate the cartilage volume.

Table 16.Results from cartilage estimation for the femur and tibia.

		Healthy Male	***Healthy Female***	***KL1***	***KL2***	***KL3***	***Neutral***	***Varus***	***Valgus***
Femur	**Signed Error (mm)**	0.047	0.038	0.047	0.050	0.066	0.054	0.046	0.062
	RMSE (mm)	0.061	0.049	0.059	0.063	0.082	0.067	0.057	0.077
	Std. Dev. Error (mm)	0.038	0.031	0.036	0.038	0.048	0.040	0.034	0.045
	Max Error (mm)	0.240	0.197	0.220	0.212	0.258	0.243	0.208	0.253
	DSC	0.847	0.848	0.814	0.807	0.751	0.793	0.817	0.772
	Volume Fraction	0.904	0.887	0.853	0.859	0.803	0.846	0.856	0.817
Tibia	**Signed Error (mm)**	0.051	0.043	0.049	0.054	0.059	0.053	0.049	0.057
	RMSE (mm)	0.066	0.055	0.062	0.071	0.075	0.068	0.062	0.074
	Std. Dev. Error (mm)	0.042	0.034	0.038	0.045	0.046	0.042	0.039	0.047
	Max Error (mm)	0.226	0.181	0.213	0.233	0.237	0.231	0.214	0.256
	DSC	0.803	0.796	0.754	0.724	0.672	0.720	0.749	0.687
	Volume Fraction	0.883	0.862	0.831	0.813	0.738	0.796	0.810	0.779

Figure 70, Figure 71, Figure 72, and Figure 73 show the mean thickness as estimated next to the true mean thickness for the healthy dataset. The overall pattern is consistent with the gold standard thickness, though there is some apparent undersegmentation in the medial compartment of all sets.

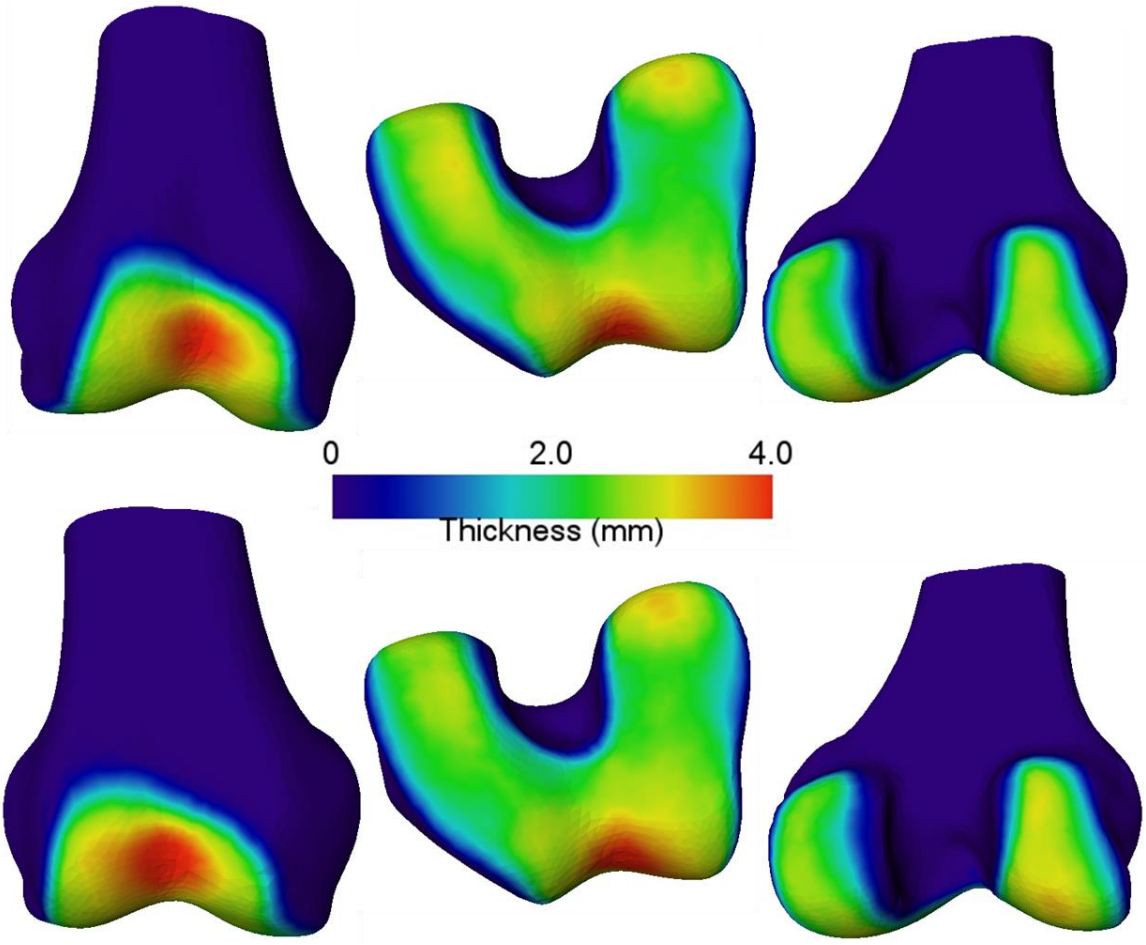


Figure 70. Mean thickness of the femoral cartilage for healthy males (top) compared with the mean estimated thickness for healthy males (bottom).

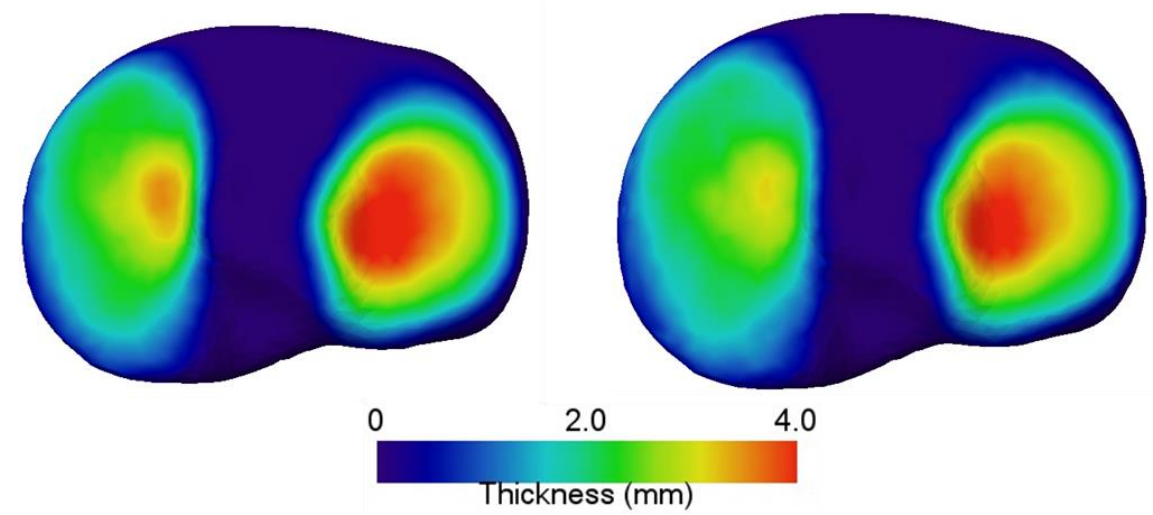


Figure 71. Mean thickness of the tibia cartilage for healthy male (left) compared to estimated mean thickness for healthy males (right).

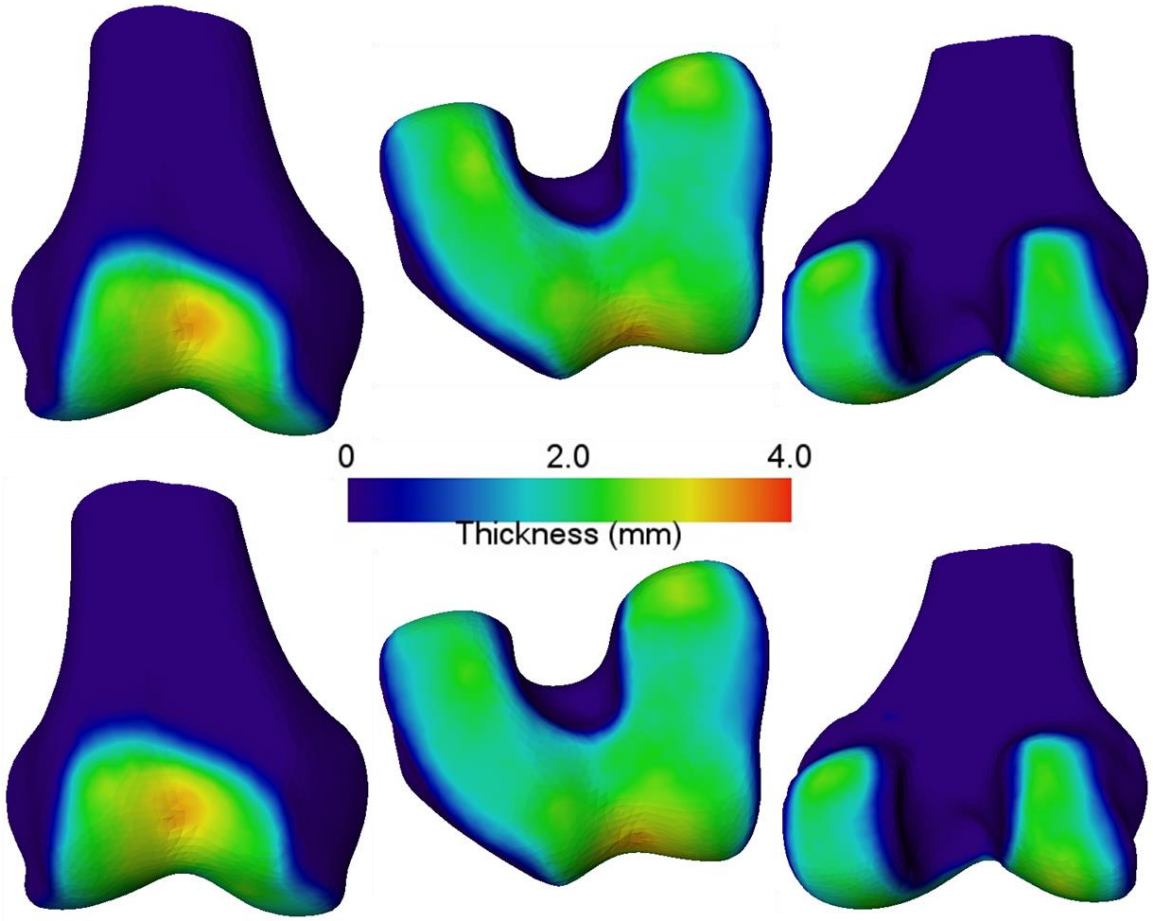


Figure 72. Mean thickness for healthy female femur (top) compared to estimated mean thickness of healthy female femur (bottom).

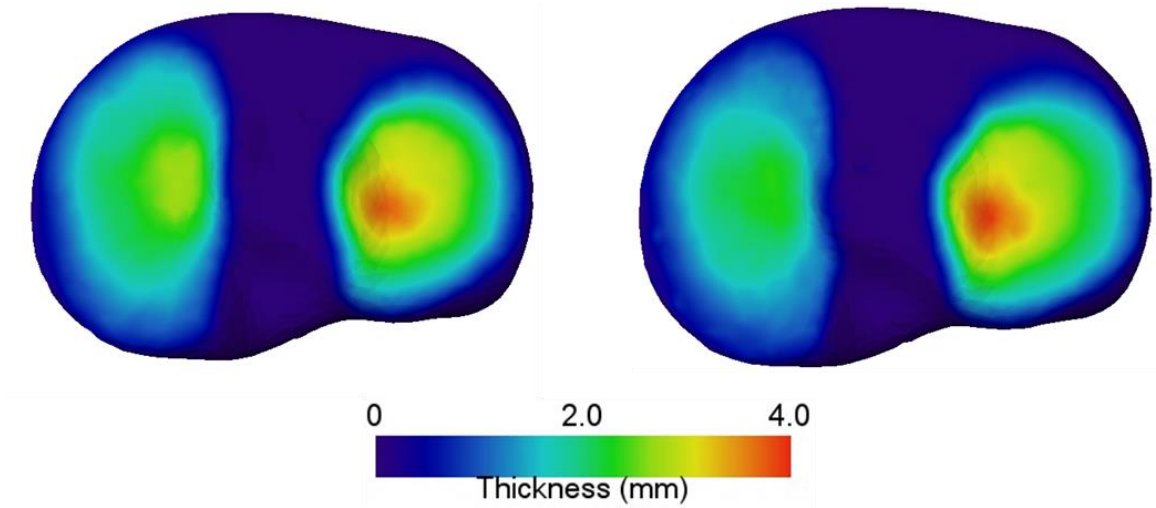


Figure 73. Mean thickness of healthy female tibia (left) compared with estimated mean thickness of healthy female tibia (right).

6.4 Conclusions

A novel method for estimation of cartilage using SSM was described, and results in healthy knees were slightly less accurate than the automated segmentation described in Chapter 5; although, these were still acceptable considering no image information was used to define the cartilage layer. This has potential applications when a subject is imaged using the more available, and less expensive, modalities of XR fluoroscopy, DXR or CT – none of which provide image information regarding the cartilage thickness, unless a contrast agent is injected prior to imaging. Research and further analysis should be conducted in the application of this method to degenerative knees, as the resulting accuracy was less than the accuracy in healthy knees – specifically, in the medial compartment.

Chapter 7

Conclusion and Recommendations

With a rapid demand for orthopedic procedures, including those involving the knee, there comes an increasing necessity in understanding the biomechanics and morphology of the associated joints. This work focused on the knee, as it undergoes significant loading during normal activities. This significant loading suggests that effective treatments, specifically those involving prostheses, of OA of the knee will be required to meet the biomechanical challenges of the joint. A full analysis of the joint should include both the hard (bone) and soft (cartilage and ligaments) of the joint. Much previous kinematic work focuses on using the bony anatomy as reference, ignoring cartilage. As seen in Chapter 4, however, the cartilage surface is not congruent to the bone surface, suggesting changes in morphology of the articulating surface of the bone which will affect biomechanics. Thus, it is important to acquire accurate cartilage thickness, even if the soft tissue is not visible in the subject images. This work sought to propose methods for effectively modeling cartilage morphology and using said models as a foundation for segmentation (if the cartilage is visible) and estimation (if no cartilage visual information is available). In doing so, the cartilage thickness need not be ignored in subsequent kinematic studies or surgical planning.

In regards to cartilage morphology, there are clear wear patterns in varus and valgus knees, suggesting perhaps that predictable biomechanical changes are to blame for malalignment. Due to the high-resolution nature of the surface and thickness, SSMs permit easy visualization of the cartilage morphology in addition to facilitating the

normalization of pathological morphology. This conflicts with previous works by Eckstein and Wirth, where the cartilage wear pattern was difficult to localize due to large divisions of the cartilage compartments. Future work should seek to increase the number of subjects for pathological analysis, while refining analysis by KL score in conjunction with pathological compartments. An interesting set of questions may be: How do varus/valgus cartilage thicknesses progress with KL score? Can these regions be related to known kinematic patterns, possibly suggesting activities to avoid if at risk of cartilage loss?

In Chapter 5, the cartilage segmentation algorithm proposed used the point correspondence of the atlas to define local classifiers at each BCI vertex on the bone. Segmentation is critical as available data increases quickly. For instance, the OAI dataset consists of roughly 4,500 subjects which undergo MRI imaging on both knees at one year follow ups. Without improvements to automatic and semi-automatic segmentation methods, it would be nearly impossible to analyze such a large dataset. The proposed method could be improved by refining the segmentation process through feature refinement and increasing the number of training subjects. Despite using such a simple classifier, through careful division of the datasets and exploitation of the point correspondence of the bone, SSM results were obtained that were as good as or better than current state-of-the-art methods. Additionally, such a method could be used to classify any difficult object in close and predictable proximity to an adjacent, more easily segmented object.

As imaging costs escalate, and a growing number of OA cases is anticipated, the method for estimating cartilage thickness proposed in Chapter 6 of this work has the potential to advance imaging options with more accuracy at decreased expense. Currently, most diagnostic imaging options consist of XR, digital fluoroscopic XR or CT – none of which capture cartilage tissue information. Conversely, the method discussed herein has been determined to be fairly accurate at estimating healthy cartilage tissue, but more work is needed to refine estimation in general and, specifically, in pathological cases. In most cases, underestimation on the medial compartment of both femoral and tibial cartilage suggests improvement can be made just by examination of this region. Future work should examine kinematic differences between estimated cartilage and true cartilage thickness, while refining the estimation process.

In summary, this work proposed methods of cartilage modeling to aid in the development of novel segmentation and estimation methods for imaging, specifically those emphasized in the application of diagnosis and treatment of OA of the knee. Using such methods as depicted here, a better picture of the cartilage surface is revealed, permitting use of cartilage thickness in applications, such as kinematic modeling and surgical planning that have been previously neglected.

List of References

1. Kuettner, K. and V. Goldberg, *Introduction.* Osteoarthritic Disorders. Rosemont, Ill: American Academy of Orthopaedic Surgeons, 1995: p. 21-5.
2. Sharma, L., et al., *Laxity in healthy and osteoarthritic knees.* Arthritis Rheum, 1999. **42**(5): p. 861-70.
3. Slemenda, C., et al., *Reduced quadriceps strength relative to body weight: a risk factor for knee osteoarthritis in women?* Arthritis & Rheumatism, 1998. **41**(11): p. 1951-1959.
4. Hart, D.J., D.V. Doyle, and T. Spector, *Incidence and risk factors for radiographic knee osteoarthritis in middle-aged women.* Arthritis Rheum, 1999. **42**(1): p. 17-24.
5. Seedhom, B., D. Dowson, and V. Wright, *Proceedings: Functions of the menisci. A preliminary study.* Annals of the rheumatic diseases, 1974. **33**(1): p. 111.
6. Li, G., et al., *The cartilage thickness distribution in the tibiofemoral joint and its correlation with cartilage-to-cartilage contact.* Clinical biomechanics, 2005. **20**(7): p. 736-744.
7. Farquhar, T., et al., *Swelling and fibronectin accumulation in articular cartilage explants after cyclical impact.* Journal of orthopaedic research, 1996. **14**(3): p. 417-423.
8. Chen, C.T., et al., *Chondrocyte necrosis and apoptosis in impact damaged articular cartilage.* Journal of Orthopaedic Research, 2001. **19**(4): p. 703-711.
9. Loening, A.M., et al., *Injurious mechanical compression of bovine articular cartilage induces chondrocyte apoptosis.* Archives of biochemistry and biophysics, 2000. **381**(2): p. 205-212.
10. Van Beuningen, H.M., et al., *Transforming growth factor-beta 1 stimulates articular chondrocyte proteoglycan synthesis and induces osteophyte formation in the murine knee joint.* Laboratory investigation; a journal of technical methods and pathology, 1994. **71**(2): p. 279-290.
11. van Beuningen, H.M., et al., *Differential effects of local application of BMP-2 or TGF-β1 on both articular cartilage composition and osteophyte formation.* Osteoarthritis and Cartilage, 1998. **6**(5): p. 306-317.
12. Van Osch, G., et al., *The relation between cartilage damage and osteophyte size in a murine model for osteoarthritis in the knee.* Rheumatology international, 1996. **16**(3): p. 115-119.
13. Kindynis, P., et al., *Osteophytosis of the knee: anatomic, radiologic, and pathologic investigation.* Radiology, 1990. **174**(3): p. 841-846.
14. Hernborg, J. and B.E. Nilsson, *The relationship between osteophytes in the knee joint, osteoarthritis and aging.* Acta Orthopaedica, 1973. **44**(1): p. 69-74.
15. Gilbertson, E., *Development of periarticular osteophytes in experimentally induced osteoarthritis in the dog. A study using microradiographic, microangiographic, and fluorescent bone-labelling techniques.* Annals of the rheumatic diseases, 1975. **34**(1): p. 12-25.
16. Nagaosa, Y., P. Lanyon, and M. Doherty, *Characterisation of size and direction of osteophyte in knee osteoarthritis: a radiographic study.* Annals of the rheumatic diseases, 2002. **61**(4): p. 319-324.

17. van de Wetering, R. and R. Batenburg, *A PACS maturity model: a systematic meta-analytic review on maturation and evolvability of PACS in the hospital enterprise.* Int J Med Inform, 2009. **78**(2): p. 127-40.
18. *2009 Annual Report of the U.S. Hospital IT Market*. 2009, HIMSS Analytics and HIMSS.
19. Kurtz, S., et al., *Projections of primary and revision hip and knee arthroplasty in the United States from 2005 to 2030.* J Bone Joint Surg Am, 2007. **89**(4): p. 780-5.
20. Desmeules, F., et al., *The burden of wait for knee replacement surgery: effects on pain, function and health-related quality of life at the time of surgery.* Rheumatology (Oxford), 2010. **49**(5): p. 945-54.
21. Moskowitz, R.W., *Osteoarthritis: diagnosis and medical/surgical management*. 2007: Lippincott Williams & Wilkins.
22. Cibere, J., et al., *Glucosamine sulfate and cartilage type II collagen degradation in patients with knee osteoarthritis: randomized discontinuation trial results employing biomarkers.* The Journal of rheumatology, 2005. **32**(5): p. 896-902.
23. Charni, N., F. Juillet, and P. Garnero, *Urinary type II collagen helical peptide (HELIX-II) as a new biochemical marker of cartilage degradation in patients with osteoarthritis and rheumatoid arthritis.* Arthritis & Rheumatism, 2005. **52**(4): p. 1081-1090.
24. Deberg, M., et al., *New serum biochemical markers (Coll 2-1 and Coll 2-1 NO< sub> 2</sub>) for studying oxidative-related type II collagen network degradation in patients with osteoarthritis and rheumatoid arthritis.* Osteoarthritis and cartilage, 2005. **13**(3): p. 258-265.
25. Kellgren, J. and J. Lawrence, *Radiological assessment of osteo-arthrosis.* Annals of the rheumatic diseases, 1957. **16**(4): p. 494.
26. Bellamy, N., et al., *Validation study of WOMAC: a health status instrument for measuring clinically important patient relevant outcomes to antirheumatic drug therapy in patients with osteoarthritis of the hip or knee.* The Journal of rheumatology, 1988. **15**(12): p. 1833-1840.
27. Eckstein, F., et al., *Proposal for a nomenclature for magnetic resonance imaging based measures of articular cartilage in osteoarthritis.* Osteoarthritis Cartilage, 2006. **14**(10): p. 974-83.
28. Eckstein, F., D. Burstein, and T.M. Link, *Quantitative MRI of cartilage and bone: degenerative changes in osteoarthritis.* NMR in Biomedicine, 2006. **19**(7): p. 822-854.
29. Eckstein, F., et al., *Two year longitudinal change and test-retest-precision of knee cartilage morphology in a pilot study for the osteoarthritis initiative.* Osteoarthritis Cartilage, 2007. **15**(11): p. 1326-32.
30. Frobell, R.B., et al., *Presence, location, type and size of denuded areas of subchondral bone in the knee as a function of radiographic stage of OA - data from the OA initiative.* Osteoarthritis Cartilage, 2010. **18**(5): p. 668-76.
31. Eckstein, F., et al., *Magnitude and regional distribution of cartilage loss associated with grades of joint space narrowing in radiographic osteoarthritis--*

data from the Osteoarthritis Initiative (OAI). Osteoarthritis Cartilage, 2010. **18**(6): p. 760-8.
32. Frobell, R.B., et al., *Femorotibial subchondral bone area and regional cartilage thickness: a cross-sectional description in healthy reference cases and various radiographic stages of osteoarthritis in 1,003 knees from the Osteoarthritis Initiative.* Arthritis Care Res (Hoboken), 2010. **62**(11): p. 1612-23.
33. F Eckstein, M.P.H.L.G., H C Charles,D J Hunter, V B Kraus, T Sunyer, O Nemirovskyi, B T Wyman, R Buck, *Clinical, radiographic, molecular and MRI-based predictors of cartilage loss in knee osteoarthritis.* Annals of the Rheumatic Diseases, 2011.
34. Wirth, W., et al., *Comparison of 1-year vs 2-year change in regional cartilage thickness in osteoarthritis results from 346 participants from the Osteoarthritis Initiative.* Osteoarthritis Cartilage, 2011. **19**(1): p. 74-83.
35. Wirth, W., et al., *MRI-based extended ordered values more efficiently differentiate cartilage loss in knees with and without joint space narrowing than region-specific approaches using MRI or radiography--data from the OA initiative.* Osteoarthritis Cartilage, 2011. **19**(6): p. 689-99.
36. *Validation of Bone Segmentation and Improved 3-D Registration Using Contour Coherency in CT Data.* 2006.
37. Fripp, J., et al., *Automatic segmentation of the bone and extraction of the bone cartilage interface from magnetic resonance images of the knee.* Physics in Medicine and Biology, 2007. **52**(6): p. 1617.
38. Fripp, J., et al., *Automatic Segmentation and Quantitative Analysis of the Articular Cartilages From Magnetic Resonance Images of the Knee.* Medical Imaging, IEEE Transactions on, 2010. **29**(1): p. 55-64.
39. Yin, Y., et al., *LOGISMOS - Layered Optimal Graph Image Segmentation of Multiple Objects and Surfaces: Cartilage Segmentation in the Knee Joint.* Medical Imaging, IEEE Transactions on, 2010. **29**(12): p. 2023-2037.
40. Pakin, S.K., et al., *Segmentation, surface extraction and thickness computation of articular cartilage*. Vol. 3. 2002, Belligham, USA: Society of Photo-Optical Instrumentation Engineers. 12.
41. Grau, V., et al., *Improved watershed transform for medical image segmentation using prior information.* Medical Imaging, IEEE Transactions on, 2004. **23**(4): p. 447-458.
42. Folkesson, J., et al., *Segmenting Articular Cartilage Automatically Using a Voxel Classification Approach.* Medical Imaging, IEEE Transactions on, 2007. **26**(1): p. 106-115.
43. Wang, Q., et al. *Semantic Context Forests for Learning-Based Knee Cartilage Segmentation in 3D MR Images*. in *MICCAI 2013: Workshop on Medical Computer Vision*. 2013.
44. Tang, J., et al., *Surface extraction and thickness measurement of the articular cartilage from MR images using directional gradient vector flow snakes.* IEEE Transactions on Biomedical Engineering, 2006. **53**(5): p. 896-907.

45. Solloway, S., et al., *The use of active shape models for making thickness measurements of articular cartilage from MR images.* Magnetic Resonance in Medicine, 1997. **37**(6): p. 943-952.
46. Dodin, P., et al., *Automatic Human Knee Cartilage Segmentation From 3-D Magnetic Resonance Images.* Biomedical Engineering, IEEE Transactions on, 2010. **57**(11): p. 2699-2711.
47. Merkl, B. and M. Mahfouz, *Unsupervised Three-Dimensional Segmentation of Medical Images Using an Anatomical Bone Atlas*, in *12th International Conference on Biomedical Engineering, Singapore*. 2005.
48. Calder, J., A.M. Tahmasebi, and A.-R. Mansouri. *A variational approach to bone segmentation in CT images*. in *SPIE Medical Imaging*. 2011. International Society for Optics and Photonics.
49. Vasilache, S. and K. Najarian. *Automated bone segmentation from Pelvic CT images*. in *Bioinformatics and Biomeidcine Workshops, 2008. BIBMW 2008. IEEE International Conference on*. 2008. IEEE.
50. Schmid, J. and N. Magnenat-Thalmann, *MRI Bone Segmentation Using Deformable Models and Shape Priors*, in *Medical Image Computing and Computer-Assisted Intervention – MICCAI 2008*, D. Metaxas, et al., Editors. 2008, Springer Berlin / Heidelberg. p. 119-126.
51. Ababneh, S.Y., J.W. Prescott, and M.N. Gurcan, *Automatic graph-cut based segmentation of bones from knee magnetic resonance images for osteoarthritis research.* Med Image Anal, 2011. **15**(4): p. 438-48.
52. K Li, S.M., X Wu, DZ Chen, M Sonka, *Simultaneous segmentation of multiple closed surfaces using optimal graph searching.* Metaxas, DN, Axel, L, Fichingter G, Szekely G. (Eds.) MICCAI, 2005. **5241**: p. 296-304.
53. Bourgeat, P., et al., *MR image segmentation of the knee bone using phase information.* Medical Image Analysis, 2007. **11**(4): p. 325-335.
54. Sodickson, A., et al., *Recurrent CT, cumulative radiation exposure, and associated radiation-induced cancer risks from CT of adults1.* Radiology, 2009. **251**(1): p. 175-184.
55. Buckland-Wright, J.C., et al., *Joint space width measures cartilage thickness in osteoarthritis of the knee: high resolution plain film and double contrast macroradiographic investigation.* Annals of the rheumatic diseases, 1995. **54**(4): p. 263-268.
56. Commission, M.P.A. and A.D. Book, *Healthcare Spending and the Medicare Program*. 2007, Washington: MedPAC, June.
57. Kladny, B., et al., *Comparison of low-field (0.2 Tesla) and high-field (1.5 Tesla) magnetic resonance imaging of the knee joint.* Archives of orthopaedic and trauma surgery, 1995. **114**(5): p. 281-286.
58. Rand, T., et al., *Comparison of low field (0.2 T) and high field (1.5 T) MR imaging in the differentiation of torned from intact menisci.* European journal of radiology, 1999. **30**(1): p. 22-27.

59. Woertler, K., et al., *Detection of articular cartilage lesions: Experimental evaluation of low-and high-field-strength MR imaging at 0.18 and 1.0 T.* Journal of Magnetic Resonance Imaging, 2000. **11**(6): p. 678-685.
60. Kijowski, R., et al., *Comparison of 1.5-and 3.0-T MR Imaging for Evaluating the Articular Cartilage of the Knee Joint1.* Radiology, 2009. **250**(3): p. 839-848.
61. Masi, J.N., et al., *Cartilage MR Imaging at 3.0 versus That at 1.5 T: Preliminary Results in a Porcine Model1.* Radiology, 2005. **236**(1): p. 140-150.
62. Bauer, J.S., et al., *Volumetric Cartilage Measurements of Porcine Knee at 1.5-T and 3.0-T MR Imaging: Evaluation of Precision and Accuracy1.* Radiology, 2006. **241**(2): p. 399-406.
63. Link, T.M., *Cartilage imaging: significance, techniques, and new developments*. 2011: Springer.
64. Yamamura, M., et al., *Open-configuration MRI study of femoro-acetabular impingement.* Journal of Orthopaedic Research, 2007. **25**(12): p. 1582-1588.
65. Gagliardi, J., et al., *Detection and staging of chondromalacia patellae: relative efficacies of conventional MR imaging, MR arthrography, and CT arthrography.* American Journal of Roentgenology, 1994. **163**(3): p. 629-636.
66. Kramer, J., et al., *Postcontrast MR arthrography in assessment of cartilage lesions.* Journal of computer assisted tomography, 1994. **18**(2): p. 218-224.
67. Cibere, J., *Do we need radiographs to diagnose osteoarthritis?* Best Practice & Research Clinical Rheumatology, 2006. **20**(1): p. 27-38.
68. Hayashi, D., et al., *Conventional Radiography as an Indirect Measure for Cartilage Pathology*, in *Cartilage Imaging*. 2011, Springer. p. 27-36.
69. Amin, S., et al., *The relationship between cartilage loss on magnetic resonance imaging and radiographic progression in men and women with knee osteoarthritis.* Arthritis & Rheumatism, 2005. **52**(10): p. 3152-3159.
70. Gale, D., et al., *Meniscal subluxation: association with osteoarthritis and joint space narrowing.* Osteoarthritis and Cartilage, 1999. **7**(6): p. 526-532.
71. Hunter, D., et al., *Change in joint space width: hyaline articular cartilage loss or alteration in meniscus?* Arthritis & Rheumatism, 2006. **54**(8): p. 2488-2495.
72. Wyler, A., et al., *Comparison of MR-arthrography and CT-arthrography in hyaline cartilage-thickness measurement in radiographically normal cadaver hips with anatomy as gold standard.* Osteoarthritis and Cartilage, 2009. **17**(1): p. 19-25.
73. Wyler, A., et al., *Hyaline Cartilage Thickness in Radiographically Normal Cadaveric Hips: Comparison of Spiral CT Arthrographic and Macroscopic Measurements1.* Radiology, 2007. **242**(2): p. 441-449.
74. Li, J., et al., *Three dimensional assessment of knee cartilage in cadavers with high resolution MR-arthrography and MSCT-arthrography.* Academic radiology, 2009. **16**(9): p. 1049-1055.
75. Cootes, T.F., et al., *Active shape models\—their training and application.* Comput. Vis. Image Underst., 1995. **61**(1): p. 38-59.

76. Mahfouz, M.R., et al., *Automatic methods for characterization of sexual dimorphism of adult femora: distal femur.* Computer Methods in Biomechanics and Biomedical Engineering, 2007. **10**(6): p. 447 - 456.
77. Lorenz, C. and N. Krahnstöver, *Generation of Point-Based 3D Statistical Shape Models for Anatomical Objects.* Computer Vision and Image Understanding, 2000. **77**(2): p. 175-191.
78. Besl, P.J. and N.D. McKay, *A Method for Registration of 3-D Shapes.* IEEE Transactions on Pattern Analysis and Machine Intelligence, 1992. **14**(2): p. 239 - 256.
79. Savitzky, A. and M.J.E. Golay, *Smoothing and Differentiation of Data by Simplified Least Squares Procedures.* Analytical Chemistry, 1964. **36**(8): p. 1627-1639.
80. Koo, S., J.H. Rylander, and T.P. Andriacchi, *Knee joint kinematics during walking influences the spatial cartilage thickness distribution in the knee.* Journal of biomechanics, 2011. **44**(7): p. 1405-1409.
81. Wirth, W., et al., *Regional analysis of femorotibial cartilage loss in a subsample from the Osteoarthritis Initiative progression subcohort.* Osteoarthritis and Cartilage, 2009. **17**(3): p. 291-297.
82. Eckstein, F., et al., *Patterns of femorotibial cartilage loss in knees with neutral, varus, and valgus alignment.* Arthritis Care & Research, 2008. **59**(11): p. 1563-1570.
83. Mahfouz, M.R., *Three-Dimensional Morphology of the Knee*, in *Insall & Scott Surgery of the Knee*. 2012, Elsevier. p. 142.
84. Mahfouz, M., et al., *Automatic methods for characterization of sexual dimorphism of adult femora: distal femur.* Computer Methods in Biomechanics and Biomedical Engineering, 2007. **10**(6): p. 447-456.
85. Johnson, J.M., et al., *Clinical and statistical correlation of various lumbar pathological conditions.* Journal of biomechanics, 2012.
86. Fripp, J., et al., *3D statistical shape models to embed spatial relationship information*, in *Computer Vision for Biomedical Image Applications*. 2005, Springer. p. 51-60.
87. Williams, T.G., et al., *Anatomically Corresponded Regional Analysis of Cartilage in Asymptomatic and Osteoarthritic Knees by Statistical Shape Modelling of the Bone.* IEEE Transactions on Medical Imaging, 2010. **29**(8): p. 1541-1559.
88. Mahfouz, M.R., et al., *A robust method for registration of three-dimensional knee implant models to two-dimensional fluoroscopy images.* Medical Imaging, IEEE Transactions on, 2003. **22**(12): p. 1561-1574.
89. Bae, W.C., et al., *Topographic patterns of cartilage lesions in knee osteoarthritis.* Cartilage, 2010. **1**(1): p. 10-19.
90. Perona, P. and J. Malik, *Scale-space and edge detection using anisotropic diffusion.* Pattern Analysis and Machine Intelligence, IEEE Transactions on, 1990. **12**(7): p. 629-639.
91. Vapnik, C.C.a.V., *Support-Vector Networks.* Machine Learning, 1995. **20**: p. 273-297.

92. Tipping, M.E., *Sparse Bayesian learning and the relevance vector machine.* The Journal of Machine Learning Research, 2001. **1**: p. 211-244.
93. Quinlan, J.R., *C4. 5: programs for machine learning*. Vol. 1. 1993: Morgan kaufmann.
94. Domingos, P. and M. Pazzani, *On the optimality of the simple Bayesian classifier under zero-one loss.* Machine learning, 1997. **29**(2-3): p. 103-130.
95. Pazzani, M.J., *Searching for dependencies in Bayesian classifiers*, in *Learning from Data*. 1996, Springer. p. 239-248.
96. Dice, L.R., *Measures of the amount of ecologic association between species.* Ecology, 1945. **26**: p. 297-302.
97. Shan, L., C. Charles, and M. Niethammer. *Automatic atlas-based three-label cartilage segmentation from MR knee images*. in *Mathematical Methods in Biomedical Image Analysis (MMBIA), 2012 IEEE Workshop on*. 2012. IEEE.
98. Lee, S., et al., *Optimization of local shape and appearance probabilities for segmentation of knee cartilage in 3-D MR images.* Computer Vision and Image Understanding, 2011. **115**(12): p. 1710-1720.

Vita

Michael Johnson was born in Houston, TX to Susan and Joe Johnson. At a young age, he moved to Chattanooga, TN where he attended the Lutheran School until transferring to Baylor School in the seventh grade. After graduating from Baylor in 2002, Michael attended Johns Hopkins University, receiving his Bachelor of Science degree in Biomedical Engineering (BME) in 2006, while performing radiology research under Dr. Eliot Siegel and Dr. Khan Siddiqui. Upon graduation he began his graduate studies at the University of Tennessee, under Dr. Mohamed Mahfouz at the Center for Musculoskeletal Research.

Professionally, Michael's interests remain focused on applications of rigorous engineering pertaining to issues related to the human body, specifically in computer vision, machine learning and orthopedics.